Computer Generation of Convergent Beam Electron Diffraction Patterns
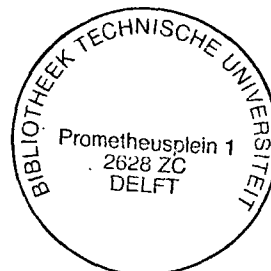

N.S. Blom

Computer Generation of Convergent Beam Electron Diffraction Patterns

Proefschrift

ter verkrijging van de graad van doctor
aan de Technische Universiteit Delft, op gezag van de
Rector Magnificus, prof.dr. J.M. Dirken,
in het openbaar te verdedigen ten overstaan van
een commissie aangewezen door
het College van Dekanen op dinsdag 20 januari 1987 te 16.00 uur

door

NICO SELHORST BLOM

scheikundig doctorandus,

geboren te 's-Gravenhage.

Cover: Tanaka pattern of gallium-arsenide along the
$<1\ \bar{1}\ 0>$ zone axis at 100 KV.

Stellingen.

1) De bewering van Lynch, dat in de 'multi-slice' methode diffractie-effecten van hogere orde Laue zônes altijd worden meegenomen, is onjuist, omdat bij bepaalde laagdikten slechts effecten van de nulde orde Laue zône een rol spelen.

   Lynch D.F., (1971), Acta Cryst., A27, 399.

2) De bewering van Kalonji dat Bollmann in zijn afleiding van de verzameling van oorsprong-punten (Eng: 'O-lattice') een mathematisch inkomplete verzameling genereert, is onjuist.

   Bollmann W., (1982), 'Crystal Lattices, Interfaces,
        Matrices', (Geneva: Bollmann).
   Kalonji G., (1985), J. Physique, 46, coll 4, 249.

3) De zogenoemde Primak-methode voor het bepalen van activeringsspectra uit de logaritmische tijdsafgeleide van isotherm veranderende grootheden kan belangrijk worden verbeterd door een deconvolutie-proces.

   Primak W., (1955), Phys. Rev., 100, 1677

4) Om in het concept van Bollmann's verzameling van oorsprong-punten, in het Engels aangeduid met 'O-lattice', het Engelse woord 'lattice' te gebruiken is incorrect, omdat de punten niet equivalent zijn.

   Bollmann W., (1982), 'Crystal Lattices, Interfaces,
        Matrices', (Geneva: Bollmann).
   International Tables for X-ray Crystallography,
        Volume I, (1969), (Birmingham: Kynoch Press
        /IUCr), 6

5) Met het gebruik van de term 'superrooster-reflekties', met betrekking tot geordende kubisch vlakken-gecenterde - en kubisch lichaams-gecenterde legeringen, moet voorzichtigheid worden betracht.

6) Met het oog op de conventie welke wordt aangehangen met betrekking tot rotaties in de 3-dimensionale ruimte, is het aan te raden om, ter voorkoming van verwarring, middelbare scholieren te gewennen bij het gebruik van een XY-assenstelsel de positieve X-as vertikaal naar boven gericht en de positieve Y-as horizontaal naar rechts gericht te kiezen.

7) De verklaring die Hirashima et al. geven voor de geobserveerde geometrieën van Neodymium complexen met poly-ethyleenglycol-ketens is twijfelachtig.

Hirashima et al., (1981), Bull. Chem. Soc. Jpn., **54**, 1567
Hirashima et al., (1981), Chem. Lett., 1501
Hirashima et al., (1982), Chem. Lett., 1405
Ohmoto et al., (1979), Bull. Chem. Soc. Jpn., **52**, 1209

8) Bij de structuurbepaling van L-asparaginezuur zou de correctie voor tweelingvorming niet op basis van structuurfactoren hebben moeten plaatsvinden, maar op basis van intensiteiten.

Derissen et al., (1968), Acta Cryst., **B24**, 1349

9) De overweging door Lagowski et al. dat dislocatiedichtheden in gallium-arsenide substraten worden veroorzaakt door condensatie van vacatures tot dislocatieringen, is tegenstrijdig met de experimentele bevindingen van Stirland et al. waar juist interstitiële dislocatieringen worden waargenomen.

Lagowski et al., (1984), Semi-insulating III-V Materials, Publ. Shiva
Stirland et al., (1978), J. Mat. Sc., **13**, 657

10) Bij het onderzoek naar de oorzaken van het toenemende aantal beroepen op voorzieningen van de gezondheidszorg, wordt ten onrechte geen aandacht geschonken aan de faktor 'vrije tijd'.

'Nota 2000', 2e Kamerstuk 19500, nrs. 1 en 2, vergaderjaar 1985-1986.

11) Het gebruik van meer dan één mistachterlicht om zichzelf zichtbaar te maken voor medeweggebruikers, is overbodig en leidt in de meeste gevallen tot verwarring.

Verantwoording.

TABLE OF CONTENTS.

List of abbreviations.

BF   —   central disc (brightfield).
CB-cone   —   convergent beam cone.
CBED   —   convergent beam electron diffraction.
CSL   —   coincident site lattice.
DCP   —   dichromatic pattern.
DSC   —   displacement shift complete lattice.
DG   —   diffraction group.
FOLZ   —   first order Laue zone.
HOLZ   —   higher order Laue zone.
WP   —   whole pattern.
ZAP   —   zone axis pattern.
ZOLZ   —   zero order Laue zone.

List of symbols.

$\{\ \}$ —   indication of a set.
$\{R|\underline{t}\}$ —   Seitz operator.
$\cup$ —   union of 2 sets.
$\cap$ —   intersection of 2 sets.

$\forall_g$ —   for all values of g.
$\times$ —   multiplication; vector product.
@   —   convolution.

$\mathcal{F}$ —   Fourier transformation.
superscript $*$ —   complex conjugate[+].
superscript T   —   transpose.

$\left.\begin{array}{c} a,b,c \\ \alpha,b,\gamma \end{array}\right\}$ —   unit cell parameters in direct space.

$\left.\begin{array}{c} a^*,b^*,c^* \\ \alpha^*,\beta^*,\gamma^* \end{array}\right\}$ —   unit cell parameters in reciprocal space.

[uvw]   —   axis in direct space.
<uvw>   —   axis in direct space, including its symmetry related.
(hkl)   —   crystal face or lattice plane or reflection.
{hkl}   —   crystal face or lattice plane or reflection, including their symmetry related.

A —   the eigenmatrix.
$C^{(j)}$ —   vector notation for the set of $C_g^{(j)}$.
$C(r)$ —   Bloch wave amplitude.
$C_{g_t,g_z}^{(j)}$, $C_g^{(j)}$ — g^{th} Fourier component of the jth Bloch wave.

[+] The symbol $*$ also indicates reciprocal unit quantities. These are therefore explicitly mentioned in the list of symbols.

$\bar{C}_h^{(j)}$	—	h^{th} eigen vector element (Fourier component of the jth Bloch wave) of the transposed eigenmatrix.
d_{hkl}^*	—	reciprocal lattice vector hkl.
d_{uvw}	—	direct lattice vector uvw.
D	—	logarithm of intensity; greyvalue.
E_a	—	accelerating voltage of the incident electrons.
f^B	—	first Born approximation atomic scattering factor for electrons.
f_x	—	atomic scattering factors for Xrays.
F_h^x	—	structure factor of reflection h (Xray scattering).
F_h^e	—	structure factor of reflection h (electron scattering).
$\underline{g}$, $\underline{h}$	—	reciprocal lattice vectors.
g, h	—	reflections.
$\underline{g}_t$, $\underline{G}$	—	projection of $\underline{g}$ in plane normal to the zone axis.
g_z	—	vector component of $\underline{g}$ along the zone axis.
G_1, G_2	—	space group of crystal I and II.
G^3_2	—	the set of diperiodic space groups in 3 dimensions.
G^3_3	—	the set of dichromatic space groups in 3 dimensions.
I_h	—	intensity of reflection h.
$\underline{k}^{(j)}$	—	wave vector of the jth Bloch wave.
$\underline{k}_t$	—	vector projection of $\underline{k}^{(j)}$ in plane normal to the zone axis.
$k_z^{(j)}$	—	vector component of $\underline{k}^{(j)}$ along the zone axis.
$\underline{K}$	—	wave vector of the incident electron inside the mean inner crystal potential; deviation of incident beam from crystal surface normal.
K	—	norm of $\underline{K}$.
$p_n(\underline{r})$	—	propagation function in direct space.
$P_n(\bar{h},k)$	—	propagation function in reciprocal space.
$q_n(\underline{r})$	—	transmission function in direct space.
$\underline{q}^{(j)}$	—	inelastic contribution to $\underline{k}^{(j)}$.
$\underline{Q}$	—	deviation vector from central axis of CB-cone.
$\underline{r}$	—	vector in direct space.
$\underline{R}$	—	vector projection of $\underline{r}$ in plane normal to the zone axis; rotation matrix.
$\underline{s}$	—	zone axis in reciprocal space units.
s	—	sine/λ.
T_{CSL}	—	CSL transformation matrix.

$T_g(\underline{k})$	—	transmission in the direction of $\underline{k}+\underline{g}$.
$\underline{u}$	—	zone axis in direct space units.
$U(\underline{r})$	—	'reduced' electron potential $(=2meV(\underline{r})/h^2)$.
U_g	—	g^{th} Fourier component of $U(\underline{r})$.
U_g'	—	inelastic contribution to U_g.
v_g	—	amplitude of the gth diffracted beam.
v	—	vector notation for the set of v_g.
V	—	volume of unit cell in direct space.
V^*	—	volume of unit cell in reciprocal space.
$V(\underline{r})$, $V_c(x,y,z)$	—	crystal potential.
$V'(\underline{r})$	—	inelastic contribution to $V(\underline{r})$.
$^pV_c(x,y)$	—	projected crystal potential.
V_{hkl}	—	Fourier component of crystal potential.
z	—	zone axis direction; vector component of $\underline{r}$ along the zone axis.
Z	—	atomic number.

$\alpha^{(j)}$	—	Bloch wave excitation coefficient.
β^2	—	relativistic correction v^2/c^2.
$\gamma^{(j)}$	—	j^{th} eigenvalue.
δ	—	delta function.
δz	—	slice thickness.
θ	—	half-angle of scattering.
λ	—	radiation wave length.
$\xi(h,k)$	—	excitation error of reflection (h,k).
Σ	—	volume ratio of CSL unit cell and original unit cell; summation sign.
$\varphi(\underline{r})$	—	Bloch wave.
$\underline{\chi}$	—	electron wave vector in vacuum.
$\bar{\Xi}_n(x,y)$	—	mean crystal potential of slice n per unit of length.
$^p\Xi_n(x,y)$	—	projected crystal potential of slice n.
χ_t	—	vector projection of $\underline{\chi}$ in plane normal to the zone axis.
χ_z	—	vector component of $\underline{\chi}$ along the zone axis.
$\Psi(\underline{r})$	—	total wave function.

$2,3,4,6$	—	n-fold rotation axis.
m	—	mirror plane.
$\bar{3},\bar{4},\bar{6}$	—	n-fold inversion-rotation axis.
d,a	—	d-glide, a-glide plane.
primed '	—	symmetry operation, including colour inversion.
subscript R	—	symmetry operation in a diffraction group (see section 2.2.3).

Chapter 1 : Introduction.

In recent years, the interest in the structure of grain
boundaries or, more generally, of interphase boundaries in
materials has greatly increased. The reason for this interest is
the important role that these defects play in the behaviour of
polycrystalline materials in various applications. For instance,
the mechanical properties of materials are largely determined by
the size and distribution of grains in the material. In
semiconductor applications, grain boundaries often cause a
deterioration of electrical properties of various devices. In all
of these applications, it is important to obtain knowledge of the
local structure and composition of the boundary regions in order
to try to improve the material properties.
Since the effective grain boundary region consists, in general,
only of a few atom layers, it is difficult to determine its local
structure and composition. One of the best experimental
techniques that can be applied is transmission electron
microscopy, in which thin foils of material can be analyzed with
respect to their structure and chemical composition. However,
even in thin foils, a grain boundary region occupies only a small
fraction of the volume analysed, and difficulties arise in the
interpretation of grain boundary effects. In spite of these
limitations, considerable progress in this field has been made
over the last ten years, using both electron diffraction and
high-resolution imaging techniques.
Another technique used for this purpose is Convergent Beam
Electron diffraction (CBED). The technique of CBED has often been
applied to determine the point and space group of single crystals
from the symmetry of the CBED patterns taken along certain zone
axes [Goodman 1975, Tinappel 1975, Buxton et al. 1976].
In the investigation of the structure of crystal interfaces, the
CBED technique is a useful tool, since the symmetry of the CBED
pattern is related to the type of interface and particularly to
the state of translation at the interface. The use of
conventional diffraction patterns, i.e. spot patterns, is not
suitable for this kind of investigation, since the difficulty in
obtaining accurate intensities limits a good interpretation.
The CBED patterns have been classified according to 31 so-called
diffraction groups [Buxton et al. 1976]. Recently, Schapink et
al. [1983] and Buxton et al. [1984] have classified the CBED
patterns that can be obtained from bicrystal specimens, i.e.
specimens involving a single interface. In the classification for
bicrystal symmetry determination, the assumption had to be made
that the bicrystal consisted of a parallel-sided combination of
two (identical) single crystals, the interface being coincident
with the mid-plane of the bicrystal specimen (symmetrical
position). In a symmetrical position of the boundary, symmetry
elements lying in the plane of the interface can be observed in
the CBED pattern.
The detailed effect of an asymmetrical position of the boundary
on the symmetry in the CBED pattern could not easily be
predicted. A computer program has, specifically, been developed
to investigate the effect of an asymmetrical boundary position.

Having obtained such a program, it offers the opportunity to investigate properties other than the position of the boundary in the case of a bicrystal. For instance, the effect of specimen thickness or absorption on the CBED pattern of both single and bicrystal specimens can easily be determined.

This thesis treats the description of the computer program based on the N-beam dynamical theory of diffraction [Bethe 1928] for the simulation of CBED patterns from single crystal and bicrystal specimens. The program is used to calculate CBED patterns for silicon, gallium-arsenide and gold single crystal and bicrystal specimens, in order to assess the usefulness of the technique of CBED as an investigative tool for the study of grain boundary structures.

excitation-error distances.   It will be clear that the intensity
of the primary beam is, in this case, more strongly reduced than
in the simple two beam case. The effect is even more pronounced
if we consider the side effects we are dealing with,   such as the
spread in monochromatism of the radiation source (bandwidth), the
shape and limiting dimensions of the crystal specimen and the
thermal motion of the atoms within the crystal.   These effects
account for the observation of intensity of reflections which do
not completely fulfil Bragg's law,   i.e. those reflections having
small excitation-error distances.
The dynamical theory of diffraction is used for the description
of the diffraction phenomenon. The dynamical theory, originally
developed by Bethe [1928],   will be treated in detail in chapter
4.
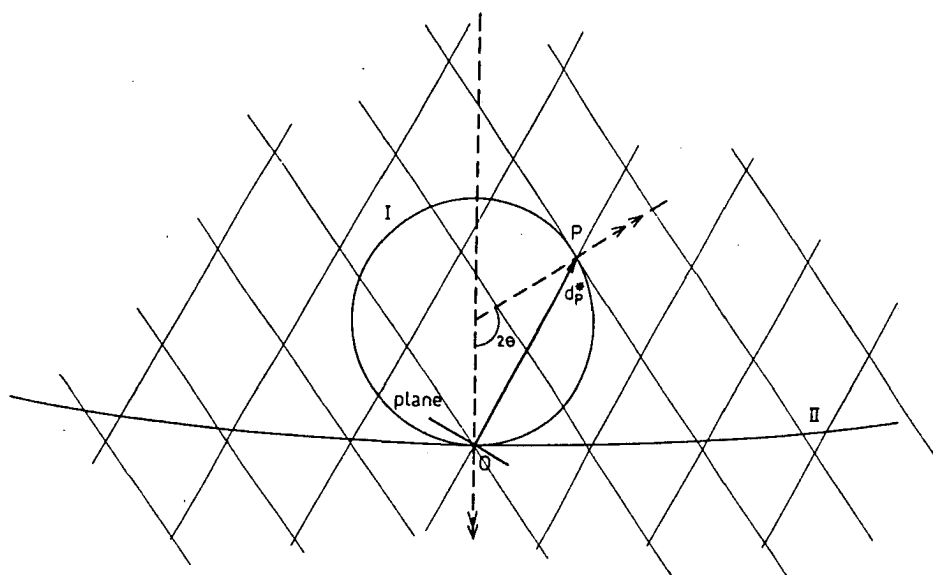
figure 2.1.1

Ewald sphere construction for different wavelengths: I. For
Xray equivalent to the wavelength of Mokα (0.71069 Å)
II. For electrons accelerated with 100kV (0.037 Å).
Point P satisfies Bragg's law of diffraction.

2.1.2 Specimen description.

In the mathematical treatment of high-energy electron diffraction
by a crystal specimen, the specimen is considered to be a thin,
electron transparent,   parallel-sided platelet,   infinite in
transverse directions.   The incoming beam is directed along or
near the surface normal $\underline{s}$ and results in a diffraction pattern
indexed according to the zone axis[+] $\underline{u}$, satisfying the relation

----

[+] A zone axis is defined as the lowest-indexed direct lattice
vector closest to the incident beam direction.

10

$$\underline{g}.\underline{u} = n \qquad\qquad\qquad 2.1.2$$

where $\underline{g}$ is a reciprocal lattice vector and n an integer, indicating the nth order Laue zone (fig. 2.1.2). Alternatively stated, since n is usually small (n= 0,1 or 2), the lattice planes in consideration are perpendicular or almost perpendicular to the specimen surface (symmetrical Laue case) [Humphreys 1979]. Reflections from the plane at n=0 are usually referred to as zero order Laue zone (ZOLZ) reflections; reflections from higher order Laue zones (n > 0) are referred to as HOLZ reflections.

For high-voltage electrons, electron back-scattering can generally be neglected [Buxton 1976]; if absorption is not considered, the original intensity of the incident electrons is conserved in the forward-scattered (transmitted) beams.
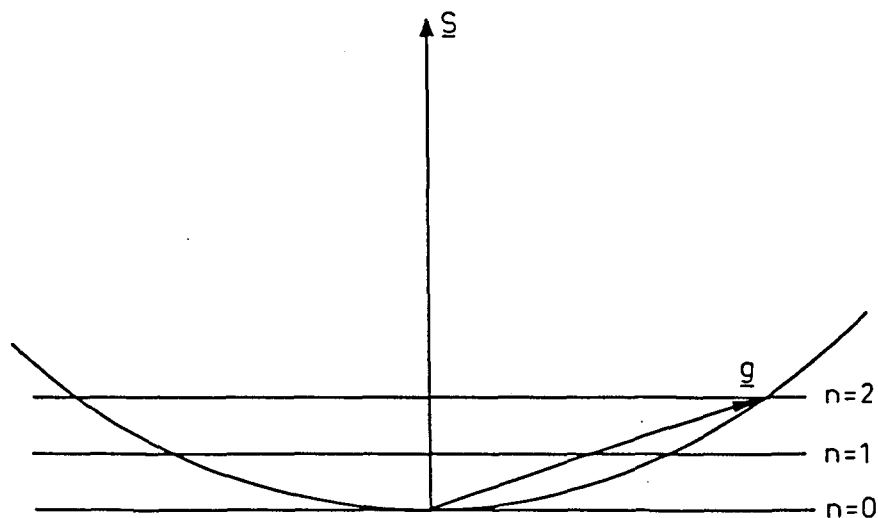
figure 2.1.2

Higher order Laue zone (HOLZ) diffraction. $\underline{s}$ is in the direction of the zone axis $\underline{u}$. The vector $\underline{g}$ is drawn in the case for $\underline{g}.\underline{u} = 2$.

2.1.3 Convergent beam electron diffraction.

In convergent beam electron diffraction (CBED) an incident beam cone is focussed on the specimen. The angle of convergence is usually of the order of a few milli-radians. As a result, the diffraction spots observed in normal diffraction are enlarged into diffraction discs in CBED. Figure 2.1.3 illustrates the application of CBED. In figure 2.1.4 an example of a CBED pattern of a gold single crystal is shown; the axis of the cone is directed along the <1 1 1> zone axis, the resulting discs are

indexed in the same way as the diffraction spots in a normal diffraction pattern. The lines observed in the pattern are Kikuchi lines, which result from further elastic scattering of originally inelastically scattered electrons [Kikuchi 1928, Hirsch et al. 1965]. The concentric rings that are seen result from the intersection of the Ewald sphere with higher order lattice planes (c.f. eq. 2.1.2, with n=1,2 and fig. 2.1.2).
The convergent beam can be thought of as being composed of a cone of (infinitesimal) parallel beams, each with a different deviation from the axis of the CB-cone. Providing the individual incoming beams can be considered to be mutually independent, the resulting CBED diffraction pattern can then be taken as the superposition of the individual diffraction patterns. In other words, the electron source is considered to be perfectly incoherent. Since, in practice this appears to be approximately true, this method is used in the simulations to describe the convergence of the beam .

In the higher-order rings of the diffraction pattern the intensity profiles of the discs are reduced to thin lines. Geometrically this can be explained by considering the fact that the points of the reciprocal lattice can be thought of being enlarged into lattice 'discs'. The intersection of the Ewald sphere with a reflection 'disc' of a HOLZ plane describes an arc of a circle. Along that line, the intensity will be at its maximum (figure 2.1.5).
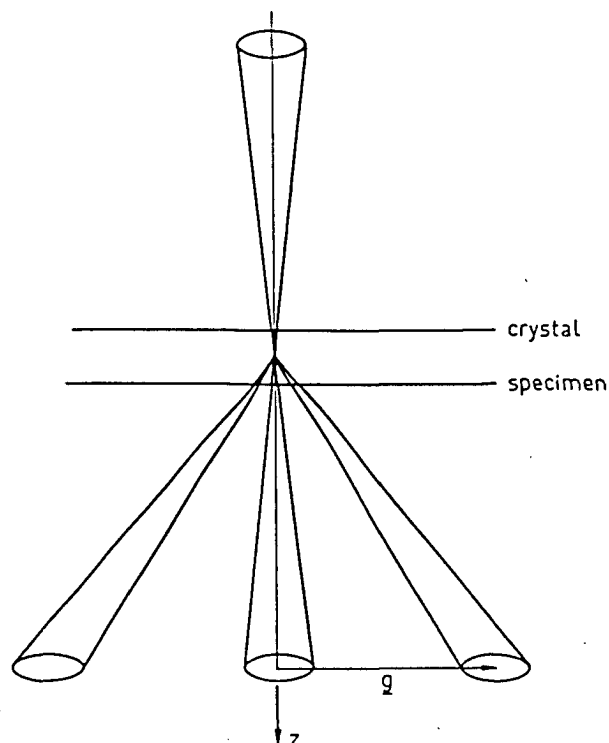
figure 2.1.3

Convergent beam electron diffraction. g indicates a ZOLZ diffraction disc.
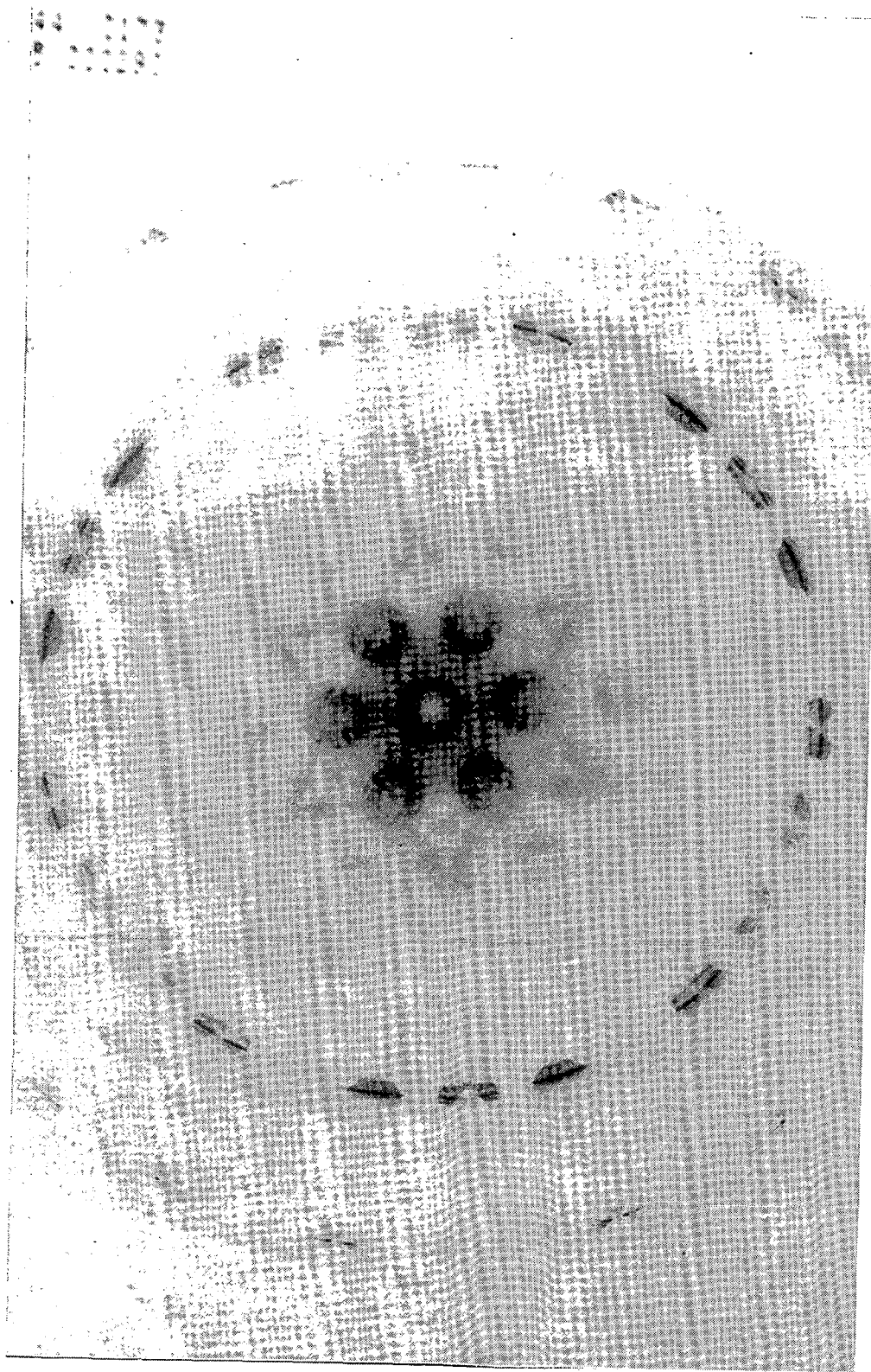
figure 2.1.4

A CBED pattern of gold at 100kV. The axis of the incident
beam cone is directed along the <1 1 1> zone axis. The
pattern shows a 3m symmetry.

13
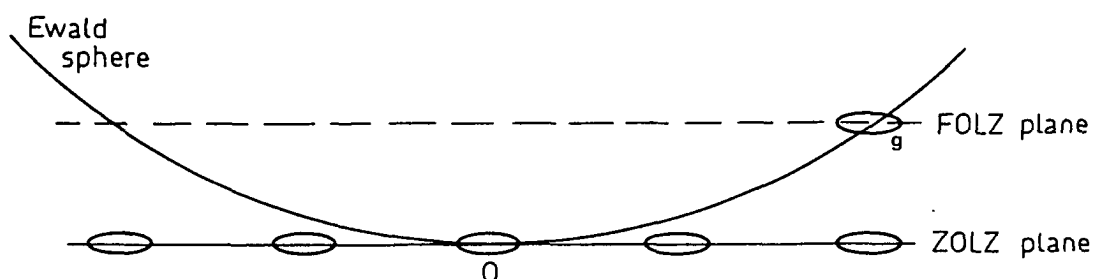
figure 2.1.5

The intensity pattern of a HOLZ disc (g) is reduced to a thin line.

The observation that more than a single line appears within the discs is a result from dynamical interaction between different reflections. This will be treated in more detail in section 4.2.4..

The symmetry present in a CBED pattern such as in figure 2.1.4 is related to the internal crystal symmetry, as will be outlined in the coming sections. A distinction is made between the central disc (i.e. the diffraction disc of the transmitted beam), and the whole pattern. In some cases the central disc can show a higher symmetry than the whole pattern.

2.2 The construction of the 31 diffraction groups.

2.2.1 Breakdown of Friedel's law.

In X-ray diffraction, it is usually observed that between the intensity of a diffraction spot h ($=h_1h_2h_3$) and the diffraction spot $\bar{h}$ the relation exists that

$$I_h = I_{\bar{h}}$$

2.2.1

known as Friedel's law [Friedel 1913]. This law is easily derived

14

since the structure amplitudes F_h and $F_{\bar{h}}$ are mutually complex conjugate if anomalous dispersion is not considered. In the kinematical approach the intensity of a spot is proportional to FF^*, giving eq. 2.2.1. Friedel's law is more accurately formulated as [Miyake & Uyeda 1955]:

'The intensities of the reflections (hkl) and ($\bar{h}\bar{k}\bar{l}$) for a fixed crystal are equal to each other provided the directions of the incident beams which excite these reflections are opposite to each other.'

The breakdown of Friedel's law in electron diffraction was first observed in the measurement of the mean inner potential of reflections from {1 1 1} and {$\bar{1}$ $\bar{1}$ $\bar{1}$} faces of zincblende in 1939 [Thiessen & Moliere 1939]. Miyake and Uyeda [1950] observed the effect in an electron diffraction pattern of zincblende. The failure, only occurring in non-centrosymmetric structures, is explained by the dynamical relation that exists between reflections that are simultaneously excited. As will be seen in the next section, where the phenomenon of reciprocity is treated, there is an exception that can be made for the central disc of a CBED pattern. As a result of reciprocity Friedel's law is satisfied in the central disc in all cases, if absorption is left out of consideration [Goodman & Lehmpfuhl 1968].

2.2.2 The reciprocity theorem.

The principle of reciprocity states that, when a signal originating from a point source at point A is detected at point B, it will be equal, in amplitude and phase, to a signal originating from the same point source at point B and detected at A [von Laue 1935].
In electron diffraction through a thin crystal this means that, for the transmission T of an electron beam directed from above with a deviation $\underline{K}$ from the crystal surface normal and diffracted in a direction $\underline{g}$, the relation exists [Buxton 1976]

$$T_{\underline{g}}^{(+)}(\underline{K}) = T_{\underline{g}}^{(-)}(-\underline{K}-\underline{G}) \qquad\qquad 2.2.2$$

where the + and − superscripts denote whether the beam is directed from above or below respectively (fig. 2.2.1), and $\underline{G}$ is the projection of $\underline{g}$ onto a plane perpendicular to the zone axis[+].

[+] In the notation used, $\underline{g}$ always indicates a lattice point vector in reciprocal space (either ZOLZ or HOLZ), and $\underline{G}$ always the projection of $\underline{g}$ on the plane of zero order Laue reflections. $\underline{G}$ needs therefore not necessarily to be coincident with a reciprocal lattice point in the ZOLZ plane.

The transmission T is taken as a dimensionless quantity, since it can be applied to both the amplitudes and the intensities of the diffracted electron beams. Von Laue [1935] proved the validity of the reciprocity theorem for the amplitude and phase of elastically scattered electrons; Pogany and Turner [1968] proved that in the case of inelastic scattering the reciprocity theorem holds for the intensities, providing there is only a small energy loss.

It is noted that when g is taken to be zero and T refers to intensities, eq. 2.2.2 becomes equivalent to Friedel's law, as has been mentioned in the previous section.

(a)   (b)
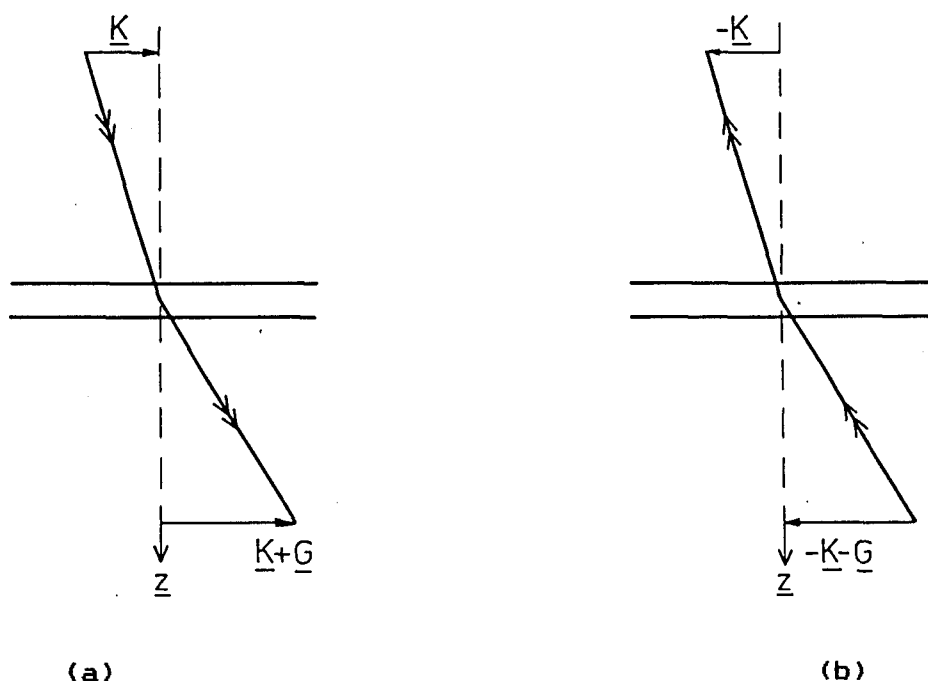
figure 2.2.1

Reciprocity: the transmission resulting from (a) is identical to the transmission resulting from (b).

2.2.3 The 31 diffraction groups.

The pattern symmetries resulting from CBED have been classified according to 31 so-called diffraction groups [Buxton et al. 1976]. The number of 31 can be deduced by considering that a CBED pattern is a superposition of diffraction patterns seen from different directions within the CB-cone projected onto the plane of view. In the first instance the 10 plane point groups, as tabulated in the Int. Tables for Xray Cryst. vol. I, are applicable. The introduction of the effect of reciprocity, as described in the previous section, results in an expansion to 31

point groups: i.e. the 31 diffraction groups as proposed by Buxton et al. [1976] (see also table 2.2). The original 10 plane point groups are a subgroup of the 31 (2-dimensional) diffraction groups. (As a matter of fact, the 31 diffraction groups are isomorphic with the Shubnikov groups of coloured plane figures [Shubnikov 1964]).

The introduction of the reciprocity relation in the construction of the 31 diffraction group, is explained as follows. The effect of reciprocity can actually be detected by inverting the specimen or, indirectly, from the presence of horizontal symmetry elements in the specimen. For instance, if a crystallographic mirror exists which is parallel to the specimen surface, then the $-$ superscript in the righthand side of eq. 2.2.2 can be changed to a $+$, hereby relating the intensity of diffraction spots when looking from one side of the specimen. It is clear that, when using CBED, a horizontal mirror plane as described can be seen immediately by the extra 2-fold symmetry that is present in the central disc of the diffraction pattern, i.e. in the disc of the transmitted beam. Reciprocity and crystal symmetry work in a complementary manner: reciprocity can be detected, apart from an inversion of the specimen, by virtue of additional crystallographic symmetry and certain crystallographic symmetries can be detected by virtue of the reciprocity relation. To be specific, horizontal symmetry elements are detected indirectly through the reciprocity relation[+], whereas vertical symmetry elements can be seen directly. In addition, one has to realize that, what is observed of the crystal (point) symmetry is imposed by the point group of the specimen. The latter will always be less or equal in point symmetry then the former. For instance, a horizontal 3-fold axis will not be observed and a horizontal 4-fold axis will act like a horizontal 2-fold axis.

For reference, table 2.2 shows the 31 diffraction groups and the internal symmetry relations in connection with CBED. The table has been reproduced from Buxton et al. [1976]. The first column shows the 31 diffraction groups. To indicate the effect of reciprocity in the notation of the diffraction groups, Buxton et al. use the subscript R. In figure 2.2.2 some examples illustrate how the diffraction group (DG) notations can be diagrammatically represented.

The effect of R, if present, may be either seen immediately from the diffraction pattern or it may be obscured. An example of the first is diffraction group 1_R, which has 2-fold symmetry in the central disc. According to figure 2.2.2a, all other discs exhibit the same internal 2-fold symmetry when set in the Bragg position (see fig. 2.2.3). The whole pattern has symmetry 1. Diffraction group 2_R (fig. 2.2.2c) has symmetry 1 in both the brightfield and the whole pattern. It is therefore, at first sight, indistinguishable from diffraction group 1. When looking at zero

---

[+] Horizontal here indicates that the symmetry element is perpendicular to the zone axis; vertical means that the symmetry elements are parallel to the zone axis.

Table 2.2

The relation between the diffraction groups and the CBED pattern symmetry. The column indicated with BF (brightfield) gives the symmetry for the central disc; the column indicated WP gives the symmetry for the whole pattern The table has been reproduced from Buxton et al. [1976].

DG	BF	WP	g in Bragg		±g in Bragg	
			gen.	spec.	gen.	spec.
1	1	1	1	n	1	n
1_R	2	1	2	n	1	n
2	2	2	1	n	2	n
2_R	1	1	1	n	2_R	n
21_R	2	2	2	n	21_R	n
m_R	m	1	1	m	1	m_R
m	m	m	1	m	1	m
$m1_R$	2mm	m	2	2mm	1	$m1_R$
$2m_Rm_R$	2mm	2	1	m	2	—
2mm	2mm	2mm	1	m	2	—
2_Rmm_R	m	m	1	m	2_R	—
$2mm1_R$	2mm	2mm	2	2mm	21_R	—
4	4	4	1	n	2	n
4_R	4	2	1	n	2	n
41_R	4	4	2	n	21_R	n
$4m_Rm_R$	4mm	4	1	m	2	—
4mm	4mm	4mm	1	m	2	—
4_Rmm_R	4mm	2mm	1	m	2	—
$4mm1_R$	4mm	4mm	2	2mm	21_R	—
3	3	3	1	n	1	n
31_R	6	3	1	2	1	n
$3m_R$	3m	3	1	m	1	m_R
3m	3m	3m	1	m	1	m
$3m1_R$	6mm	3m	2	2mm	1	$m1_R$
6	6	6	1	n	2	n
6_R	3	3	1	n	2_R	n
61_R	6	6	2	n	21_R	n
$6m_Rm_R$	6mm	6	1	m	2	—
6mm	6mm	6mm	1	m	2	—
6_Rmm_R	3m	3m	1	m	2_R	—
$6mm1_R$	6mm	6mm	2	2mm	21_R	—
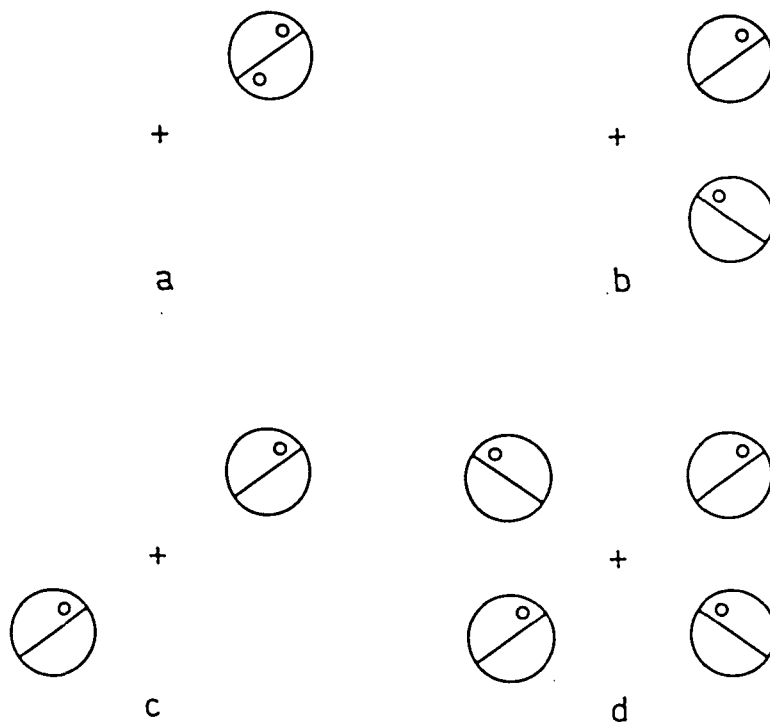
figure 2.2.2

Diagrammatic representation of certain diffraction groups (DG). (a), (b), (c) and (d) represent the DG's 1_R, m_R, 2_R and $2_R mm_R$ respectively. In each diagram, the + sign indicates the position of the zone axis.
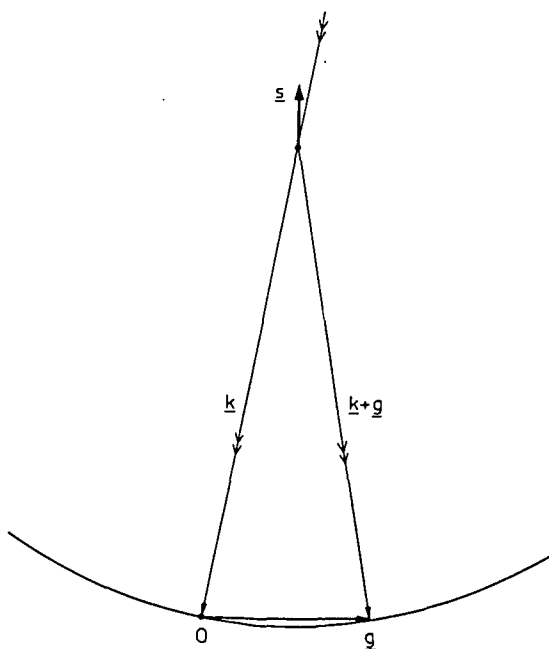

figure 2.2.3

A general ZOLZ reflection $\underline{g}$ set in Bragg position. $\underline{s}$ indicates the direction of the zone axis. $\underline{k}$ is the wave vector of the incident beam.

order Laue zone (ZOLZ) reflections g and $\bar{g}$, successively set in the Bragg position, it is seen that the patterns of the discs are identical in orientation as well as in intensities. Therefore, apart from the 180° relation between discs g and -g, there is an extra 180° rotation of the pattern within the disc(s) itself. This extra rotation is indicated with the subscript R.

Columns 4 and 5 of table 2.2 describe the symmetry of a particular reflection g that will be seen when that reflection is set in the Bragg position. Columns 6 and 7 show the symmetry relation between reflections g and $\bar{g}$ when set in their respective Bragg position. The symbol n in this table means that there is no relation; a dash indicates that the symmetry relation can be deduced from columns 5 and 6.

2.2.4 The projection approximation.

A special case occurs when the crystal potential is seen to be projected in a plane perpendicular to the zone axis:

$$^{P}V_{c}(x,y) = \int_{0}^{z} V_{c}(x,y,z) \, dz \qquad 2.2.3$$

where $^{P}V_{c}(x,y)$ and $V_{c}(x,y,z)$ denote the crystal potential in two dimensions and three dimensions respectively. Because of the periodicity along the z-axis, a unit cell, with its c-axis along the z-axis, can be chosen, having the a^{*} and b^{*} axes perpendicular to c by definition. If the integration is taken over one period in z, eq. 2.2.3 becomes:

$$^{P}V_{c}(x,y) = c \int_{0}^{1} V_{c}(x,y,z) \, dz \qquad 2.2.4$$

It can be shown that the equivalent fourier expansion becomes [Lipson & Cochran 1953]:

$$^{P}V_{c}(x,y) = c \{\Sigma_{h}\Sigma_{k}V_{hk0} \exp(-2\pi i(hx+ky))\} \qquad 2.2.5$$

where V_{hk0} are the fourier coefficients of the crystal potential for $l=0$ and $^{P}V_{c}(x,y)$ is expressed in units of [V][Å] [Goodman & Moodie 1974].

Since the plane of projection has become a mirror plane in itself, it is no longer necessary to differentiate between the top and bottom side of the specimen. The + and - superscripts in eq. 2.2.2 can, therefore, be omitted, resulting in

$$T_g(\underline{K}) = T_g(-\underline{K}-\underline{G}) \qquad\qquad 2.2.6$$

This means that, for g=0 , i.e. the transmitted beam (c.f. footnote on page 15), an inversion centre exists for the transmission in the directions $\underline{K}$ and $-\underline{K}$, equivalent to a 2-fold symmetry in the diffraction disc. In general, when a reflection $\underline{g}$ is set in the Bragg position ($\underline{K} = -\frac{1}{2}\underline{G}$, see also fig. 2.2.3) it follows from eq. 2.2.6 that a slight deviation $\underline{Q}$ from that position ($\underline{K} = -\frac{1}{2}\underline{G} + \underline{Q}$) results in an equivalent transmission in the direction $-\frac{1}{2}\underline{G} - \underline{Q}$. In the CBED pattern this centre of symmetry through $-\frac{1}{2}\underline{G}$ gives a 2-fold symmetry in the gth diffraction disc, when set in Bragg position [Buxton et al. 1976, Pogany & Turner 1968].
The diffraction groups that can be obtained using the projection approximation are those which emerge when a horizontal mirror plane is added. It is obvious that this operation will lead to the 10 diffraction groups containing the symbol 1_R. The fourth column of table 2.2 shows that for a general reflection in the Bragg position a 2-fold symmetry occurs, as expected.

2.3 The effect of translation-coupled symmetry elements.

Thus far, the effect of the crystal point group on the diffraction pattern has been considered. In fact, information concerning only the crystal point group can be obtained from the diffraction group classification. On the other hand, the diffraction pattern itself contains information also on the presence or absence of systematic extinctions, due to either lattice translations (Bravais lattice) or to translation-coupled symmetry elements. This information can, in turn, be translated to information on space group symmetry, as will be outlined below.
In the kinematical treatment of diffraction the intensities of the diffraction spots are proportional to FF^*, where F is the structure factor of a certain reflection hkl and F^* denotes the complex conjugate of F. The phase information, embedded in the stucture factor equation, is therefore lost in the intensities. Translation-coupled symmetry operations can be detected by their systematic extinctions. As a result of the choice of a non-primitive Bravais lattice on the one hand or the presence of screw axes and/or glide planes on the other hand, certain reflections can be forbidden: the value of their structure factor is zero. In principle, every crystal structure can be placed in a primitive lattice. The choice of a non-primitive Bravais lattice is imposed by the choice of a unit cell in agreement with the point symmetry elements present in the structure. The presence of screw axes and/or glide planes is imposed by the unit cell contents, i.e. the structure itself. It will be clear that ignorance of the translation-coupled symmetry operations can easily lead to erroneous results in indexing diffraction spots.
In dynamical diffraction it is possible to generate kinematically forbidden reflections. This can be explained as resulting from

causes [Humphreys 1979]. Firstly, it may be caused by the effect of double (multiple) diffraction, meaning that a beam originating from a reflection g can act as an incident beam for a reflection h, resulting in a reflection $g+h$, which may be kinematically forbidden. Secondly, kinematically forbidden reflections can occur in a thin specimen when the specimen thickness is not equal to an integral number of unit cells [Morris et al. 1968].

Gjonnes and Moodie [1965] have set up general conditions for the continued absence of kinematically forbidden reflections in dynamical diffraction caused by the presence of a screw axis or glide plane having its translation component normal to the zone axis. Depending on the diffraction conditions, an extinction band in the diffraction disc of a kinematically forbidden reflection occurs. The direction of the extinction band makes it possible to distinguish between the presence of either a screw axis or a glide plane [Steeds et al. 1978]. It is therefore possible, using the technique of CBED, to determine 191 of the 230 space groups uniquely [Tanaka et al. 1983].

Different considerations have to be made for translation-coupled symmetry elements having a translation component parallel to the zone axis. In contrast to kinematical diffraction, in dynamical diffraction the intensities of reflections hkl are phase related. In principle it is therefore possible to observe the effect of phase differences, caused by these translation components in CBED discs not dynamically forbidden. On the other hand, considerations made by Goodman [1975] and Buxton et al. [1976] showed no detectable differences in the CBED pattern. Ishizuka [1984] recently showed using calculations based on the multi-slice method, that the effect of a d-glide plane in the spinel structure on its CBED pattern is negligibly small.

Based on these considerations, the effect on the CBED pattern of a translation parallel to the zone axis, originating from a screw axis and/or glide plane, is assumed to be negligibly small. In these cases, only the symmetry operation without its translation-coupled symmetry has to be considered, e.g. a 2-fold screw axis parallel to the zone axis is treated as a normal 2-fold axis.

Chapter 3 : CBED from bicrystals.

3.1   Introduction.

A bicrystal specimen is considered, in analogy to the definition
of a single crystal in the previous chapter, to consist of a
parallel-sided combination of two homogeneous crystals separated
by a plane, the interface. The bicrystal is assumed to be
infinite in transverse directions.

In general, both parts of the bicrystal can be crystals of
different composition, the interface positioned in an arbitrary
direction. We will restrict ourselves to the special case where
both crystals differ only in orientation along a common crystal
axis (rigid body translations included), with the interface
positioned parallel to the bicrystal surfaces (fig. 3.1.1). The
location of the interface (or grain boundary) may still be chosen
arbitrarily. These restrictions offer a sufficient model in
connection with the specimens investigated experimentally. In
practice however, often bicrystal specimens with an inclined
boundary are found, which do not, therefore, fulfil the
symmetrical Laue condition. On the other hand, this type of
specimens can in most cases be approximated by having a stepped
boundary, such that the beam diameter is considerably smaller
than the distance of the individual steps in the boundary plane
(figure 3.1.2).

Given the above mentioned restrictions, the relation between both
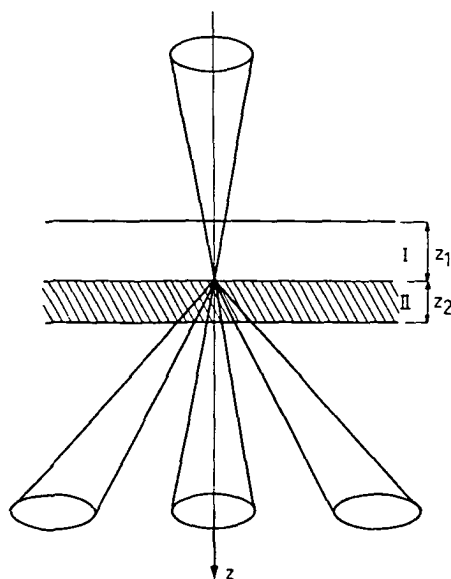parts of the bicrystal can be described as follows. Defining a

figure 3.1.1

The geometry of a bicrystal specimen. The thickness of the
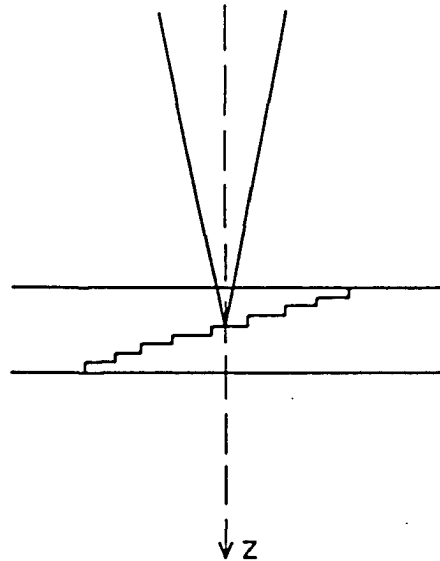constituent parts are z_1 and z_2 for I and II respectively.

figure 3.1.2

The interpretation of bicrystal specimens with an inclined boundary.

coordinate system with the z-axis perpendicular to the bicrystal surface, i.e. parallel the common crystal axis, and indicating the upper crystal by I and the lower crystal by II, the following relation exists

$$\{R_z|\underline{t}\}\ I = II \qquad\qquad 3.1.1$$

In the Seitz operator $\{R_z|\underline{t}\}$ [Seitz 1936], R_z[+] describes an arbitrary rotation along the common axis and $\underline{t}$ is an arbitrary rigid body translation of one crystal relative to the other. Inversely, eq. 3.1.1 becomes

$$\{R_z^{-1}|-\underline{t}\}\ II = I \qquad\qquad 3.1.2$$

The order in which the operations R_z and $\underline{t}$ are applied is immaterial. Since the rotation R_z will always be along the common crystal axis of rotation, in the forthcoming sections the subscript z will be omitted.
Each different combination of R and $\underline{t}$ in eq. 3.1.1, for a certain location of the grain boundary, will, generally, give rise to a different intensity profile of the CBED pattern; the symmetry of the pattern need, not necessarily, to be different for each R and $\underline{t}$. As will be outlined below, it is possible, based on the restriction of having the grain boundary coincident with the midplane of the specimen (i.e. $z_1=z_2$ in fig. 3.1.1), to relate the symmetry present in the bicrystal to the symmetry relations in the CBED pattern, i.e. to the 31 diffraction groups.

[+] The rotation matrix R_z is defined righthanded, the axis of rotation pointing towards the viewer; see also appendix A.

3.2   Crystallographic properties of bicrystal specimens.

Prior to the treatment of the specific crystallographic applications on bicrystals, the concept of two-colour symmetry is introduced. Colour symmetry operations exhibit the same properties as normal symmetry operations, except that in addition a change of 'colour' occurs (fig. 3.2.1). The change of 'colour' is to be interpreted as a change of some kind of property.
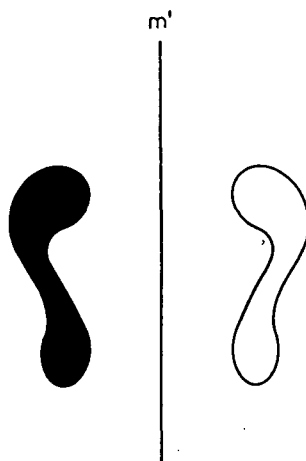
figure 3.2.1

An example of a 2-coloured mirror operation.

In the application of bicrystals the colour is to be interpreted as belonging either to crystal I or crystal II. A coloured symmetry operation in this case relates an atom of a kind (including its environment) belonging to crystal I to an atom of the same kind (including its environment) to crystal II, and vice versa (fig. 3.2.2). Coloured symmetry operations will be indicated by a primed symbol, e.g. 2',m', etc..

figure 3.2.2

A bicrystal specimen having a 2-coloured mirror operation in the plane of the grain boundary.

The method of contructing a bicrystal, described in the previous
section, can be seen as a three-step procedure. All steps
together result in the elimination of some of the classical
symmetry elements, originally belonging to the single crystal
space group, on the one hand, and the generation of coloured
symmetry elements relating crystal I and crystal II, on the other
hand, thus constructing the space group of the bicrystal. The
three steps are (fig. 3.2.3)

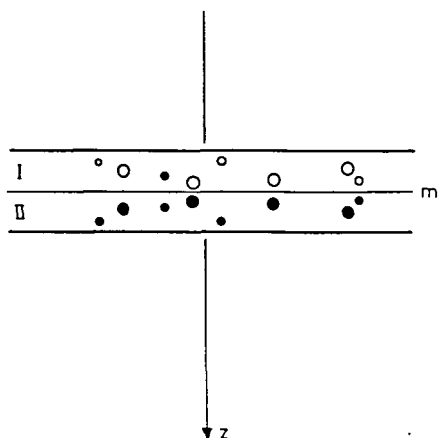Step I
A new pattern is constructed from the superposition of the
constituent structures. Each structure is assigned a colour
'black' and 'white' respectively.

Step II
The location and orientation of the interface are chosen.

Step III
All the 'black' points on one side and all the 'white' points on
the other side of the interface are subsequently rejected. Points
lying exactly on the plane of the interface can be chosen to
belong either to the 'black' structure or the 'white' structure.

The individual steps are treated in more detail here below, apart
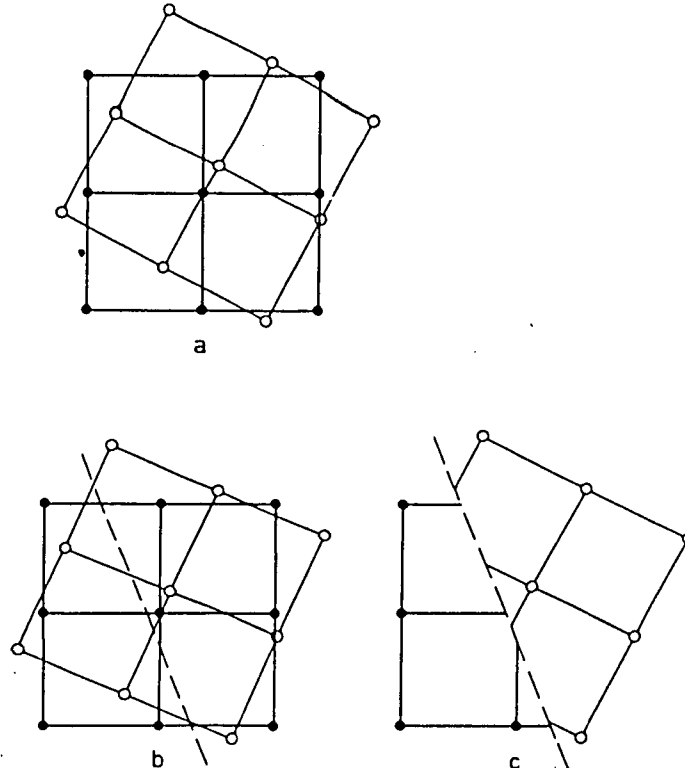from step II which is considered to be trivial.

a

b   c

figure 3.2.3

The construction of a bicrystal specimen. Figures (a), (b),
and (c) illustrate the different steps in the construction
(see text).

26

Step I involves the construction of a pattern composed of the two
interpenetrating structures. This new construction has, depending
on the state of operation (i.e. the Seitz operator in eq. 3.1.1),
either translational symmetry in 1, 2 or 3 dimensions (and will,
therefore, again have a lattice), or has no translational
symmetry. We will restrict ourselves to the case where a new 3-D
lattice is generated, the coincident site lattice (CSL) [Bollmann
1970].
The different constituent structures are assigned a colour
('black' and 'white' lattices), hereby constructing a dichromatic
pattern [Pond & Bollmann 1979]. The symmetry elements that emerge
from the dichromatic pattern are a result of a dissymmetrization
of the original space group and the generation of new coloured
symmetry elements which relate 'black' points to 'white' points,
and vice versa.

The construction of a dichromatic pattern can be dealt with in a
more mathematical way. Consider the space groups of the
constituent structures, G_1 and G_2 respectively. Including the
relation that exists between crystal I and crystal II (eq.
3.1.1), the space group of the dichromatic pattern (DCP) G_{dcp}
will be formed by the union of the classical symmetry elements
that will remain after the dissymmetrization, and the colour
symmetry elements that are generated as resulting from the
relation between I and II.
The classical symmetry elements that will remain are those which
coincide after the transformation $\{R|\underline{t}\}$. In the case when two or
more different rotational symmetry elements are coinciding after
the transformation, the resulting rotation will be that of the
lowest, provided that their modulus is zero (for example a 4 fold
axis coinciding with a 2 fold axis results in a 2 fold axis; a 3
fold axis coinciding with a 2 fold axis gives no resultant
symmetry element). In general, following the treatments of
Gratias and Portier [1982] and Kalonji [1985], the set of
classical symmetry elements emerging in the dichromatic pattern
G_{dcp}, H is given by

$$H = G_1 \cap \{R|\underline{t}\} G_2 \{R|\underline{t}\}^{-1} \qquad\qquad 3.2.1$$

where the symbol $\cap$ denotes the intersection of two sets. It is
noted that the resulting set of operators H is expressed on the
basis of G_1, a similar set can be generated on the vector basis
of G_2; the equivalent set based on the CSL can be obtained from
the similarity transformation THT^{-1}, where T is the CSL
transformation matrix (see next section). H will be a subgroup of
both G_1 and G_2.

Coloured (or anti-) symmetry elements do only occur when the
constituent parts of the bicrystal are identical crystals, i.e.
the interface is homophase and the space groups are related by
the similarity transformation $G_1 = \{R|\underline{t}\}^{-1} G_2 \{R|\underline{t}\}$. A
heterophase interface will result in an empty set of coloured
symmetry operations.

Consider a point in crystal I, x_1, and its equivalent in crystal II, related by $\{R|\underline{t}\}\, x_1 = x_2$. For all the symmetry related points this equation becomes

$$\{R|\underline{t}\}\, G_1 x_1 = \{x_2\} \qquad\qquad 3.2.2^+$$

and vice versa,

$$\{R|\underline{t}\}^{-1} G_2 x_2 = \{x_1\} \qquad\qquad 3.2.3$$

Those operations which transfer a point (and its environment) from crystal I to crystal II and simultaneously a point from crystal II (and its environment) to crystal I will be the common operators out of the sets $\{R|\underline{t}\}\, G_1$ and $\{R|\underline{t}\}^{-1} G_2$, or similarly stated:

$$G' = \{R|\underline{t}\}G_1 \wedge \{R|\underline{t}\}^{-1}G_2 \qquad\qquad 3.2.4$$

where G' denotes the set of operators involving a colour transfer. Since, in the homophase case, G_2 is related to G_1 by $G_2 = \{R|\underline{t}\}\, G_1\, \{R|\underline{t}\}^{-1}$, eq. 3.2.4 becomes

$$G' = \{R|\underline{t}\}\, G_1 \wedge G_1\, \{R|\underline{t}\}^{-1} \qquad\qquad 3.2.5$$

Finally, the space group of the dichromatic pattern G_{dcp} is constructed from the union of H and G'

$$G_{dcp} = H \cup G' \qquad\qquad 3.2.6$$

In general, there are 1651 possible space groups to describe dichromatic patterns in three dimensions [Shubnikov & Koptsik 1964]. These are normally referred to as the Shubnikov space groups. In Vainshtein's notation [Goodman 1984, Vainshtein 1981] the Shubnikov space groups are referred to as $G^3{}_3$, i.e. the dichromatic space groups in three dimensions (superscript 3) having translational symmetry in three dimensions (subscript 3). The classical 230 space groups form a subgroup of $G^3{}_3$.

Step III involves the subsequent rejection of all the 'white' points on one side of the interface and all the 'black' points on the other side. Consequently, not all the space groups of $G^3{}_3$ have to be considered. Caused by the presence of the interface, a maximum of 2-dimensional translational symmetry is to be expected

---

$^+$ The brackets lefthand side are a part of the Seitz operator and the brackets on the righthand side denote a set.

for the pattern resulting after the rejection. Therefore, bicrystals should be described with the 80 diperiodic space groups in 3-dimensional space, G^3_2, a subgroup of G^3_3 [Kalonji 1985]. The group G^3_2 is isomorphic with the 80 2-dimensional space groups of layers [Shubnikov & Koptsik 1964, Pond & Bolllmann 1979, Goodman 1984]. There are 31 point groups in connection with G^3_2, which have, therefore, from a group-theoretical point of view, to be isomorphic with the 31 diffraction groups. Table 3.1 lists the point group operations which are possible in case of the bicrystal specimen in consideration.

Table 3.1

The possible point group operations in case of a bicrystal specimen. The orientation is expressed in terms of the zone axis (z in fig. 3.1.1). The operations $\bar{3}'$, $\bar{4}'$ and $\bar{6}'$, although taken parallel to the zone axis have also a component perpendicular to the zone axis.

orientation	symmetry operations
parallel	2 3 4 6 m
	$\bar{3}'$ $\bar{4}'$ $\bar{6}'$
perpendicular	$\bar{1}'$ m' $2'$

An equivalent line of reasoning can be applied by considering the 122 point groups in connection with group G^3_3. Basically, this set of point groups is composed of three subsets, namely, the 32 classical point groups, the 32 grey point groups (equivalent to the 32 classical point groups including a coloured centre of symmetry, $\bar{1}'$) and 58 general coloured point groups. The 32 classical point groups are used to describe the point group of bicrystals having different constituent parts, i.e. involving a heterophase boundary. The 32 grey point groups are used to describe the point symmetry of stacking-faults or inversion boundaries [Pond & Vlachavas 1983]. The remaining 58 point groups are therefore sufficient to describe the point symmetry of the patterns of interest.
Buxton et al. [1984] and Schapink et al. [1983] have tabulated the relation between the 58 coloured point groups and the resulting DG's in connection with the direction of the incident beam (see also appendix B). In view of the fact that the 58 coloured point groups are related to the 31 DG's, it will be clear that some of the point groups result in the same DG. For instance, the point groups $6'/m'm'm$ and $\bar{6}'m2'$ result in the same DG, $3m1_R$, when the incident beam is taken along the $6'$ and $\bar{6}'$ axis, respectively. Although not applicable in all cases, a few methods are at hand to determine the point group uniquely in such cases. One method involves the interpretation of DG's resulting from different zone-axis patterns (ZAP). Experimentally, different ZAP's from one bicrystal specimen are often difficult

to obtain. Another method is related to the validity of the projection approximation. When three-dimensional diffraction effects are not present, the projection approximation can be applied, making it possible for point groups to be distinguished. An example of the latter method is described by Schapink et al. [1983], illustrated in connection with the above mentioned point groups.

3.3   The coincident site lattice.

As has been mentioned in the previous section, we restrict ourselves to those transformations

$$\{R|\underline{t}\}\ I = II \hspace{4cm} 3.3.1$$

which result in 2-dimensional translational symmetry in the plane of the interface. The axis of rotation is common to both crystals. As a consequence, a new 3-dimensional lattice, the coincident site lattice (CSL), can be constructed which is common to both the consituent crystal lattices (fig. 3.3.1).
Since a general translation $\underline{t}$ does not destroy the translational symmetry, the CSL is only dependent on the specific rotation in the Seitz operator [Bollmann 1982].
With the coincidence of lattice points, the principle axes of the unit cell of the CSL can be expressed in terms of the basis of either crystal I or crystal II, using integral indices. The unit cell of the CSL is usually larger than the original unit cells of the constituent crystals. Defining the ratio of the volume of the CSL unit cell and the original unit cell to be Σ [Friedel 1926], it is found that

$$\det(T_{CSL}) = \Sigma \hspace{4cm} 3.3.2$$

in which T_{CSL} denotes the CSL transformation matrix.
To be consistent with the literature on general crystallographic transformations, the transformation matrix T_{CSL} will have the new lattice vectors as defined on the basis of crystal I, in rows and in a righthanded orientation [Int. Tables of Xray Cryst. vol I].

In figure 3.3.1 an example of a $\Sigma=5$ CSL is shown. The CSL is obtained by a rotation of $36.9°$ along one of the principal axes of a cubic crystal system or along the unique c-axis of a tetragonal system.
In case $\Sigma=1$, the volume of the unit cell of the CSL is identical to the volume of the original unit cell; provided that we are dealing with a bicrystal fitting the description as defined in the previous sections, the associated point group of the CSL must have a coloured centre of symmetry $\bar{1}'$, or must belong to one of the cubic groups [Buxton et al. 1984].
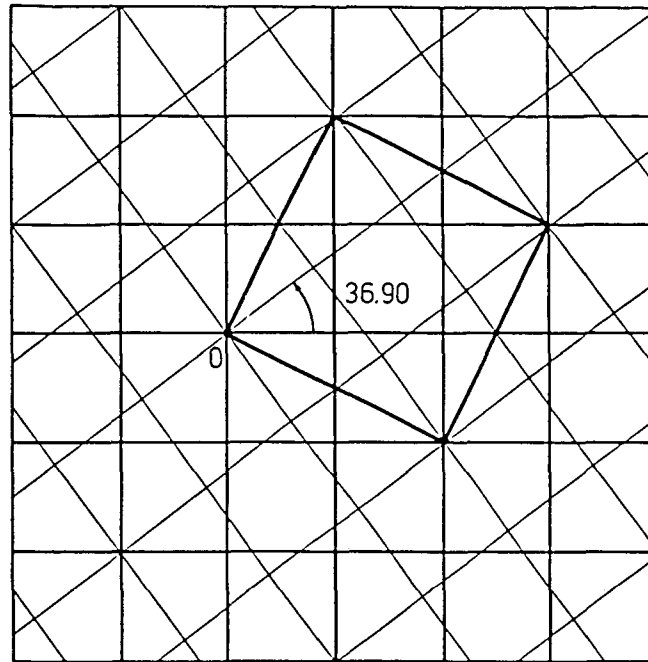
figure 3.3.1

An example of a $\Sigma=5$ CSL. The volume of the CSL unit cell
(heavy lines) is five times as large as the original unit
cells. This CSL can be generated by a rotation of $36.9°$
along one of the principal axes of a cubic crystal system or
along the unique c-axis of the tetragonal crystal system.

As was seen in the mathematical evaluation of the space group of
a dichromatic pattern G_{dcp}, the translational part of the Seitz
operator (eq. 3.3.1) contributed to the formation of G_{dcp}. If the
effect of $\underline{t}$ is split into the effect of its contribution along
the zone axis and the effect of its contribution normal to the
zone axis, it is easy to see what the effect of $\underline{t}$ will be with
respect to G_{dcp} compared to the state of zero translation.
A translational component parallel to the zone axis changes G_{dcp}.
The bicrystal space group and point group remain unchanged, i.e.
all the elements as listed in table 3.1 are conserved despite a
translation in the z-direction.
A translation component normal to the zone axis changes G_{dcp} as
well as the bicrystal point group. Considering the highest
possible symmetry of a DCP, various symmetry operations are
destructed, due to the translation, having direct consequences
for G_{dcp} and the bicrystal point group and, therefore, on the
resultant DG of the CBED pattern. Consequently, it is possible to
relate a resulting CBED pattern to a certain translation
component normal to the zone axis.

31

The difference vectors between the lattice points of crystal I and II form, after the transformation of eq. 3.3.1, again a translation lattice, the displacement shift complete (DSC) lattice [Bollmann 1982]. From those translations, considered within the Wigner-Seitz cell of the DSC, the complete set of space groups of the DCP's is obtained, and, therefore, the complete set of resulting DG's. In general, different translations may lead to the same DG, i.e the relation is not unique for each DG. On the other hand, in specific cases, there may exist a unique relation between the DG and the translation. In such cases it is possible to determine the translation from the symmetry of the CBED pattern [Schapink & Mertens 1981].

Chapter 4 : The computer program for the simulation of CBED patterns.

This chapter is divided into two parts. The first part (A) describes the physical background that is used in the computer program. The second part (B) treats the implementation of the program, including some considerations on the choice of the program language, numerical aspects and the communication with the user. With respect to the use of the hardware configuration, this is described in the introduction to part B and in section 4.6.3.

A. Physical basis.

4.1   Introduction.

An immediate reason for the construction of a computer program for the simulation of CBED patterns, has been the fact that in the classification of diffraction patterns resulting from bicrystals, the assumption had to be made of having the interface coincident with the mid-plane of the specimen, as explained in the previous chapter (section 3.2). What the effect will be when the interface is not coincident with the mid-plane cannot be deduced unless the process is simulated, provided that there exists a physical basis (theory) which makes this possible.
The two most commonly used descriptions of the N-beam dynamical scattering [Goodman & Moodie 1974] are the Bloch wave or eigenvalue method and the multi-slice method. The Bloch wave method is based on the N-beam dynamical theory originally developed by Bethe [1928] and involves the evaluation of an eigenvalue problem for an NxN hermitian matrix. The multi-slice method, developed by Cowley and Moodie [1957], describes the propagation of waves through a crystal as the propagation of waves through a number of thin perfect crystal slices.
Because the Bloch wave method has been taken as a theoretical basis for the program, this method will be treated extensively in this part of the chapter. A general description of the Bloch wave method is given including the effects of higher order Laue zones (HOLZ) and the phenemological treatment of absorption. The multi-slice method will be explained shortly. Finally, considerations are made to sustain the use of the Bloch wave method.

4.2 The dynamical theory of electron diffraction.

4.2.1 General.

The formulation of the dynamical theory of diffraction was originally developed by Bethe [1928]. The theory is based on the description of the electron wave function as a superposition of Bloch waves. It has been used and described by many others over the last decade [Hirsch et al. 1965, Buxton 76, Jones et al. 1977, Baker 1982]. In the next overview, the notation used by Humphreys [1979] and Hirsch et al. [1965] is followed.

The starting point in Bethe's theory is the evaluation of the Schrödinger equation (for convenience, the Schrödinger equation is presently expressed in units of potential) for the wave function of fast electrons in a crystal potential:

$$\{ \frac{\hbar^2}{2me} \nabla^2 + V(\underline{r}) + E_a \} \Psi(\underline{r}) = 0 \qquad 4.2.1$$

where ∇^2 is the Laplace operator, $\hbar = h/2\pi$, m is the relativistic mass of the fast electron, e is the absolute value of the charge of the electron, $V(\underline{r})$ the crystal potential, eE_a the energy of the electrons, which is determined by the accelerating voltage of the incident electrons, and $\Psi(\underline{r})$ the electron wave function. The expression for the electron wave function is twofold:

$$\Psi(\underline{r}) = \begin{vmatrix} \exp(2\pi i \underline{X}.\underline{r}) & z < 0 \\ C(\underline{r})\exp(2\pi i \underline{k}.\underline{r}) & 0 < z < t \end{vmatrix} \qquad 4.2.2$$

in which $\underline{X}$ is the electron wave vector in vacuum with $X^2 = 2meE_a/h^2$ and $\underline{k}$ is the electron wave vector[+] in the crystal specimen of thickness t. The second part of eq. 4.4.2 is usually addressed to as a Bloch wave. $C(\underline{r})$ has the periodicity of the crystal and $\Psi(\underline{r})$ can therefore be fourier expanded as

$$\Psi(\underline{r}) = \Sigma_g \ C_g \exp(2\pi i (\underline{k}+\underline{g}).\underline{r}) \qquad 4.2.3$$

For convenience we define the reduced potential $U(\underline{r})=2meV(\underline{r})/h^2$; the Schrödinger equation is then converted to

----

[+] Since we are dealing with high-energy electrons, the wave vectors used are assumed to be corrected for relativistic effects (see also Humphreys [1979], Fujiwara [1962] and Whelan [1962]).

$$\{ \frac{-1}{4\pi^2} \nabla^2 + U(\underline{r}) + x^2 \} \quad \varphi(\underline{r}) = 0 \qquad\qquad 4.2.4$$

In the same way the reduced crystal potential can be fourier expanded to

$$U(\underline{r}) = \Sigma_h U_h \exp(2\pi i \underline{h} \cdot \underline{r}) \qquad\qquad 4.2.5$$

Substitution of eqs. 4.2.3 and 4.2.5 into eq. 4.2.4 results in a linear equation in the Bloch wave coefficients. Consequently, the solution of the problem results in a set of linear equations of the type:

$$\bigvee_{g} \quad (K^2 - (\underline{k}+\underline{g}))^2 C_g + \Sigma_{h \neq g} U_{g-h} C_h = 0 \qquad\qquad 4.2.6$$

in which K is the magnitude of the mean electron wave vector in the crystal after a correction for the change in wavelength due to the mean crystal potential (refractive index effect), i.e.

$$K^2 = x^2 + U_0 \qquad\qquad 4.2.7$$

Equation 4.2.6 involves one solution for each $\underline{g}$ considered. If we take N reflections into account, there will be N such solutions. To distinguish between the different solutions we include a superscript j. Equations 4.2.6 can be written as an eigenvalue problem of an N×N matrix, giving the N solutions of the individual Bloch waves. We write

$$AC^{(j)} = \gamma^{(j)} C^{(j)} \qquad\qquad 4.2.8$$

where A denotes the N×N (hermitian) eigenmatrix, $C^{(j)}$ one of the eigenvectors of the problem and $\gamma^{(j)}$ the associated eigenvalue. Taking $\underline{g}=(g_t,g_z)$ and $\underline{k}=(k_t,k_z)$, in which the subscripts t and z denote the tangential and parallel component of $\underline{g}$ and $\underline{k}$ along the zone axis, respectively. We evaluate for the eigenvalue $\gamma^{(j)}$

$$K^2 - k_z^{(j)2} \approx 2K \ (K - k_z^{(j)}) = -2K\gamma^{(j)} \qquad\qquad 4.2.9$$

having included the high-energy approximation $K+k_z^{(j)} \approx 2K$. Including reflections belonging to higher-order Laue zones (HOLZ), the diagonal elements of the eigenmatrix A become (after assuming $g_z \ll k_z^{(j)}$):

$$-(k_t + g_t)^2/2K - g_z \qquad\qquad 4.2.10$$

and off-diagonal elements

$$U_{g-h}/2K \qquad\qquad 4.2.11$$

Section 4.2.3 will treat the characteristics of the eigenmatrix in more detail.

As there are different solutions fulfilling eq. 4.2.8, the appropriate solution for the Schrödinger equation will be the superposition of the individual Bloch waves

$$\Psi(\underline{r}) = \sum_j \alpha^{(j)} \sum_g C_g^{(j)} \exp 2\pi i (\underline{k}^{(j)} + \underline{g}) \cdot \underline{r} \qquad\qquad 4.2.12$$

in which $\alpha^{(j)}$ is the excitation coefficient (or amplitude) of the jth Bloch wave.
Following eq. 4.2.2 we can write for the total wave function

$$\Psi(\underline{r}) = \begin{vmatrix} \exp 2\pi i \underline{X} \cdot \underline{r} & z < 0 \\ \sum_j \alpha^{(j)} \varphi^{(j)}(\underline{r}) & 0 < z < t \end{vmatrix} \qquad\qquad 4.2.13$$

The excitation amplitudes of the individual Bloch waves can be found from the boundary conditions at $z = 0$ (continuity in Ψ and grad Ψ), i.e. from the consideration of continuity in the tangential components of the wave vectors in vacuum and inside the crystal it follows, taking $\underline{r}=(R,z)$, that:

$$\exp 2\pi i \; X_t \cdot \underline{R} = \sum_j \alpha^{(j)} \sum_g C_g^{(j)} \exp 2\pi i (k_t^{(j)} + g_t) \cdot \underline{R} \qquad\qquad 4.2.14$$

with $\underline{r}=(R,z)$ and $\underline{X}=(X_t,X_z)$, i.e. the tangential and parallel components along the zone axis, respectively.
The excitation coefficients of the Bloch waves $\alpha^{(j)}$ remain to be determined. Multiplying both sides with $\exp -2\pi i (X_t - g_t') \cdot \underline{R}$, where g_t' is different from g_t, then, after integration over the area S enclosed by the translational symmetry vectors a_x and a_y (i.e. $V(\underline{r}+a_x)=V(\underline{r})$ and $V(\underline{r}+a_y)=V(\underline{r})$), with a_x and a_y in the boundary surface [Heine 1963], we have

$$\delta(g_t') = \sum_j \alpha^{(j)} \sum_g C_g^{(j)} \delta(k_t^{(j)} - X_t + g_t + g_t') \qquad\qquad 4.2.15$$

36

Since for all the Bloch waves $k_t^{(j)} (=k_t) = X_t$, and because of the delta function on the left-hand side, we get:

$$1 = \Sigma_j \propto^{(j)} \Sigma_g C_g^{(j)} \delta(g_t) \qquad\qquad 4.2.16$$

The delta function $\delta(g_t)$ indicates that only those C_g's for which $g_t=0$ remain in the summation, i.e. they still may have a component g_z. For clarity we extend our notation to $C_g = C_{g_t,g_z}$. Equation 4.2.16 becomes:

$$1 = \Sigma_j \propto^{(j)} C_{0,0}^{(j)} + \ldots + \Sigma_j \propto^{(j)} C_{0,g_z}^{(j)} + \ldots \qquad 4.2.17$$

From the characteristics of a hermitian eigenvalue problem we know that the resulting (complex) eigenvectors exhibit the orthogonality relation, meaning that

$$\Sigma_j C_{g_t,g_z}^{*(j)} C_{h_t,h_z}^{(j)} = \delta_{gh} \qquad\qquad 4.2.18$$

Therefore, for each possibility $C_{0,g_z}^{*(j)}$ within the set of reflections substituted for $\propto^{(j)}$, equation 4.2.17 is fulfilled. On the other hand, we must realize that the coefficients $C_{0,g_z}^{(j)}$ belong to a different Brillouin zone than the one we are considering. Therefore, the solution is unique and we write:

$$\propto^{(j)} = C_{0,0}^{*(j)} = C_0^{*(j)} \qquad\qquad 4.2.19$$

In conclusion, we can write for the total wave function of a fast electron in a crystal potential field, that

$$\Psi(\underline{r}) = \Sigma_j C_0^{*(j)} \Sigma_g C_g^{(j)} \exp 2\pi i (\underline{k}^{(j)} + \underline{g}) \cdot \underline{r} \qquad 4.2.20$$

The way in which this wave function is used to calculate the intensities belonging to the different diffraction spots (or discs in CBED) as a function of specimen thickness, will be treated in the coming sections.

The main objective of the calculations have been to include higher order Laue zone effects. Buxton [1976] has treated the HOLZ effects using perturbation methods on a two-dimensional approximation including the projected vectors (or g_t-vectors) of higher order Laue zones. These g_t-vectors do not necessarily have to coincide with reciprocal lattice vectors of the ZOLZ. This construction leads to a set of secular equations resulting in

37

Bloch waves for the 2-D case (not to be confused with the general approach of the projection approximation in which only g-vectors are included as lattice vectors belonging to the zero order reciprocal lattice plane). The Bloch wave states in three dimensions can then be found by expansion of the 2-D states (see also Baker [1982]). It must be noted that, with the use of secular equations the interlayer interactions are neglected.

The effects of HOLZ interactions are presently included by considering the first term in eq. 4.2.6 as

$$K^2 - (\underline{k}^{(j)}+\underline{g})^2 = -2K\gamma^{(j)} - 2k_z^{(j)}g_z - (k_t+g_t)^2 - g_z^2 \qquad 4.2.6a$$

The last term in this equation, g_z^2, is neglected since it is assumed that $g_z \ll k_z^{(j)}$. The second term on the right-hand side in eq. 4.2.6a destroys the hermitian property of the eigenvalue problem. By applying the approximation that at high energy $k_z^{(j)} \approx K$, the hermitian property is conserved. Jones et al. [1977], on the other hand, treat the second term by substituting $k_z^{(j)} = K + \gamma^{(j)}$. An appropriate choice of the eigenvectors again results in a hermitian problem.

Jones' approach differs form the present approach by only a factor of $1/(1+g_z/K)$. Since we are dealing with small values of g_z compared to K, the resulting intensities will show differences which are numerically insignificant (see also section 4.6.4).

4.2.2 Electron scattering and the structure factor.

The scattering of electrons by the individual atoms can be obtained from Mott's formula [Mott 1930, Hirsch et al. 1965, Humphreys 1979] in terms of the atomic scattering for Xrays:

$$f^B(s) = 0.023934 \ (Z-f_x(s))/s^2 \qquad 4.2.21$$

where $f^B(s)$ is the Born electron scattering amplitude in units of [Å], $f_x(s)$ the atomic scattering for Xrays, $s=\sin\theta/\lambda$ and Z the atomic number (see also the Int. Tables for Xray Cryst. vol. IV). In the case where s=0 the scattering amplitudes can be obtained from [Ibers 1958]

$$f^B(0) = 4\pi m e^2/3h^2 \times Z\langle r^2\rangle \qquad 4.2.22$$

where $\langle r^2\rangle$ is the mean-square atomic radius. The values for $f^B(0)$ are also listed in the Int. Tables for Xray Cryst. vol. IV. The values for the atomic scattering factors for Xrays can be obtained from the Tables or can be calculated by a polynomial

approximation [Cromer & Waber 1965].

The reduced potential, as used in the evaluation of the Schrödinger equation, is given by

$$U_h(s) = V^* F_h^e(s)/(\pi\sqrt{(1-\beta^2)})$$ 4.2.23

where $F_h^e(s)$ is the structure factor based on the scattering of electrons, β is the relativistic correction and V^* is the volume of the unit cell in reciprocal space.

4.2.3 The eigenmatrix and its solutions.

In section 4.2.1 it was shown that the resulting eigenvalue problem involved the solution of a NxN hermitian matrix, in which N is the number of reflections taken into account. We reconsider

$$AC^{(j)} = \gamma^{(j)}C^{(j)}$$ 4.2.8

in which A is the eigenmatrix, $C^{(j)}$ is the jth Bloch wave with fourier coefficients $C_h^{(j)}$ and $\gamma^{(j)}$ is the associated eigenvalue. Refering back to eq. 4.2.10 it is known that the eigenmatrix has diagonal elements

$$-(k_t+g_t)^2/2K - g_z$$ 4.2.10

which are real in all cases, and off-diagonal elements

$$U_{g-h}/2K$$ 4.2.11

The upper triangle of the eigenmatrix is composed of values resulting from eq. 4.2.11; the lower triangle with values following from the same equation with U_{h-g} substituted for U_{g-h}. Depending on the relation that exists between U_{g-h} and U_{h-g} we find that four distinct situations can be recognized for the properties of the eigenmatrix. The four distinct situations will be treated individually [Acton 1970].

1) elastic scattering and non-centrosymmetry.

From the definition of the structure factor it follows that, if only elastic scattering is considered (i.e. no absorption) and the structure is general non-centrosymmetric, we find

$$U_{g-h} = U_{h-g}^{*} \qquad\qquad 4.2.24$$

leading to a hermitian eigenmatrix ($A = (A^{*})^{T}$). In general the characteristic solution of a hermitian matrix results in real eigenvalues and complex mutually orthogonal eigenvectors. The property of mutual orthogonality denotes that the eigenvectors exhibit the following relation

$$\Sigma_{j} C_{g}^{*(j)} C_{h}^{(j)} = \delta_{gh} \quad \underline{and} \quad \Sigma_{g} C_{g}^{*(i)} C_{g}^{(j)} = \delta_{ij} \qquad 4.2.25$$

(c.f. eq. 4.2.18; it is noted that this orthogonality property has been used there to determine the Bloch wave excitation amplitudes).

2) elastic scattering and centrosymmetry.

If only elastic scattering is considered and the structure is centrosymmetric, we have the relation that

$$U_{g-h} = U_{h-g} = U_{h-g}^{*} \qquad\qquad 4.2.26$$

This can only be the case when the U's are all real, resulting in a real symmetric matrix ($A = A^{T}$), i.e. a special case of the hermitian property. The eigenvalues and eigenvectors will now both be real[+]; the eigenvectors will still be mutually orthogonal.

3) inelastic scattering and centrosymmetry.

In the third case absorption is considered. Because of the centrosymmetry we still have the relation $U_{g-h} = U_{h-g}$, but due to the effect of absorption, the equivalence with its complex conjugate is lost. Therefore, we have

----

[+] It must be noted that if there is a degeneracy in eigenvalues (equal eigenvalues) not only the associated eigenvectors are a solution to the problem but also any linear combination of those eigenvectors, including combinations of the type $\underline{A}+i\underline{B}$ (c.f. appendix A of Jones et al. [1977]).

$$U_{g-h} = U_{h-g} \ast U_{h-g}^{\ast} \qquad\qquad 4.2.27$$

i.e. the eigenmatrix is complex symmetric. The solution is a set of complex eigenvalues and associated mutually orthogonal complex eigenvectors.

4) inelastic scattering and non-centrosymmetry.

In the most general case, absorption is considered and the structure is non-centrosymmetric. There will exist no relation between U_{g-h} and U_{h-g}. In general, we have

$$U_{g-h} \ast U_{h-g} \qquad\qquad 4.2.28$$

The eigenmatrix is asymmetric complex, giving complex eigenvalues and eigenvectors. The orthogonal property is lost. Instead, the eigenvectors exhibit a bi-orthogonal relationship [Acton 1970, Wilkinson 1965] with the eigenvectors of the transposed eigenmatrix A^T, meaning

$$\Sigma_j C_g^{\ast(j)} \bar{C}_h^{(j)} = \delta_{gh} \quad \underline{and} \quad \Sigma_g C_g^{\ast(i)} \bar{C}_g^{(j)} = \delta_{ij} \qquad 4.2.29$$

where $\bar{C}$ denotes an eigenvector element of the transposed eigenmatrix. In the evaluation of eq. 4.2.17 for the determination of the Bloch wave excitation amplitudes, eq. 4.2.29 should actually be used in cases where the eigenvalue problem involves a general complex matrix.
The computational evaluation of an asymmetric complex eigenvalue problem is, despite the availability of elaborate algorithms, still a time consuming process. For this reason, the phenemological treatment of absorption is included with the use of first order pertubation methods as described in section 4.2.6.

4.2.4 The dispersion surface.

The evaluation of the eigenmatrix gives the solution of the permitted values $k_z^{(j)}$ for each Bloch wave j as a function of the incident beam direction expressed by k_t ($=X_t$, from the boundary conditions). A plot of these permitted values $k_z^{(j)}$ against k_t is called the dispersion surface.
In the 'free-electron' case, when the diffracted intensities are vanishingly small (all the off-diagonal elements in the eigenmatrix are set equal to zero, i.e. $U_{g-h}=U_{h-g}=0$), it can be shown that the solution corresponds to an electron wave vector lying on one of the free-electron spheres with radius K centred on the (set of) reflections taken into account. The spheres intersect at the Brillouin zone boundary. Degeneracy occurs at the intersection with $k_t=-\frac{1}{2}g_t$.

With potentials of the incident electrons, the influence of the crystal potential becomes apparent. Switching on the crystal potential $(U_{g-h}$ and $U_{h-g} \neq 0)$ causes the dispersion surface to split at the Brillouin zone boundaries. The individual dispersion branches are asymptotic to the free-electron spheres[+].
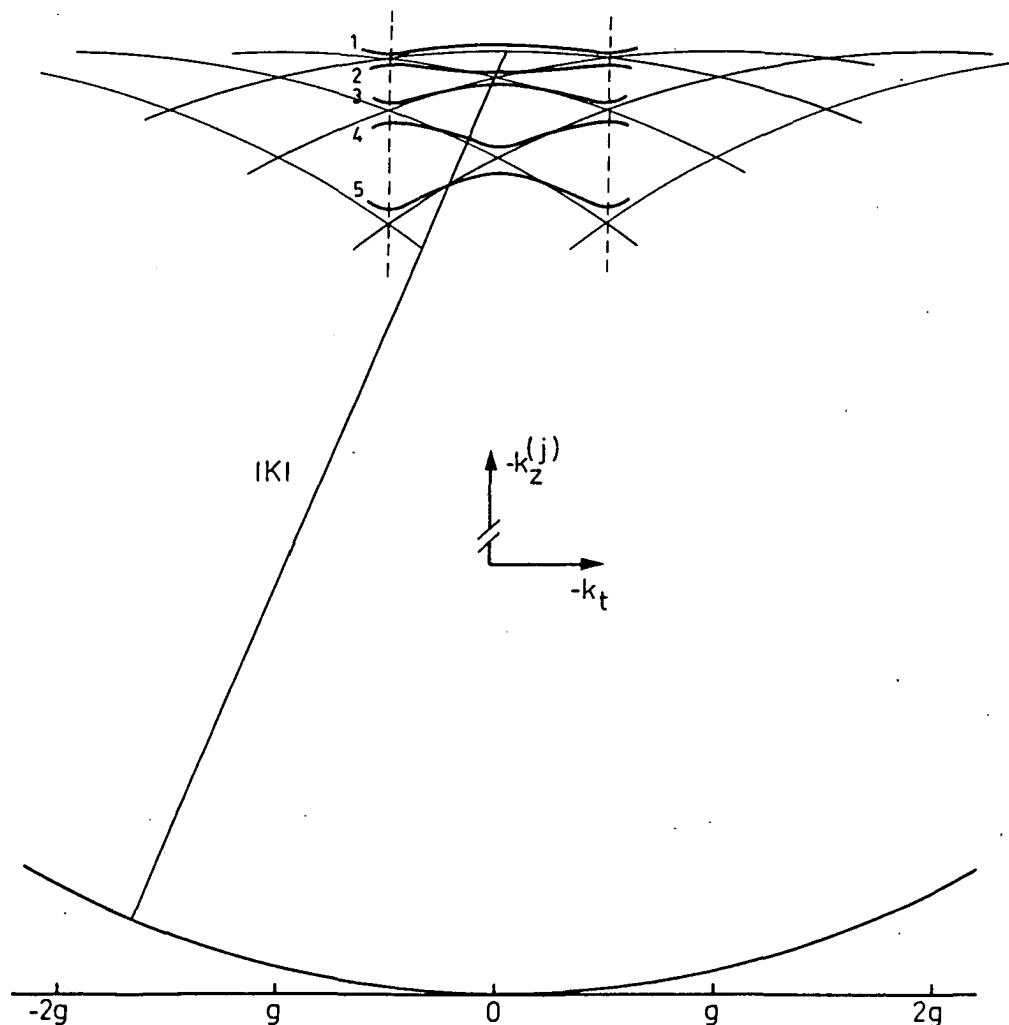
Figure 4.2.1 shows a cross-section of the dispersion surface in the direction of g in a 5-beam case. The individual branches are labeled according to Humphreys and Fisher [1971]. The dispersion surface has the symmetry of the weighted reciprocal lattice seen along the zone axis.

figure 4.2.1

Cross-section of the dispersion surface in the direction of g in a 5-beam symmetrical Laue case. The individual branches of the dispersion surface are labeled according to Humphreys and Fisher [1971]. The dispersion surface is symmetric across the Brillioun zone boundary.

[+] Since K is here the electron wave vector corrected for the mean inner potential, the free-electron spheres are in fact 'corrected' free-electron spheres.

disc
diameter

dispersion
surface

$-k_z^{(J)}$

$-k_t$

a

1

2

|K|
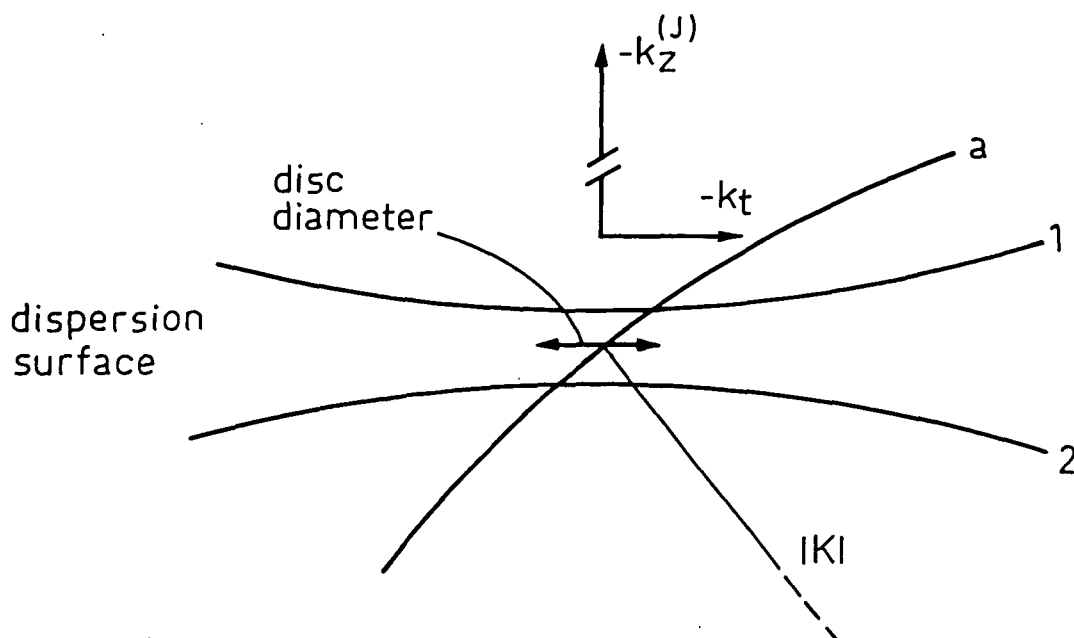
figure 4.2.2

Geometrical contruction of the intersection of the zero
layer dispersion surface observed in HOLZ diffraction discs
(line a).

The individual branches of the zero layer dispersion surface can
be seen in a CBED pattern [Steeds et al. 1982]. If a sphere of
radius K is drawn from a HOLZ reflection g near or in the Bragg
position, this sphere intersects some of the branches within the
disc diameter of the convergent beam (figure 4.2.2). Each
intersection of that sphere (i.e. at certain values of k_t) with
one of the branches of the dispersion surface, gives rise to
intensity in a point (k_t+g_t) in the HOLZ diffraction disc.
All the points of intersection coming from k_t values out of the
plane of drawing in figure 4.2.2 add up to intensity lines in the
HOLZ diffraction disc. Each line in the HOLZ diffraction disc
can, therefore, be geometrically assigned to one of the branches
in the dispersion surface.

In the case of a bicrystal, it is not possible to construct a
dispersion surface by analogy with the single crystal case as
described above.
Consider for instance a silicon bicrystal, having a $\Sigma=3$ type
boundary, viewed along <1 1 1>. The dispersion surfaces of the
top and bottom part fit exactly in the projection approximation,
since the mutual rotation of the dispersion surface belongs to
the rotational symmetry of the weighted ZOLZ plane. In this case
the dispersion surface can be seen to belong to the entire
bicrystal. When HOLZ reflections are included, this reasoning is
not valid, since the individual dispersion surfaces no longer
coincide. Consequently, it is therefore assumed, that the
dispersion surfaces of the constituent crystals should be
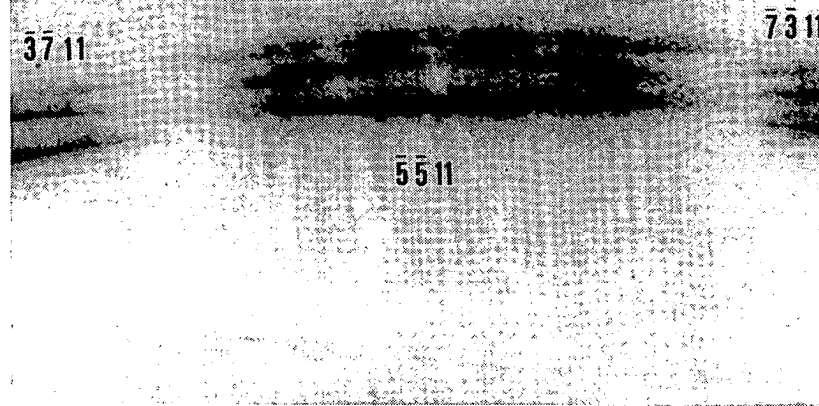treated separately.

figure 4.2.3

An example of the observation of dipersion branches in the
<5 5 11> HOLZ diffraction disc (c.f. fig. 4.2.2) of silicon.
The incident beam (100 kV) is directed along the <1 1 1>
zone axis.

4.2.5 The diffracted intensities.

As has been shown in section 4.2.1, the total wave function for
the description of fast electrons in a crystal potential field is
given by

$$\Psi(\underline{r}) = \Sigma_j C_0^{*(j)} \Sigma_g C_g^{(j)} \exp 2\pi i (\underline{k}^{(j)} + \underline{g}).\underline{r} \qquad 4.2.20$$

In order to calculate the intensities of the transmitted and
diffracted beams, the amplitudes of the beams must be evaluated.
The component of the diffracted wave that contributes to the
intensity of the spot in the diffraction pattern, is the
component parallel the crystal surface, i.e. in the direction
$k_t + g_t$. Equation 4.2.20 can be expanded to

$$\Psi(R,z) = \Sigma_j C_0^{*(j)} \Sigma_g C_g^{(j)} \exp 2\pi i (k_t + g_t).R \times$$

$$\exp 2\pi i (k_z^{(j)} + g_z).z \qquad 4.2.30$$

Defining the amplitude in the direction $k_t + g_t$ as $v_g(z)$, we write

$$\Psi(R,z) = \Sigma_g v_g(z) \exp 2\pi i (k_t + g_t).R \qquad 4.2.31$$

44

From the combination of equations 4.2.30 and 4.2.31, it follows

$$v_g(z) = \Sigma_j \; C_0^{*(j)} \; C_g^{(j)} \exp 2\pi i \, (k_z^{(j)} + g_z) . z$$

$$....4.2.32$$

Subsequently, the resulting intensity is calculated by

$$I_g(z) = v_g(z) \times v_g(z)^* \qquad\qquad 4.2.33$$

For the intensity calculations we need the values of $k_z^{(j)}$ to evaluate the exponents of eq. 4.2.32. These values can be obtained from the eigenvalues $\gamma^{(j)}$, since $\gamma^{(j)} = k_z^{(j)} - K$. A much simpler method is using the eigenvalues $\gamma^{(j)}$ directly, instead of the values $k_z^{(j)}$. Since the term $\exp(-2\pi i K + g_z)$ can be taken outside the summation sign, and a phase modulation of the amplitude does not influence the values of the intensity, we are allowed to do this

In matrix notation we have [Humphreys 1979]

$$v = C \; \{\exp 2\pi i \gamma^{(j)} . z\} \; C^{-1} \; u \qquad\qquad 4.2.34$$

in which u is a vector having all its elements except the first zero, C is the hermitian matrix containing the eigenvectors (in columns) which are mutually orthogonal i.e. $(C^*)^T = C^{-1}$, and the term between brackets denotes a diagonal matrix.
The intensities are subsequently obtained from multiplying the elements of the vector v with their complex conjugate.

4.2.6 The treatment of absorption.

In the phenomenological treatment of absorption by inelastic scattering of the incoming electrons, two mechanisms are generally thought to describe the process [Humphreys 1979]. First we have the single and collective electron excitation (plasmon interaction), and secondly the collective atom excitation (phonon interaction). It is not the intention to treat both effects separately, but to consider the effect of inelastic scattering resulting in a loss in the electron flux one way or the other.
In analogy to the description of absorption in optics Yoshioka [1957] showed that the effect of inelastic scattering can be described by the addition of a complex component to the crystal potential

$$V^{eff}(\underline{r}) \rightarrow V(\underline{r}) + iV'(\underline{r}) \qquad\qquad 4.2.35$$

where $V(\underline{r})$ is the elastic contribution and $V'(\underline{r})$ the inelastic contribution.

As has been shown by Humphreys and Hirsch [1968], the magnitude of the complex component is typically less than or equal to one-tenth of the real potential.

Similarly we write for the reduced fourier potentials

$$U_g \rightarrow U_g + iU'_g \qquad\qquad 4.2.36$$

Accordingly, since the potential in the Schrödinger equation is made complex, the resulting Bloch wave vectors inside the crystal will become complex. We write

$$\underline{k}^{(j)} \rightarrow \underline{k}^{(j)} + i\underline{q}^{(j)} \qquad\qquad 4.2.37$$

From the boundary conditions (conservation of the tangential component of the incoming wave vector inside the crystal) it follows that the direction of $\underline{q}$ will be parallel to the zone axis. To obtain the equation for the total wave function we expand eq. 4.2.20 by substituting eqs. 4.2.36 and 4.2.37, giving

$$\Psi(\underline{r}) = \Sigma_j C_0^{*(j)} \Sigma_g C_g^{(j)} \exp 2\pi i (\underline{k}^{(j)}+\underline{g}).\underline{r} \ \exp(-2\pi q^{(j)}.z)$$

$$\dots\dots 4.2.38$$

and it is seen that the excitation coefficients of the individual Bloch waves are exponentially attenuated:

$$C_0^{*(j)}(z) = C_0^{*(j)} \exp(-2\pi q^{(j)}.z) \qquad\qquad 4.2.39$$

In section 4.2.3 it has been mentioned that, as a result of the introduction of inelastic scattering into the calculations, the eigenmatrix becomes general complex (centro-symmetry not considered), having complex eigenvalues and mutual bi-orthogonal complex eigenvectors.

Since the eigenvalue/vector evaluation of such a matrix is a time consuming process (for the calculation of the Bloch wave amplitudes even the eigenvectors of the transposed eigenmatrix have to be calculated), the effect of inelastic scattering is treated by perturbation methods. Because $V'(\underline{r})$ is typically ≤ 0.1 $V(\underline{r})$, it will, therefore, yield a good approximation [Humphreys 1979].

It can be established that the values $q^{(j)}$, including HOLZ interactions, is obtained from

$$q^{(j)} = \Sigma_g \Sigma_h \; U_{g-h}'/(2(K+g_z)) \; C_g^{*(j)} C_h^{(j)} \qquad 4.2.40$$

In matrix notation this equation becomes

$$\mathbf{q} = \mathbf{C}^{-1} \; \{\{U_{g-h}'/(2(K+g_z))\}\} \; \mathbf{C} \qquad 4.2.41$$

where $\mathbf{q}$ denotes a vector having the values $q^{(j)}$ as its elements, $\mathbf{C}$ the eigenvector matrix and the term between brackets a square matrix having its elements given by the indicated expression.

Finally, the amplitudes of the diffracted beams for reflections g are calculated by (c.f. eq. 4.2.32) [Blom & Schapink 1985]

$$v_g(z) = \Sigma_j \; C_0^{*(j)} \; C_g^{(j)} \exp 2\pi i (k_z^{(j)} + g_z).z \times$$
$$\exp(-2\pi q^{(j)} z) \qquad 4.2.42$$

The non-degenerate perturbation method is valid under the limitations of having a set of non-degenerate eigenvalues. In the case of degenerate eigenvalues (occurring in symmetrical cases and in case of the 'critical voltage' effect), the actual general complex eigenmatrix has to be solved or a degenerate perturbation method has to be used [Sprague & Wilkens 1970].
To perform accurate calculations (e.g. crystal potentials and charge densities) the unperturbed method of evaluating the eigenvalue problem has to be used [Humphreys 1979]. On the other hand, it has been shown by Jones et al. [1977] that, in the calculations involving intensity profiles using the non-degenerate perturbation method, no appreciable differences occur compared to calculations using degenerate perturbation methods (which is equivalent to the diagonalization of the general complex eigenmatrix).
Consequently, the calculations described in this thesis are based on the non-degenerate perturbation method, provided that inelastic scattering plays a role, even in cases where a degeneracy in eigenvalues occurs.

4.3   The Bloch wave method versus the multi-slice method.

4.3.1 The multi-slice method.

A second method for the description of dynamical diffraction is the multi-slice method originally developed by Cowley and Moodie [1957, 1958, 1959a, 1959b].
The wave field emerging at the exit face of a crystal of thickness t can be found by considering the propagation of the wave field through m consecutive slices of the crystal with thickness δz, with $m\delta z=t$. The phase changes of the wave field can be described by a transmission function $q_n(\underline{r})$ describing the phase changes resulting from the crystal potential field in the nth slice, and a propagation function $p_n(\underline{r})$ describing the phase changes caused by propagation of the wave field (free space propagation).
The consecutive slices do not have to be of equal thickness, but from a computational point of view it is an advantage to choose the thickness in such a way that the transmission function and the propagation function remain unchanged when considering the transmission through a slice [Self et al. 1983].
Following Huygens' principle the wave function after the nth slice is given by

$$\Psi_n(\underline{r}) = (\Psi_{n-1}(\underline{r}) @ p_n(\underline{r})) \cdot q_n(\underline{r}) \qquad 4.3.1$$

where the symbol @ denotes a convolution.
The solution to the problem is exact in the limit of m going to infinity and δz going to zero, such that $m\delta z=t$. From this point of view the finite thickness δz must be chosen in such a way that the error introduced by the use of a finite slice will be negligible.
Since we are dealing with a 2-dimensional problem, we take $\underline{r}=(x,y)$ in eq. 4.3.1. The transmission function is taken as a phase grating function given by

$$q_n(x,y) = \exp(i\sigma\tilde{\varphi}_n(x,y)\delta z) \qquad 4.3.2$$

where $\tilde{\varphi}_n(x,y)$ is the mean crystal potential per unit length projected on a plane at the centre of the slice perpendicular to the zone axis (c.f. section 2.2.4 where the projected potential is defined) [Goodman & Moodie 1974, Dawson et al. 1974] and σ is the relativistic interaction coefficient. Values for σ are given by Doyle and Cowley [1974].
Similar to eq. 2.2.5 we write for the mean crystal potential per unit length (in case of the projection approximation)

$$\xi(x,y) = \sum_h \sum_k V_{hk0} \exp(-2\pi i(hx+ky)) \qquad 4.3.3^{+}$$

where x and y are expressed in fractional coordinates of a unit cell having its c-axis along the zone axis and therefore the a^{*} and b^{*} axes in the plane of projection.

The propagation function, for convenience expressed in reciprocal space, is given by

$$P(h,k) = \exp(2\pi i\ \xi(h,k)\delta z) \qquad 4.3.4^{+}$$

where P(h,k) is the fourier transform of p(x,y) and ξ(h,k) is the excitation error of the reflection (h,k), i.e. the distance parallel to the zone axis of the reflection (h,k) from the Ewald sphere.

The starting point in the calculations is the second slice, since the wave function emerging from the first slice is simply given by q_1(x,y). The recursive evaluation of eq. 4.3.1 finally results in the amplitudes of the diffracted beams provided that the fourier transformation of the wave function is taken as the final step. Therefore, it will be a more convenient way to treat eq. 4.3.1 in terms of reciprocal space quantities as

$$\Psi_n(h,k) = \mathcal{F}\{\mathcal{F}^{-1} [\ \Psi_{n-1}(h,k).P(h,k)].q_n(x,y)\}$$

$$....4.3.5$$

where $\mathcal{F}$ and $\mathcal{F}^{-1}$ denote the fourier transform and the inverse fourier transform respectively.

Apparently, the calculations involve two fourier transformations per slice, apart from the initialization of the functions P(h,k) (or p(x,y)) and Q_n(h,k) (or q_n(x,y)).

In order to obtain a good approximation using the multi-slice method with only a limited number of slices, tests are available to get optimal results in such cases [Moodie 1965, Anstis 1977, Shannon 1978].

The introduction of an absorption correction is applied in analogy to that of the Bloch wave method by considering the crystal potential to be changed by an additional inelastic component (c.f. eq. 4.2.35)

$$V^{eff}(\underline{r}) \rightarrow V(\underline{r}) + iV'(\underline{r}) \qquad 4.2.35$$

where $V(\underline{r})$ is the elastic contribution and $V'(\underline{r})$ the inelastic contribution. The effect of absorption, $(V'(\underline{r}) \leq 0.1\ V(\underline{r}))$ can be incorporated in the phase grating function.

+ The subscript n has been omitted since the phase grating function is assumed to be equal for each slice considered.

HOLZ interactions are introduced using the phase grating function. The construction of the phase grating function (in direct space) involves the following integration for each slice n [Goodman & Moodie 1974]

$$P_{\$_n}(x,y) = \int_{z}^{z+\delta z} V(x,y,z) \, dz = \$_n(x,y)\delta z \qquad 4.3.6^+$$

where $V(x,y,z)$ is the potential distribution within the slice (c.f. eq. 2.2.4). The slice thickness δz is chosen in such a way that it is not correlated to the repeat distance c in the z-direction. Hence, it can be taken either greater or smaller than c, resulting in a mean crystal potential distribution different for each slice. If the slice thickness just equals the repeat distance c then it can be shown that the mean crystal potential per unit length ($\$_n(x,y)$) is given by eq. 4.3.3, i.e. no HOLZ effects are taken in to account (see also section 2.2.4).
Another possibility is taking the slice thickness δz less than the repeat distance c. Equivalently to eq. 4.3.3 we then define [Self et al. 1983]

$$\$_n(x,y) = \Sigma_h\Sigma_k\Sigma_l \, V_{hkl} \, \exp(-2\pi i(hx+ky)) \times$$

$$\exp(-2\pi i ln\delta z/c) \times \sin(\pi l\delta z/c)/(\pi l\delta z/c) \qquad 4.3.7$$

From a computational point of view it will be convenient to choose δz as an integer multiple of c. The projected potential function will then repeat itself within a (few) number of slices. On the other hand, care must be taken that 'false' HOLZ effects might be introduced [Goodman & Moodie 1974]. If in eq. 4.3.4 the excitation error $\xi(h,k)$ is just equal to (a multiple of) $1/\delta z$ the propagation of this reflection is reinforced [Lynch 1971] introducing 'false' HOLZ effects. In this case the slice thickness has to be reduced.

4.3.2 A comparison between the Bloch wave method and the multi-slice method.

In order to decide which of the methods described above is most suitable for the simulation of CBED patterns, a comparison is made between the Bloch wave method and the multi-slice method. Since it is not the intention and subject of this thesis to give

---

+ The left-hand side of eq. 4.3.6, the projected crystal potential, is expressed in [V][Å] and has therefore been indicated with a superscript p in order to distinguish it from the mean crystal potential per unit length, which is used in the phase grating function eq. 4.3.2.

an overview on the differences and similarities of both methods, the reason for deciding to use the Bloch wave method as the physical basis for the simulations, is treated from the point of view of its application.

Both the Bloch wave method and the multi-slice method have been used extensively in simulation processes on digital computers and, as a result, a lot is known about the differences and similarities between both methods [Self et al. 1983, Goodman & Moodie 1974, Shannon 1978, Cowley 1975]. As a matter of fact, it has been proven that equivalent calculations with both methods based on 49 reflections do not show differences larger than 10^{-5} of the intensities [Cowley 1975][+], confirming the similarity in result.

From a computational point of view, both methods differ considerably. The evaluation of an eigenvalue problem as in the Bloch wave method is proportional to N^3, where N denotes the number of reflections taken into account. For the multi-slice method the equivalent is proportional to $N_2 \log N$ [Self et al. 1983] when using a FFT algorithm and taking N as a power of 2. The total calculation time needed for one slice is then of the order of $2N_2 \log 2N$ [Ishizuka & Uyeda 1977]. Generally, the multi-slice method will be faster for calculations involving 16 reflections or more [Self et al. 1983]. On the other hand, if the thickness of the specimen increases, the number of slices will increase accordingly. The advantage of computation time in the multi-slice method over the Bloch wave method is then decreased.

In summary, it can be said that both methods give identical results and could therefore be used for the simulation of CBED patterns. They are both suited for the introduction of local defects from the perfect crystal structure. From a computational point of view, the multi slice method is more suitable.

The main objective in the simulation of CBED patterns has been the introduction of HOLZ interactions into the calculations. Compared with the multi-slice method, the Bloch wave method is clearly more suitable for this purpose.

[+] Cowley ('Diffraction Physics',1975,p239) mentions here the unpublished work of Fisher,Turner and Warburton in 1968. Whether the work included the effect of HOLZ interactions is not known to the present author.

B. Implementation.

4.4 Introduction.

Having described the physical basis of the program for simulating CBED patterns in detail, the next step in the development of the program is the implementation of the theory. It is not the intention to give a detailed description of the program itself, but rather to give a synopsis of how it has been constructed and to emphasize some points which have not yet been dealt with in the first part of this chapter.

Section 4.5 deals with the program construction and the program flow. The different forms with respect to output, i.e. the way the calculated data are displayed and offered to the user, are treated in detail. In addition, some sections have been included in order to give a closer look at certain specific parts in the program. For instance, the way in which the CB-cone is constructed, the use of the parameters, considerations on the CSL-transformation and finally some aspects on the eigenmatrix setup are treated respectively.

In section 4.6 some remarks are made on the diagonalization of the eigenmatrix and the choice of FORTRAN. An important part of this section is reserved for the processing of the calculated results, i.e. the way they are displayed, the resolution obtained and the accuracy of the calculated data in connection with symmetry relations in the CBED pattern.

Finally, before presenting the simulations, some preliminary remarks are made on the differences between the calculated patterns and the experimentally observed patterns.

The computer program, in its present state, is written in FORTRAN77 and has been operational on the Amdahl 470 mainframe of the Delft University of Technology (this mainframe has been replaced by an IBM 3083 mainframe in June 1985) and on the CYBER 205 supercomputer of the Stichting Academisch Rekencentrum Amsterdam (SARA). The use of the CYBER 205 involved the vectorization of certain parts of the program, which will be dealt with in more detail in section 4.6.3.

At present, the program uses 2500 kB of memory when compiled with a maximum allowed number of 200 reflections. When less reflections are required, the program can be re-compiled with smaller array dimensions, thereby reducing the memory needed.

A Versatec 1200-A electrostatic plotter of the Department of Technische Natuurkunde, section Pattern Recognition, has been used to visualize the calculated CBED patterns. The plotter has a total of sixteen different greylevels.

4.5 Program construction.

4.5.1 Program flow.

The program has been constructed in such a way that it can be used in the treatment of the most general case of crystal specimens belonging to the triclinic crystal class[+].

The program actually consists of four parts (fig 4.5.1). It was apparent from the beginning that the eigenvalue/eigenvector calculation would be the most time-consuming part of the program. This part has, therefore, been used in a batch environment.

Two programs are available to handle the input parameters. One program (CRYSTIO) treats the more rigid parameters, such as unit cell parameters, the reflections hkl used in the calculation in connection with the accelerating voltage of the incident electrons etc.. The other program (SIMIO) treats the parameters that are more often adjusted, such as the specimen definition and the form in which the output is desired. A detailed description of the input parameters is given in section 4.5.4.

Both CRYSTIO and SIMIO operate interactively. They are based on the input of some simple instructions defining the input parameters for program EIGSIM.

Program EIGSIM is the most important part of the program package. Figure 4.5.2 shows the flow-chart of program EIGSIM. The following program blocks can be distinguished.

If a CSL transformation is involved, the new unit cell dimensions in direct and reciprocal space are first calculated. In addition, the original reflections $\underline{h}$ and the atomic positions are transformed to the coordinate system of the CSL. In cases where the CSL transformations includes a unit cell enlargement ($\Sigma > 1$), additional atoms are generated.

The second block involves the extension of data in the case of a bicrystal specimen. The set of reflections $\underline{h}$ is extended with the reflections $R\underline{h}$ (R denoting the rotation-relationship between crystal I and crystal II), non-common to the set {h}. Subsequently, the atomic positions of the second part of the bicrystal (crystal II) are generated.

The third part of program EIGSIM involves the actual eigenmatrix setup, the eigenvalue/vector evaluation and the amplitude calculation. The eigenmatrix is first set up for each infinitesimal, parallel, incoming beam direction within the CB-cone. In addition, the eigenvalues and eigenvectors are calculated and the resulting amplitudes are evaluated for a certain thickness of the specimen. This sequence is repeated for crystal II, for the case of a bicrystal, ; the total thickness of the specimen is then divided into two parts, one in connection with crystal I and the other in connection with crystal II.

[+] Appendix A gives a survey on the general transformations in an oblique coordinate system. In table 2.1 the geometrical relations for the triclinic crystal class are summarized.
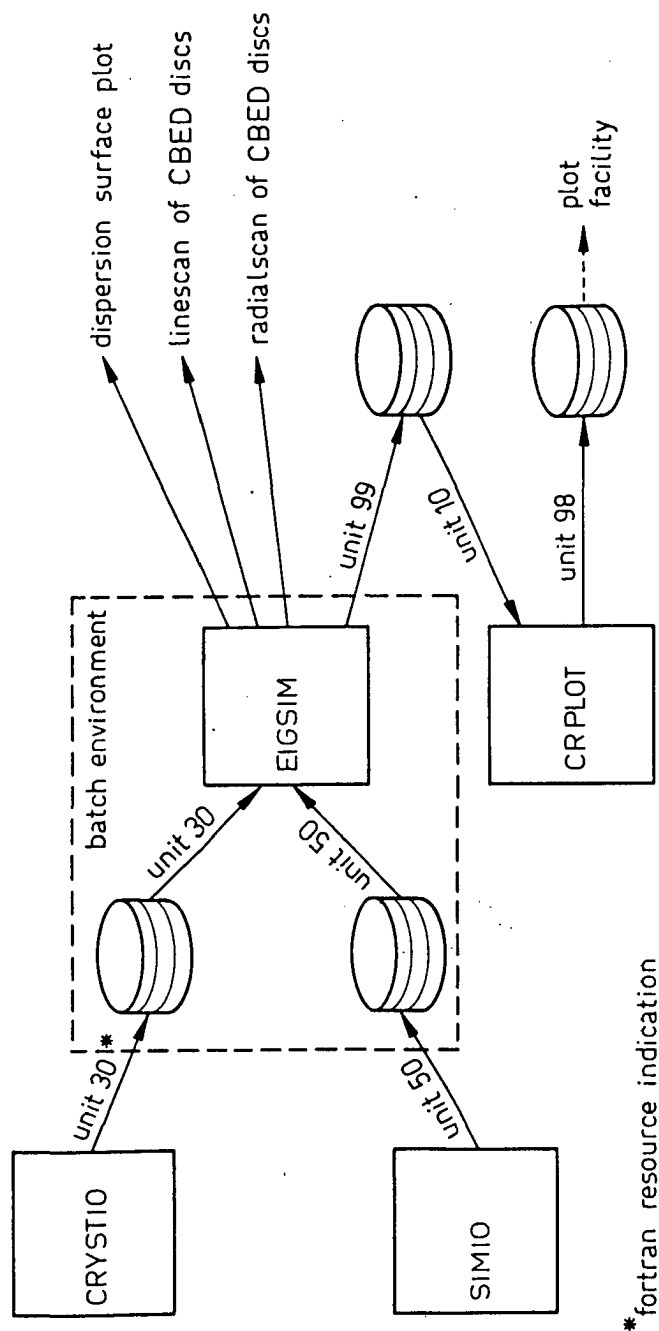
figure 4.5.1

Block diagram illustrating the construction of the program
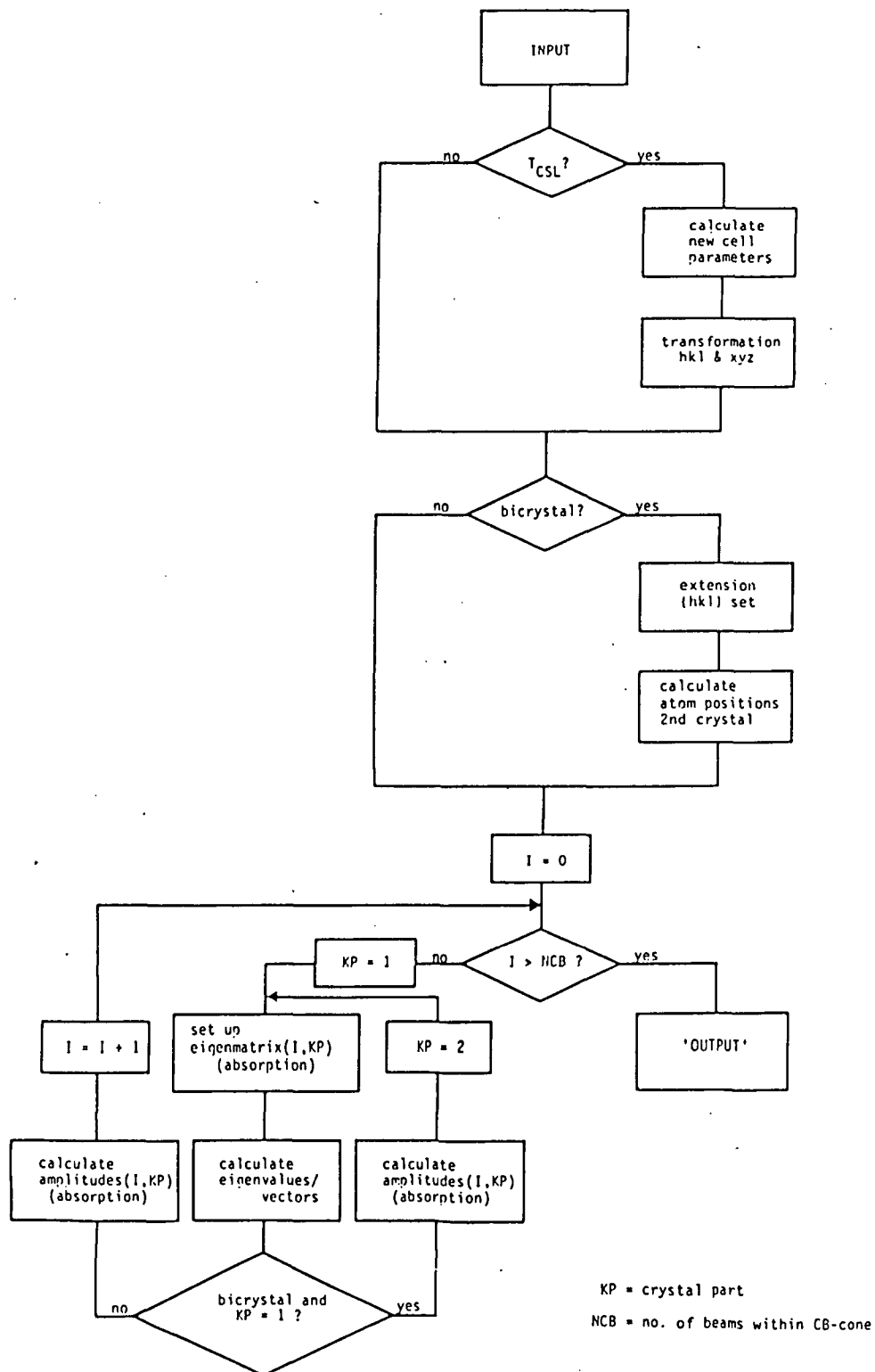for the simulation of CBED patterns.

figure 4.5.2

Flow-chart of program EIGSIM

Finally, when the number of incoming beam directions reaches the number with which the convergent beam is described, the loop is terminated.
It is evident, depending on the number of reflections taken into account and depending on the number of beams with which the CB-cone is described, that the use of program EIGSIM involves a large computation time. It is observed that the eigenvalue/vector evaluation and the amplitude calculation are the most time consuming parts of the program.

4.5.2 Presentation of the output.

There are five different forms of output that can result from the EIGSIM program. Two of them involve the visualization of the results. The other three involve plotting line-scans through the diffraction discs or plotting cross-sections of the dispersion surface.
In considering visualization, it has been the intention to be able to compare the simulated results with the experimental results. Since, in experimental cases, the greylevel of photographic material is related logarithmically to the incident intensity, the calculated intensities are transformed using (D-values)

$$D = \log(I) \qquad\qquad 4.5.1$$

The different forms of output are treated individually here below.

1) XY-plot.

A rectangular grid is used to describe the incident convergent beam (figure 4.5.3a). Each gridpoint symbolises the tangential vector component of the incoming beam direction (i.e. k_t). The D-value is calculated for each gridpoint within each diffraction disc. Finally, the D-values are assigned a certain greyvalue; they are converted to integer values within a certain greylevel scale. The gridpoint density can be chosen arbitrarily; a default grid of 64*64 is implemented. Section 4.5.3 treats the use of the grid in more detail.

The range of the greylevel scale is dependent on the output device that has been used for displaying the plots, for instance, a line-printer. By superimposing certain symbols (letters,numbers etc.) the suggestion of different greylevels can be obtained. In this case the greyvalues were based on a 21 greylevel scale.
The method used most extensively has been a TV-monitor connected to a dedicated system for image manipulation, controlled by a HP1000 computer system. The individual picture elements (pixels) can be directed with 8 bits deep, equivalent to a range of 256 different greyvalues. The hardware limits the size of the images

to a maximum of 256*256 pixels. Since, in all cases, the calculated plots involve images of 64*64 pixels, a linear 4 nearest-neighbour interpolation has been performed in order to obtain 256*256 images.

To obtain a hard copy of the video screen, a Versatec 1200-A electrostatic plotter was used. This plotter has only a 16 greylevel basis. Thus, the resolution that can be obtained with the video display is inevitably reduced, when a hardcopy of it is taken (see also section 4.6.4).

The images that are obtained show the contrast of the micrograph images resulting from the electron microscope, i.e. to eliminate confusion, they have the inverse contrast of the images seen on the fluorescent screen of the electron microscope.

2) RPHI-plot.

A radial grid is used to describe the incident convergent beam (fig. 4.5.3b). Each gridpoint symbolises a certain incoming beam direction by its tangential vector component k_t. The CB-cone is scanned radially, i.e. in steps along R and along φ. For each gridpoint the D-value is calculated.

To obtain 'true' images of the diffraction discs the results should be plotted in the same radial fashion. As it has not been possible to output the data in this format, the radial grid is tranformed to a rectangular grid with the horizontal axis coincident with the φ-axis and the vertical axis coincident with the R-axis. As a result the image of the diffraction disc is 'unfolded'. Subsequently, the image are treated in the same way as an XY-plot. The gridpoint density of the radial grid can be chosen arbitrarily; a default grid of 64*64 is used.

The reason for the implementation of the Rphi-plot facility arises from the fact that rotational symmetry might get lost when using the XY-plot facility. One method to overcome this observation is to take a higher resolution of the XY grid, with the consequence that the computation time increases. A much simpler solution is to apply the radial grid as described. Rotational symmetry can then be detected with a minimum of a 12-points resolution along φ, and even mirror symmetry is detected if the resolution of the applied grid is sufficient.

A disadvantage in the use of the radial grid is the way the Rphi-plot is displayed; because the image is 'unfolded', the result has lost its direct connection with the discs observed in CBED patterns.

A difficulty in the implementation of both the XY-grid and Rphi-grid, in connection with the possibility of using varying grid resolutions, has been the memory allocation. To reduce the allocation of core-memory, at certain steps in the program, the resulting intensities calculated up to that point are written to background memory. As a consequence, for images having more than 360 pixels, different parts of one image reside on different parts of background memory. Program CRPLOT is used to re-organize the data in such a way that blocks of one image are obtained.

3) Line-scan.

As an alternative to the plot facilities, a simple line-scan of a
diffraction disc can be obtained. The direction of scanning is
indicated by a lattice vector of the ZOLZ plane; the scanning
takes place over the diameter of the disc. The line-scan option
is very useful to detect the presence of a mirror plane in a
certain direction. The scanning direction must then, of course,
be perpendicular to the mirror plane direction.
Since in the line-scan option, usually only a limited number of
incoming beam directions within the CB-cone are taken, the
computation time is reduced considerably, for possibly the same
information on the symmetry relations within the CBED pattern.

4) Radial-scan.

Equivalent to the line-scan option a radial-scan option is
included. The diffraction discs are scanned in a radial way at a
fraction of the total disc radius, i.e. $R_{r-s} \leq R_{disc}$. This option
can be very useful to detect rotational symmetry elements.
In addition, computation time can be reduced considerably, for
the same reasons as with the line-scan option.

5) Dispersion surface plot.

For each of the incoming beam directions, the associated set of
eigenvalues (or dispersion branches) is calculated and the
eigenvalues are plotted against the tangential component of the
incoming beam direction (c.f. section 4.2.4).
The direction of scanning is indicated by a lattice vector $\underline{g}$
belonging to the ZOLZ plane. The plot, therefore, gives an
intersection of the dispersion surface along $\underline{g}$. The scanning can
be taken either from $\underline{0}$ to $\underline{g}$ or from $-\underline{g}/2$ to $\underline{g}/2$, i.e. the
scanning is over one Brillouin zone.

4.5.3 Convergent-beam description.

As has been mentioned in the previous section, there are two
different grid-types that are used in the calculations to
describe the convergent beam: a rectangular grid and a radial
grid (fig 4.5.3). Each gridpoint (in both types) stands for the
tangential component $\underline{k}_t$ of an incoming beam direction within the
CB-cone. The CB-cone itself is described by its semi-angle and
the deviation from the zone axis. For each vector $\underline{k}_t$ (or, in
other words, for each gridpoint) the associated intensity (and
subsequently its D-value) is calculated.
The gridpoints are expressed in terms of the reciprocal crystal
lattice. Firstly, the centre of the grid is taken to be
coincident with the origin of the reciprocal lattice. Secondly,
the orientation of the grid is taken such that each gridpoint is
expressed in terms of a reciprocal lattice vector lying in the

ZOLZ plane of interest. The choice of this orientation is immaterial. Finally, the vectors are scaled to vectors in terms of units of k_t.

The density of the applied grid (either XY or Rphi), i.e. the number of gridpoints within the angle of convergence, is directly proportional to the amount of detail that is obtained. On the other hand, a higher resolution results in an increase of the computation time (and therefore in a decrease in throughput on multi-user systems). A more detailed discussion on computational aspects in general is given in section 4.6.2.

a   b
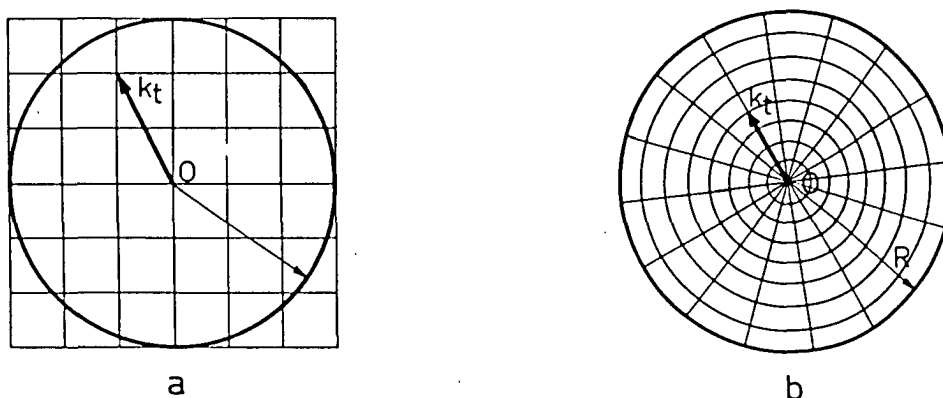
figure 4.5.3

The different gridtypes to be used: (a) rectangular grid, (b) radial grid. Each gridpoint symbolises the vector k_t of an incoming beam direction.

4.5.4 Program parameters.

Having treated the different ways in which the results of the calculation can be obtained, the parameters are treated that determine the crystal specimen and the CBED pattern to be calculated, in the following overview.
The program parameters can roughly be divided into two sets of parameters: structure determining and specimen-configuration determining. The two sets will be considered separately.

1) Structure determining parameters.

The crystal structure of the specimen is described by the unit cell and its contents. The unit cell is given by the dimensions a, b, c, α, β and γ; the contents is given by the different atoms of a certain type and their position within the unit cell expressed in relative coordinates. Since there is no automatic generation of the space group symmetry related atoms included, all the atoms in one unit cell have to be specified.
The scattering amplitudes (or scattering factors) of the atoms of a type are introduced using the Cromer-Waber coefficients [Cromer & Waber 1965] for a third degree polynomial approximation of the Xray scattering factors as a function of $\sin\theta/\lambda$. The way in which the Xray scattering factors are related to the electron scattering factors has been treated in section 4.2.2. The electron scattering factors are used for calculating the (reduced) fourier potentials.
The effect of absorption is introduced by a perturbation factor defined by V'/V (see section 4.2.6). The perturbation factor is usually less than, or equal to, 0.1 [Humphreys 1979]. Whether or not absorption is taken into account depends on the atoms in the unit cell; electron scattering is generally more subjected to absorption when heavy atoms are present.
The diffraction pattern to be calculated is given by the zone-axis (zone-axis pattern or ZAP). The subset of reflections hkl of a ZAP used in the calculation determine the degree of approximation of the simulations. Usually, those reflections lying near to, or on, the Ewald sphere are known to contribute to the image formation [Jones et al. 1977]. The radius of the Ewald sphere is determined by the accelerating voltage of the incident electrons. The choice of the accelerating voltage and the choice of the subset of reflections are, therefore, mutually related.

2) Specimen-configuration determining parameters.

In addition to the description of the crystal structure, a specimen is exclusively described by its thickness, since parallel sided boundaries are assumed.
In case of a bicrystal, the relation {R|$\underline{t}$} between crystal I and crystal II is included. The associated CSL is introduced by the transformation matrix T_{CSL}. The position of the interface, expressed as a fraction of the total thickness, determines the individual thickness of the crystals I and II. The range of uniquely different positions of the boundary is between 0 and 0.5. Because of the reciprocity relation, positions of the interface indicated by values above 0.5 is equivalent to the same configuration turned upside down.
The angle of convergence of the incident beam (designated by the semi-angle) in connection with the number of beams with which the convergence is described, determine the amount of detail that will be obtained.
Finally, a deviation parameter determines the orientation of the axis of the incident CB-cone relative to the zone-axis.

4.5.5 The eigenmatrix setup.

As has been seen in section 4.5.1 (fig. 4.5.2), for each (parallel) incident beam direction within the CB-cone, the eigenmatrix has to be set up. Subsequently the eigenvalues and eigenvectors are determined.
The diagonal elements (c.f. eq. 4.2.10) are a function of the incident beam direction. Consequently, these elements have to be evaluated for each incoming beam direction.
The off-diagonal elements, on the other hand, are dependent on the values of U_{g-h} (c.f. eq. 4.2.11). Therefore, they have to be calculated only once (and for a bicrystal, once for each crystal). Due to the hermitian property of the eigenmatrix $(A^{*}=A^{T})$, either the upper or lower triangle is sufficient. In the case where absorption is taken into account, the hermitian property is conserved, since absorption is treated using perturbation methods.

4.5.6 Eigenvalue and eigenvector evaluation.

For the determination of the eigenvalues and eigenvectors of the eigenmatrix, the standard procedure FO2AXF of the NAG-library [Numerical Algorithms Group 1984] of mathematical tools has been used. This routine uses the Householder algorithm for the reduction of the eigenmatrix to a tridiagonal form. In addition, the QL algorithm (an adaptation of the QR algorithm) is applied for the evaluation of the eigenvalues and associated eigenvectors.

4.6   Discussion.

4.6.1 The choice of FORTRAN.

The programming language FORTRAN has been extensively used in scientific application over the last decades. Even after the latest improvements released in FORTRAN77 (FTN5), the language is not as well structured (thereby reducing its readability) as other programming languages such as Pascal, Algol68 and the recently developed language Ada. On the other hand, because of its extensive use, FORTRAN is supported for use on many different types of computer configurations (i.e. portability). In addition, a number of library packages consisting of standard scientific routines (NAG-lib etc.) are known to support the FORTRAN-programmer.

4.6.2 Considerations on computation time.

Because of the large number of eigenvalue/vector problems

involved, computation time is unavoidably increased in a situation where a plot with high resolution is required. In general, from a computational point of view, the algorithms for the evaluation of an eigenvalue problem running on scalar processors are proportional to N^3 if N denotes the dimension of the problem. In the present case, N is equivalent to the number of reflections taken into account. Usually N is in the order of 20-100. In the case of a bicrystal, the number of eigenvalue problems is even doubled.

As has been shown above, electron diffraction in a bicrystal is treated on the basis of the CSL.
An alternative method for the description of electron diffraction involves the treatment of the diffracted beams leaving the first crystal as incoming beams to the second crystal [Sheinin & Corbett 1976, Sutton & Pond 1978]. Defining the number of reflections taken into account to be N_1 and N_2 for the crystals I and II respectively, the computation time using this method will be proportional to $N_1^3 + N_1 N_2^3$ for a single incident beam within the CB-cone. If {g} represents the set of reflections used in crystal I and equivalently {h} the set used in crystal II, the amplitude of a particular reflection 1 is obtained by summing all the contributions of the combinations $\underline{g} + \underline{h} = \underline{1}$ [Sutton & Pond 1978]. In general, the sets {g} and {h} need not necessarily to be equal.
In the CSL method, the reciprocal lattice of the CSL contains all the diffraction vectors common to both crystals that are relevant to diffraction for the bicrystal. The CSL is continuous across the interface; the location of the atoms in the unit cell is different in both crystals. Due to continuity across the interface, the set of reflections taken into account for both crystals will be the same, i.e. the Bloch waves in both crystals will have the same number of components. Therefore, matching at the interface is a simple procedure. Defining the number of reflections to be N_{12}, the computation time will be proportional to $2N_{12}^3$ for each incident beam within the CB-cone, since the eigenvalue problem of dimension N_{12} has to be solved two times, once for each crystal. By analogy to the previous method, the equivalent set of reflections taken into account will be the union of the sets {g} and {h}, transformed to the vector basis of the CSL, i.e. T_{CSL}{g} $\cup$ T_{CSL}{h}.
Both methods, though different in approach, yield the same result when sufficiently large sets {g} and {h} are used in the actual computations. From a computational point of view, both methods are different. The difference in total computation time depends on the relative magnitude of N_1 and N_2 on the one hand and N_{12} on the other. In the limiting case of where no common reflections exist, i.e. when $N_{12} = N_1 + N_2 - 1$, it is easily seen that the CSL method requires less computation time for $N_1 = N_2 > 13$, i.e. $N_{12} > 25$ [Blom & Schapink 1985]. In practice, common reflections are frequently observed. Therefore, the CSL method can become more advantageous for even lower values than indicated.

4.6.3 Implementation on the Cyber 205.

The program for the simulation of CBED patterns has first been made operational on the Amdahl 470 mainframe of the Delft University of Technology. In the course of its use, it was clearly observed that even simple calculations (line-scan etc.) involved large computation times and, therefore, a low throughput of results. With the implementation of the program on the CDC Cyber 205 computer at the Stichting Academisch Rekencentrum Amsterdam (SARA), this disadvantage was overcome.

The Cyber 205 is a vector computer. At SARA a version of the Cyber 205 is installed with one floating-point vector processor. The computer runs using VSOS (Virtual Storage Operaring System). To make optimal use of the vector capability, a large amount of data involving the same operation (addition, multiplication etc.) has to be offered to the vector processor as data from consecutive memory locations, i.e. a vectorization of data. Apart from an initialization period, a result is produced, each clock-cycle. The Cyber 205, having a clock-cycling period of 20ns (clock frequency of 50MHz), is capable of performing 50×10^6 floating-point operations per second (50 Mflop/s) in connection with an operand length of 64 bits [Hwang & Briggs 1984]. With a operand length of 32 bits the peak performance is doubled (100 Mflop/s).

In general, the application of vectorization is useful for the time consuming parts of a program, provided that these parts are suitable to undergo vectorization. In the program described, the time-consuming parts are the eigenvalue/vector evaluation and the intensity calculations based on the eigenvalues and eigenvectors ($\pm$ 90% and $\pm$ 8% of the total computation time on the Amdahl 470, respectively, absorption not included).
It is known that vectorization is most appropriate when using large dimensions of the array data structures. The present problem involves array data structures with dimensions in the order of 20-100. Although not large, compared to the dimensions required to obtain optimal use of the processor capabilities, enough reduction in computation time can be obtained in comparison with simple scalar processing, considering the fact that successive calculations (4000 times or more) have to be performed for one image only. Therefore, the vectorization of parts of the program has been restricted to those parts involving the eigenvalue/vector evaluation and the intensity calculation.

A vector-adapted version of the NAG-library routine F02AXF for the computation of the eigenvalues and eigenvectors has been obtained by the pre-compilation of the routine with the VAST (Vector and Array Syntax Translator) pre-compiler for vectorization. Subsequently, the resulting source code has been compiled with the FTN200 vector compiler. In terms of reduction in computation time, the ultimate result may not be optimal.

The intensity calculation part of the program has been vectorized by re-writing parts of the source code in such a way that data are presented in vectors (reconstruction of computation loops: implicit vectorization). In some parts standard vectorization utilities ('gather' and 'scatter') known to the FTN200 compiler have been implemented to obtain additional vectorization (explicit vectorization). To avoid stride problems the dimensions of certain array data structures (e.g. the eigenmatrix etc.) have been adjusted, for each calculation made, to the number of reflections involved.

The efforts made in vectorization have been effective. An overall reduction in computation time by a factor of 9 has been obtained[+]. Using the Cyber 205, the eigenvalue/vector evaluation and intensity calculation take respectively ± 97% and ± 3% of the total computation time. Therefore, the vectorization of the intensity calculation has been relatively more effective. In the case where absorption is included the values are ± 80% and ± 19%, respectively.

4.6.4 Symmetry detection.

In order to detect any symmetry present in a pattern or part of a pattern, a comparison of numbers (or pixels) has to be made. As an example, figure 4.6.1 shows the result of a radial scan of the 000 disc of a CBED pattern resulting from a simulation of a silicon bicrystal specimen. The interface is a twin boundary ($\Sigma=3$, orientation relation $\{60°|0\}$[++] along $<1\ 1\ 1>$) and is positioned at 0.5 of a total thickness of 2000 Å. The cone of incidence is directed along the $<1\ 1\ 1>$ zone-axis.

From the theory, it follows that the resulting CBED pattern has diffraction group $3m1_R$ (see also next chapter). According to table 2.2, this means that the whole pattern (WP) has symmetry 3m and the central disc (in table 2.2. indicated by BF) has symmetry 6mm. Looking at the third column of figure 4.6.1, it is seen that the sequence of intensities is repeated every 60°, i.e. a six-fold symmetry; the dotted lines indicate mirror operations. Consequently, a 6mm symmetry is present.

On the other hand, it is also observed that the values of symmetry related intensities are not exactly equal in all cases. As has often been found, a discrepancy at the fourth decimal place occurs with symmetry related intensities. Although the symmetry has to be exact, since it is imposed by the symmetry within the specimen, the numerical evaluation imposes its

---

[+] In comparison with the Amdahl 470, a reduction in computation time by a factor of 5 is obtained when the Cyber 205 is operating in scalar mode, i.e. when vectorization is excluded.

[++] This is a short-hand notation of the Seitz operator having a rotation matrix involving a 60° rotation and a zero translation.

```
-.4727E+00   -.7931E+00   0.8524E+00                           — 6°
-.4692E+00   -.8007E+00   0.8613E+00 ---
-.4691E+00   -.8007E+00   0.8613E+00
-.4727E+00   -.7931E+00   0.8524E+00
-.5129E+00   -.7862E+00   0.8812E+00
-.5036E+00   -.7295E+00   0.7856E+00
-.3870E+00   -.5996E+00   0.5093E+00 ---
-.3872E+00   -.5997E+00   0.5096E+00
-.5037E+00   -.7296E+00   0.7861E+00
-.5129E+00   -.7862E+00   0.8811E+00                           —
-.4727E+00   -.7931E+00   0.8524E+00
-.4691E+00   -.8008E+00   0.8613E+00 ---
-.4691E+00   -.8008E+00   0.8613E+00
-.4727E+00   -.7931E+00   0.8524E+00
-.5129E+00   -.7861E+00   0.8811E+00
-.5036E+00   -.7294E+00   0.7856E+00
-.3869E+00   -.5995E+00   0.5091E+00 ---
-.3871E+00   -.5997E+00   0.5094E+00
-.5037E+00   -.7295E+00   0.7859E+00                           —
-.5128E+00   -.7861E+00   0.8810E+00
-.4726E+00   -.7931E+00   0.8523E+00
-.4690E+00   -.8008E+00   0.8613E+00 ---
-.4690E+00   -.8008E+00   0.8612E+00
-.4726E+00   -.7931E+00   0.8523E+00
-.5129E+00   -.7861E+00   0.8810E+00
-.5036E+00   -.7295E+00   0.7857E+00
-.3870E+00   -.5996E+00   0.5093E+00 ---
-.3870E+00   -.5996E+00   0.5092E+00
-.5036E+00   -.7294E+00   0.7857E+00
-.5129E+00   -.7861E+00   0.8810E+00                           —180°
-.4726E+00   -.7931E+00   0.8523E+00
-.4690E+00   -.8008E+00   0.8613E+00 ---
-.4691E+00   -.8008E+00   0.8613E+00
-.4726E+00   -.7931E+00   0.8523E+00
-.5129E+00   -.7861E+00   0.8810E+00
-.5037E+00   -.7295E+00   0.7859E+00
-.3871E+00   -.5997E+00   0.5094E+00 ---
-.3870E+00   -.5995E+00   0.5092E+00
-.5036E+00   -.7294E+00   0.7856E+00
-.5129E+00   -.7861E+00   0.8811E+00                           —
-.4727E+00   -.7930E+00   0.8524E+00
-.4691E+00   -.8006E+00   0.8613E+00 ---
-.4691E+00   -.8008E+00   0.8613E+00
-.4727E+00   -.7931E+00   0.8524E+00
-.5129E+00   -.7861E+00   0.8811E+00
-.5038E+00   -.7296E+00   0.7860E+00
-.3872E+00   -.5997E+00   0.5095E+00 ---
-.3870E+00   -.5996E+00   0.5093E+00
-.5036E+00   -.7294E+00   0.7857E+00
-.5130E+00   -.7861E+00   0.8811E+00                           —
-.4727E+00   -.7930E+00   0.8524E+00
-.4692E+00   -.8007E+00   0.8613E+00 ---
-.4692E+00   -.8007E+00   0.8613E+00
-.4727E+00   -.7930E+00   0.8524E+00
-.5129E+00   -.7862E+00   0.8811E+00
-.5037E+00   -.7295E+00   0.7860E+00
-.3871E+00   -.5997E+00   0.5095E+00 ---
-.3871E+00   -.5996E+00   0.5095E+00
-.5037E+00   -.7295E+00   0.7859E+00
-.5129E+00    7862E+00   0.8012E+00                           —360°
```

figure 4.6.1

An intensity profile of the 000 disc of a Si-bicrystal specimen using the radial-scan method. The interface is positioned at 0.5 of the total thickness (2000 Å). Columns 1 and 2 give the real and imaginary part of the amplitude, column 3 shows the intensity. A 6mm symmetry is observed. --- indicates a mirror operation.

limitations on the precision. Intensities which are related by symmetry, but which have different values, are said to be numerically equivalent.

A general and satisfactory criterion for numerical equivalence is difficult to establish. It depends on the hardware presentation of the data and the accuracy of the algorithms used. Therefore, it will be different for each environment in which the programs are executed. In the presently used computer configuration, deviations in the fourth decimal place between symmetry related intensities have been commonly observed; in case of absorption the effect is already apparent in the second decimal place.

From this point of view, it can be said that the detection of symmetry elements within the pattern using computational methods will involve elaborate ('errorfree') algorithms covering the relation of symmetry in connection to numerical equivalence.

The best method for presenting the calculated results is to display them using the XY-plot and RPHI-plot methods described. One advantage compared to the line-scan and radial-scan methods is its direct connection with the experimentally obtained results. If the resolution of the applied grid has been sufficient, even fine details can be compared.

Additionally, the human eye is known to be sensitive for pattern regularities, i.e. patterns involving some kind of symmetry. Therefore displaying the plots in the way described, enables the observer to detect symmetry at a glance.

As has been mentioned earlier, the amount of detail that is obtained is, firstly, dependent on the resolution of the applied grid. Secondly, the amount of detail obtained is dependent on the greylevel resolution. In fact, symmetry might be obscured, if the amount of detail is too low. Consequently, one has to be aware that sufficient greylevels are used to display the image. In principle, the amount of detail obtained is proportional to the number of greylevels within the greylevel-scale. In practice, limitations are imposed by the number of greylevels of the device on which the plots are displayed. In the present case a TV monitor has been used. It is known that even for high quality TV monitors the sensitivity of the combination display-device/observer, indicated by the perceived dynamic range (PDR), is about 110 just noticeable differences (JND's) across the dynamic range of the display [Pizer et al. 1982]. Therefore, the use of a greylevel-basis consisting of 256 greylevels is assumed more than adequate.

A reduction of the number of greylevels within the greylevel-basis has been inevitable when a hardcopy of the monitor screen is made, causing a discrease in detail. In this case, care has to be taken, since a decrease in detail can also artificially generate symmetry.

Using the radial-scan method, it is possible to deduce radial symmetry reasonably easily. To observe mirror symmetry using this method is, on the other hand, more difficult. A mirror can be detected if the resolution along φ is increased. If, in advance, the position of the mirror plane is known (or presumed), the line-scan method is preferred.

4.6.5 Limitations with respect to the calculated CBED patterns.

In view of the next chapter in which the calculated results are presented, a few remarks on the differences between the calculated and experimental results are made in this section; they are known in advance and relate to all the presented simulations. The topics described here will therefore not be re-examined in the next chapter.

Firstly, the simulations are an approximation of the experiment, since the number of reflections and type of reflections (i.e. their indices) determine the degree of approximation. In the calculations, the set of reflections used is assumed to be the limiting set contributing to diffraction.
Secondly, in the case of a bicrystal, the local rearrangement of individual atoms near the interface to energetically preferred positions (atomshuffles) is not taken into account. Since only a few atom-layers are assumed to be involved in this process, its contribution to the pattern formation is considered to be negligible, compared to the contribution of the major part of the specimen.
Thirdly, the mutual overlap of the diffraction discs, if present, is not taken into account. A large unit cell of the (CSL) lattice in combination with a large angle of convergence of the incident beam can give rise to partial overlap of diffraction discs. The diffraction in the directions k_1+g_1 and k_2+g_2 converging at the same place in the diffraction pattern are treated independently. Therefore, discs that overlap in the experiment are simulated as though they do not overlap, i.e. an infinite camera length is presumed. Experimentally, overlap of the diffraction discs can be avoided using the Tanaka method [Tanaka et al. 1980].
Finally, double (or multiple) diffraction can be simulated provided that the effect is introduced into the calculations. All the reflections contributing to a case of double or multiple diffraction must be included in the calculation.

According to its definition, the concept of simulation can be formulated as [DSTT 1974]

Simulation : 'An imitation of some or all of the behaviour of one system with a different, dissimilar system.'

Although this formulation is not considered to be the most complete description of the concept of simulation, it is sufficient to be used as an analogy for the treatment of the different subjects presented in this chapter.
The system to be simulated, i.e. the 'one system' in the formulation, is the complex of a crystal specimen that is subjected to an incident (convergent) electron beam, the result of which is a (convergent beam) diffraction pattern.
The different dissimilar system is some kind of model ('simulation model') which can be used as the analogy of the

complex process described above. In the present case, the simulation model basically consists of three parts, mutually linked together: a description of the specimen, a description of the diffraction process and a description (presentation) of the results. The limitations of the simulation model determine the degree of imitation obtained.

Limitations are obtained using a computer for the calculation of the results. Although the computer is assumed to be merely a tool rather than a constituent part of the simulation model, it imposes its own limitations.
Firstly, the dynamical theory allows an infinite number of reflections to be taken into account. A large number of reflections taken into account is, as has been mentioned, impractical, both from the point of memory allocation as well as from the point of view of computation time (see also section 4.6.2.).
Secondly, the computer imposes its limitations on the display of the results. The number of greylevels used for the imaging of the intensities determine the correspondence between experimental and calculated results (see also section 4.6.4).
Thirdly, the convergent beam is described by a number of parallel incident beams having different incoming directions. In considering computation time, this number is limited. (see also section 4.5.3).

A different type of limitation is observed in the description of the diffraction process. Although, these are considered to be side effects, they are worth mentioning. The diffraction process is treated using the dynamical theory of diffraction originally developed by Bethe [1928]. As has been shown the dynamical theory describes a great deal of the features observed in electron diffraction. Only a few of the observations, for instance, Kikuchi lines and background scattering, cannot be described using the dynamical theory. The dynamical theory of diffraction also imposes its limitations on the description of the specimen. For instance, local thickness variations seen by a finite probe size of the incident beam, cannot be treated.

Having considered the above arguments, it is relevant to ask to what extent the (complex) model is indeed an imitation of the experiment. Using the dynamical theory of diffraction, we have a quantitative analogy of the diffraction process. Although we have lost a one to one imitation of the diffraction process, the analogy is assumed to be sufficient to justify the use of the term simulation in the present case [Shannon 1975]. As will be seen in the forthcoming chapter, the presented results are an imitation of the experiment, within the limitations described above. They offer, on the other hand, sufficient information to draw conclusions about the nature of the simulated systems.

Chapter 5 : Comparison of computer-generated and experimental CBED patterns.

5.1 Introduction.

In this chapter simulations of CBED patterns are presented and discussed. Most of the computer calculated images shown, involve simulations of the central (000) disc of the CBED pattern. Where possible, a comparison is made with the equivalent image using electron microscopy.
The results that are presented describe different sets of parameters in crystal structure (Si, GaAs or Au) and/or specimen type (bicrystal or single crystal, thickness variations, etc.). Each result is presented in a different section including a discussion on the topic in question. In each section only the most important parameters will be mentioned; appendix C gives the complete set of parameters used in each of the calculations.
The topics treated in this chapter are simulations on :

1) Silicon, single crystal specimen.
   The simple case of a single crystal specimen is used for testing the computer program.
2) Thickness variations.
   The effect of specimen thickness on the pattern profile is illustrated with the example of single crystals of gold.
3) The effect of absorption.
   The application of perturbation methods, in order to deal with absorption, is illustrated with the example of single crystals of gold.
   The influence of absorption on the symmetry relations in the pattern, that are observed as a result of reciprocity, is treated for single crystal and bicrystal specimens.
4) Variations in the position of a twin boundary in a silicon bicrystal specimen.
5) Bicrystal specimens of silicon containing an additional translation component in the description of the orientation relation of the crystal parts. The effect of translation on the symmetry of the CBED pattern is treated.
6) A bicrystal specimen of gold having a $\Sigma=7$ type twist boundary.
7) The Tanaka method.

The last section of this chapter deals with a general discussion on the results presented. Conclusions concerning the comparison between the computed and the experimental images are made. In addition, some comments are made on the extent to which an approximation of the experimental observations is obtained.

All the calculated images that are presented are a hard copy of the video screen and have been made using a Versatec 1200-A electrostatic plotter. The resulting images are based on a 16 greylevel range. All the experimental results presented have been obtained using a Philips EM400T electron microscope.

5.2 Results.

5.2.1 Silicon single crystal specimens.

An essential step in the development of a new technique is the testing phase. When applied to the present case, i.e. the development of a computer program for the simulation of CBED patterns, the computed results have, at some stage, to be compared with the experimental results, i.e. with CBED patterns obtained from the electron microscope using specimens similar to the specimen-model used in computations. In addition, the conditions of the electron beam, i.e. the angle of convergence of the incident beam and the accelerating voltage used, must be equivalent.

The most simple system to consider is performing calculations based on a single crystal specimen. Convergent beam patterns taken from single crystal specimens of silicon are known to clearly show the HOLZ lines intersecting the (000) disc. Figure 5.2.1 shows an experimental image of the (000) disc of the CBED pattern of silicon taken along the <1 1 1> zone axis at 100 kV. The HOLZ lines are indexed accordingly (the indexing of the HOLZ lines is limited to the FOLZ lines). To give an example of the usefulness of the HOLZ line pattern, the position of the HOLZ
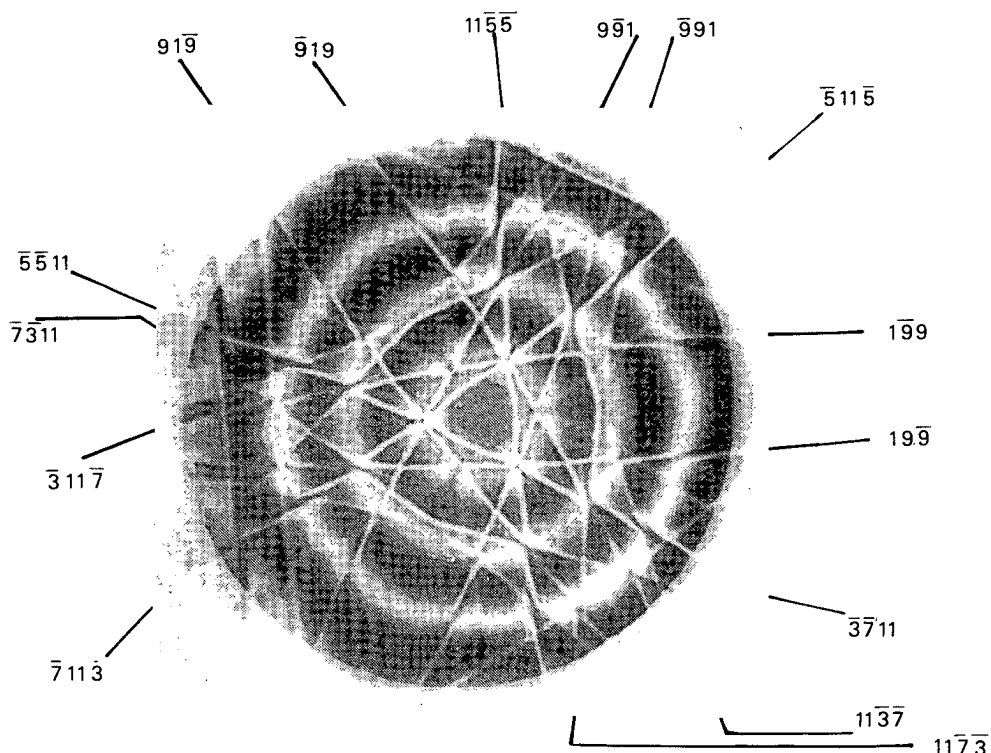
figure 5.2.1

Experimental image of the (000) disc of a <1 1 1> ZAP CBED pattern taken at 100 kV. Clearly visible is the HOLZ line pattern within the disc. The HOLZ lines are indexed accordingly.

lines can be used to obtain an accurate determination of lattice parameters as a function of, for instance, the temperature. The position of the HOLZ lines must then, of course, be corrected for dynamical effects [Jones et al. 1977].
Kinematically, it is easily shown that the position of the HOLZ lines shift with varying accelerating voltage. Experimentally, it has been shown [Jones et al. 1977] that the three <5 5 11> FOLZ lines shift from their positions at 100 kV to intersect exactly at the centre of the (000) disc at 102.7 kV. This effect can clearly be seen in figure 5.2.1 and 5.2.2' respectively. This behaviour gives, therefore, an excellent opportunity for testing the simulation program. The computed image is shown in figure 5.2.3a. The image has been calculated using 22 reflections, 9 of which belong to the FOLZ of the <1 1 1> zone axis (3×<5 5 11>, 6×<1 9 9̄>. The specimen thickness has been taken to be 2000 Å. The angle of convergence is 0.2⁰, which is different from the angle of convergence in the experimental case of figure 5.2.2 (0.4⁰). For convenience, figure 5.2.3b shows the image of figure 5.2.2 at a different micrograph magnification: thus, figures 5.2.3a and 5.2.3b are directly comparible. In figure 5.2.3a it is seen that the three <5 5 11> FOLZ lines do indeed intersect at the centre of the (000) disc, in agreement with the experimental image (figure 5.2.3b).
The mutual dynamical interaction between the different FOLZ lines is clearly visible in the experimental image. In figure 5.2.3b the short arrow indicates the dynamical splitting at the crossing of the <5̄ 5̄ 11> line with the <1 9 9̄> and <11 7̄ 3̄> lines; the long arrow indicates a dynamical splitting which is caused by the interaction between two <1 9 9̄> lines. In the computed image the mutual dynamical interaction between the two <1 9 9̄> lines is visible (indicated by the long arrow in figure 5.2.3a). The dynamical interaction between the <5 5 11>, <1 9 9̄> and <11 7 3̄> lines (short arrow) is not as apparent as in the experimental image, which may be explained by the fact that the <11 7̄ 3̄> reflections were not included in the calculation.
The bright concentric rings, which are both observed in the experimental image as well in the computed image, are thickness contours (see also the next section). It is apparent that the position of the rings is different in both cases, indicating that the thickness must have been different. A quantative comparison in thickness is not possible, since the thickness was not determined experimentally.

The crystal structure of silicon is described with space group Fd3̄m. When viewed along the <1 1 1> zone axis the arrangement of the Si-atoms exhibits a 3̄m symmetry as shown in figure 5.2.4. It is therefore expected that the diffraction group of the CBED pattern is $6_R mm_R$, resulting in a 3m symmetry in the (000) disc (see table 2.2).
The experimental image (figures 5.2.2 and 5.2.3b) clearly shows the 3m symmetry. The computed image shown in figure 5.2.3a lacks this symmetry. Instead, a 3-fold symmetry is present and only one of the three mirror lines. It is a coincidence that this mirror lies along the diagonal of the rectangular grid from top-left to bottom-right. It is therefore reasonable to suggest that the

figure 5.2.2

Experimental image of the (000) disc of a <1 1 1> ZAP CBED pattern of silicon taken at 102.7 kV. It shows the intersection of the <11 5 5> FOLZ lines at the centre of the disc.
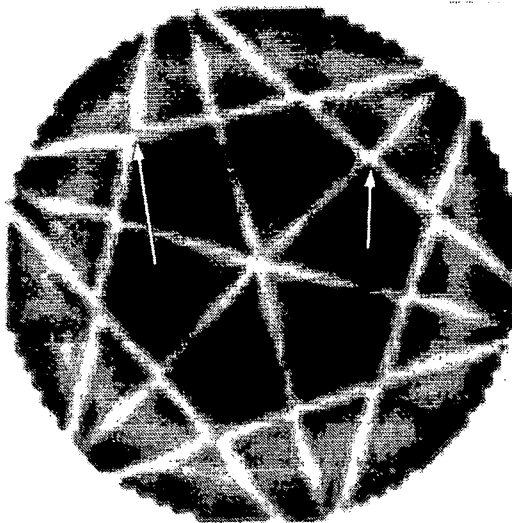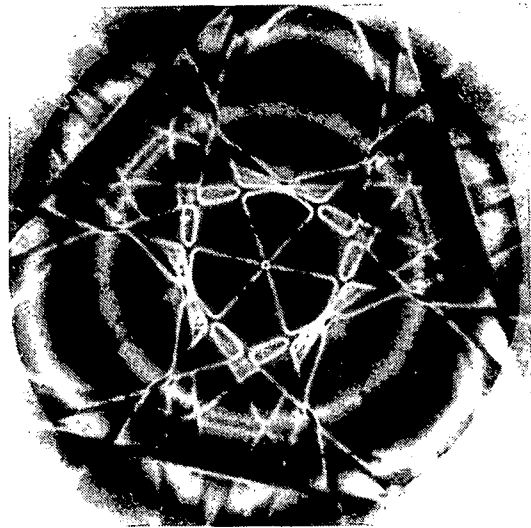
(a)   figure 5.2.3   (b)

Comparison of computed and experimental images. a) Computed image of the (000) disc of a <1 1 1> ZAP of silicon at 102.7 kV. b) Micrograph magnification of part of figure 5.2.2.. The arrows in a) and b) indicate places where dynamical splitting of HOLZ lines can be observed.

figure 5.2.4

The arrangement of Si-atoms viewed along <1 1 1>. The ●, ▲ and ■ indicate pairs of Si-atoms at 0, 1/3 and 2/3 in height along the zone axis. Each symbol is positioned midway between the shortest Si-Si distance. The pattern exhibits a 3m symmetry.

72
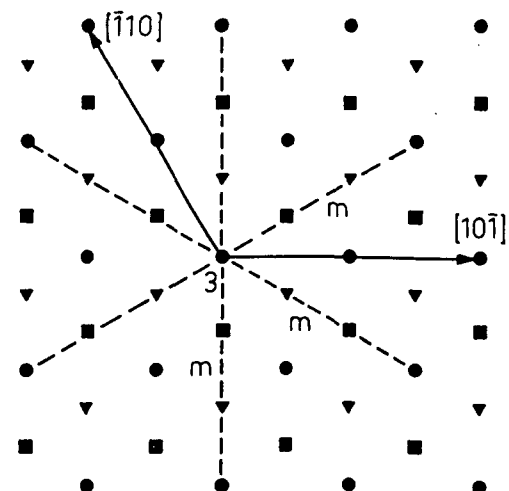
absence of the other two mirror lines results from the rectangular grid construction. In order to verify the presence of the mirror lines, the Rphi grid-type has been used. The result is shown in figure 5.2.5. As explained in section 4.5.2, this image is a different representation of the diffraction disc. In figure 5.2.5 both the 3-fold symmetry as well as the mirror lines are now clearly visible.

figure 5.2.5

Rphi representation of the image presented in figure 5.2.3a. The 3m symmetry is clearly observed.

0°   360°
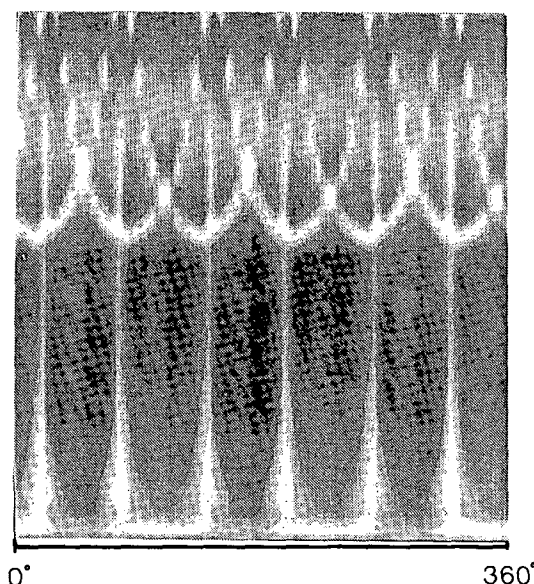
Another aspect of the simulations is the degree to which it approximates the experiment. The agreement between the computed image and the experimental image is influenced by the number of reflections that are taken into account, the specimen thickness and the treatment of absorption. The latter two will be dealt with in the forthcoming sections.

The number of reflections taken into account determines the degree of approximation of the description of the diffraction phenomenon. Figure 5.2.6a shows a computed image of the (000) disc of a silicon <1 1 1> ZAP. The calculation has been based on 88 reflections[+], 51 of which belong to the FOLZ. The angle of convergence is 0.2° and the specimen thickness is 2000 Å. Based on the accelerating voltage of 100 kV the image should be compared with the image shown in figure 5.2.1. Since the angle of convergence is different in both cases (experimental: 0.41±0.02°), a magnified image of the central region of figure 5.2.1 is presented in figure 5.2.6b so that a comparison of the calculated and experimental images can be made.

[+] In the calculation mentioned the (11 $\bar{3}$ 7), ($\bar{1}\bar{1}$ 3 9) and (9 $\bar{1}$ 7) reflections have been left out by mistake. Therefore the number of 88 should have been 91. Since it results in only a minor difference, the image based on the 88 reflections is used for the presentation.
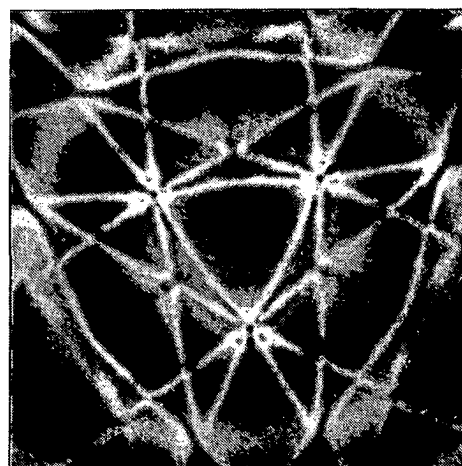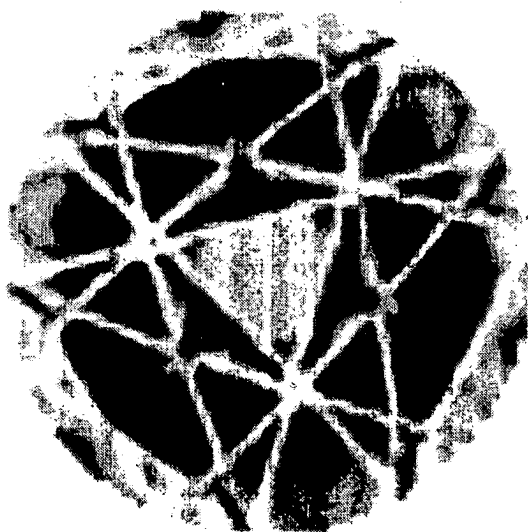
11 $\overline{3}$ $\overline{7}$

(a)   (b)

figure 5.2.6

a) Computed image of the (000) disc of silicon (single
crystal; <1 1 1> ZAP at 100 kV). The calculation is based on
88 reflections. The 3m symmetry is not present because the
(11 $\overline{3}$ $\overline{7}$) reflection is missing as indicated. b) Micrograph
of figure 5.2.1, magnified in order to account for the
difference in angle of convergence. The disagreement of the
position of the thickness contours indicates that the
specimen thickness is different in a) and b).

The images presented in figures 5.2.6a and 5.2.6b are in good
agreement, apart from the difference in position of the thickness
contours, as explained above. Even the fine details of the
experimental image can be observed in the computed image.
The 3m symmetry is absent in the computed image because the (11 $\overline{3}$
 $\overline{7}$) reflection was omitted in the calculation. (see also footnote
on the previous page). Had it been present, the 3m symmetry would
have been complete.
Although the (11 $\overline{3}$ $\overline{7}$) was originally left out by mistake, it
illustrates the fact that those reflections lying on the Ewald
sphere within the angle of convergence, should, at least, be
included into the calculations in order to obtain a satisfactory
agreement with the experimental results. It is known that the
degree of approximation is dependent on the number of Bloch waves
describing the diffraction process, i.e. the number of
reflections taken into account. Therefore, a large number of
reflections, including reflections which do not ly on the Ewald
sphere within the angle of convergence, gives a better
approximation of the diffraction process. On the other hand, the
computation time increases non-linearly with the number of

reflections. It should, therefore, be realized that the aim of
the calculations is to obtain either a good (accurate) agreement
with a long computation time or a satisfactory agreement with an
acceptable computation time. It will be clear that the criterion
for this decision depends on the computer configuration used.

5.2.2 Thickness variations and image contrast.

As has been mentioned in the previous section for the case of
silicon, thickness variations can be determined from the number
of concentric rings within the central disc of the CBED pattern.
Since absorption is assumed to be negligibly small, the total
electron flux will remain constant. The electron intensity
oscillates between the primary beam and the diffracted beams
('Pendellösung') over the 'extinction distance' along the zone
axis (since the extinction distance and the effect of
Pendellösung are actually defined in a two-beam case and here the
concepts are used in a multi-beam case, the concepts of
extinction distance and Pendellösung should be treated with care;
the quotes used here indicate this difference). Therefore, the
image contrast is repeated over the 'extinction distance'.
In the presence of absorption, e.g. in gold, the total electron
flux is attenuated along the depth within the specimen. The image
contrast is not repeated. It is therefore appropriate to have a
closer look at the effect of specimen thickness on the intensity
profile of the CBED patterns. This will be illustrated with the
examples of <1 1 1> ZAP's of gold single crystal specimens. The
absorption is, in each of the specimen models used, equally
treated with an absorption factor V'/V of 0.1. In the next
section, the effect of absorption, in connection with thickness,
is treated in more detail. Figures 5.2.7 a to d show the images
of the (000) disc of the <1 1 1> ZAP CBED pattern of Au specimens
with a thickness of 230 Å, 300 Å, 350 Å and 400 Å respectively.
The change in pattern caused by a thickness difference of 50 Å is
remarkable.
In analogy with the case of <1 1 1> ZAP's of silicon, the
patterns show a 3m symmetry. The crystal srructure of gold is
described with space group Fm$\bar{3}$m. When viewed along the <1 1 1>
zone axis the Au-atoms exhibit a $\bar{3}$m symmetry relationship.
Referring to figure 5.2.4 for the case of silicon, this figure is
also applicable to gold, provided that each symbol is treated as
a Au-atom instead of a pair of Si-atoms. The diffraction group
will therefore be $6_R mm_R$, and according to table 2.2 this gives a
3m symmetry in the (000) disc.
At the time of the calculations no experimental data were
available to verify the calculations. At a later stage,
experimental data was obtained from a gold single crystal
specimen with a thickness of 460 Å±10% . The thickness was
determined using the extinction contour method.
Figure 5.2.7e shows the calculated image of the (000) disc for a
thickness of 460 Å and figure 5.2.8 the experimentally obtained
image. The angle of convergence is, in both cases, identical
within the error (0.4⁰ and 0.40±0.02⁰ respectively).
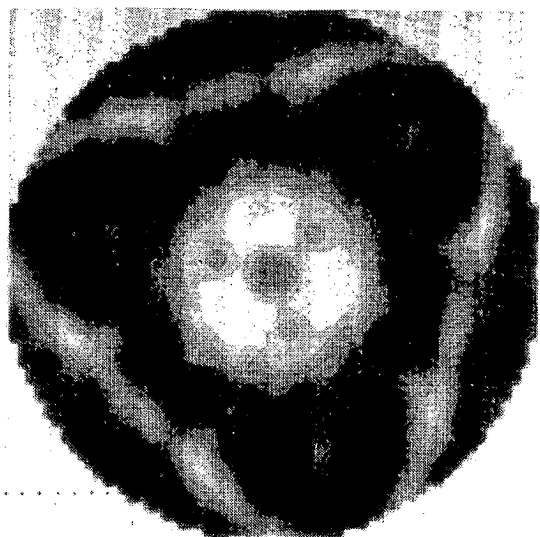
(a)
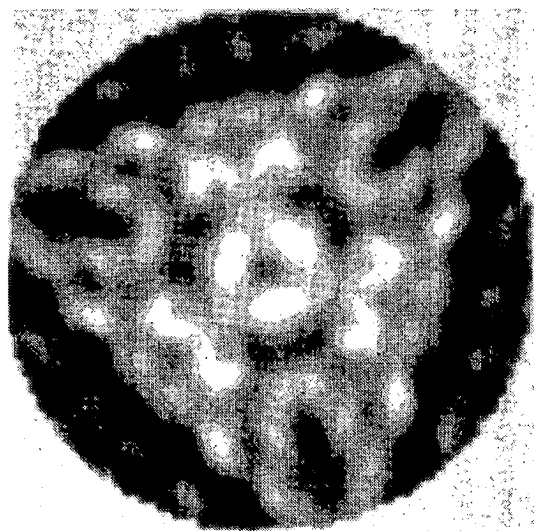
(b)
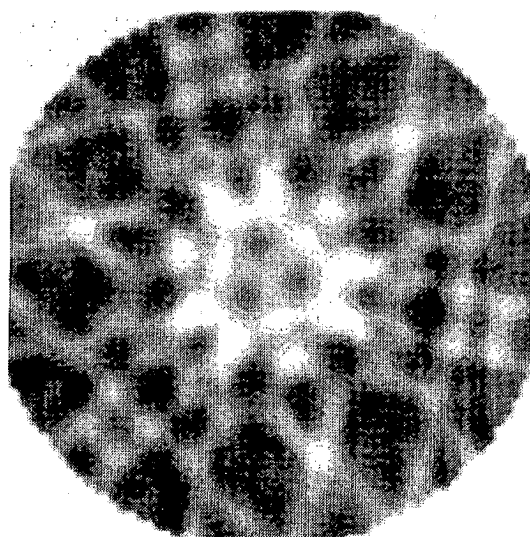
(c)
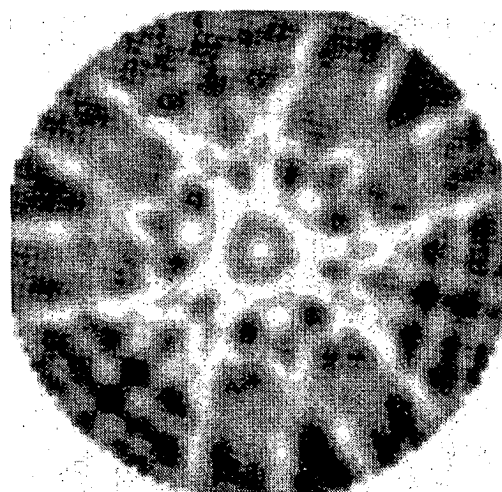
(d)

figure 5.2.7

Computed (000) discs for gold single crystal specimens
having varying thickness. The zone axis is directed along
<1 1 1>. The figures a) to e) show the results for 230 Å,
300 Å, 350 Å, 400 Å and 460 Å respectively. The angle of
convergence is in all cases 0.4°. Absorption is treated with
an absorption factor of 0.1. The symmetry is 3m.

(continued)
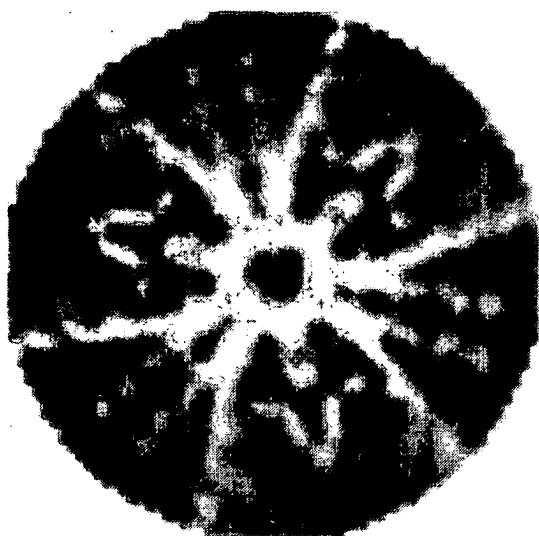
figure 5.2.7e
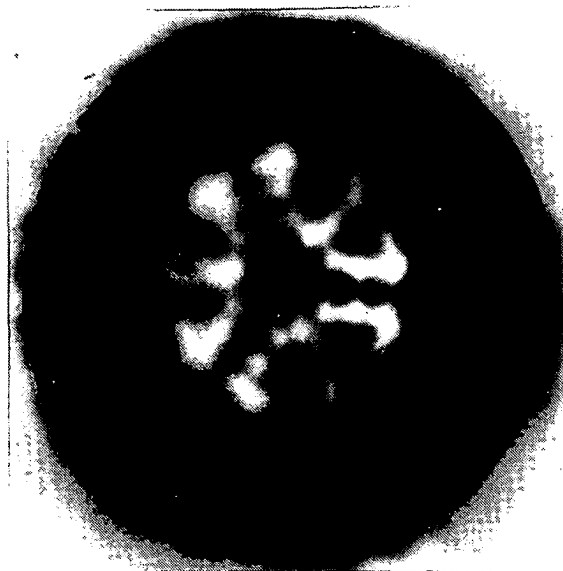
figure 5.2.8

Experimental image of the (000) disc of a gold single crystal specimen having 460 Å±10% thickness. The angle of convergence is 0.40±0.02°. The symmetry is approximately 3m.

It is seen that the experimental image has the characteristics of figure 5.2.7e, but also of figure 5.2.7d. In fact, the agreement is such, that it is difficult to decide which agreement is better. The discrepancy can be explained either by a wrong treatment of absorption in the calculated case, or a deviation from specimen thickness in the experimental case. Gold is considered to be a strongly absorbing material, having an absorption factor of 0.1 [Humphreys & Hirsch 1968, Cowley 1975] (see also the next section). Therefore, it is justified to conclude, based on the visual agreement of the images, that the actual thickness of the specimen in the experimental case must be, within the inaccuracy of the extinction contour thickness measurement, at the lower side of 460 Å. In order to determine the thickness in such a case more accurately, additional calculations within the range of 400 Å to 460 Å should be performed. Since it is not the intention of the present subject to determine the thickness, these calculations are omitted.
The effect of increasing thickness in computed images is extended in figure 5.2.9a (see section 5.2.3) for a thickness of 600 Å. As the absorption factor of 0.1 is used in this case, the image fits into the sequence shown in figure 5.2.7. Again, it is seen that

the pattern has altered considerably.

From the point of view of thickness measurements, it has been shown that the computer program can be used to determine the thickness in a more accurate way than the extinction contour method. On the other hand, the calculation method can lead to laborious efforts if no information on the thickness and absorption factor is available in advance.

5.2.3 The effect of absorption.

The exclusion of absorption from calculations for the case of gold is known to give images which show poor agreement with experimental images [Schapink et al. 1985]. Figures 5.2.9a and 5.2.9b show the difference in computed images which result if absorption is included, or excluded from, the calculation. The images show the (000) disc of a <1 1 1> ZAP of a gold single crystal specimen. They are based on a thickness of 600 Å. The image shown in figure 5.2.9a has been based on a calculation with an absorption factor (i.e. V'/V) of 0.1. It is seen that the introduction of the effect of absorption changes the pattern drastically.

In the previous section, in which thickness variations in gold single crystal specimens were considered, absorption was taken
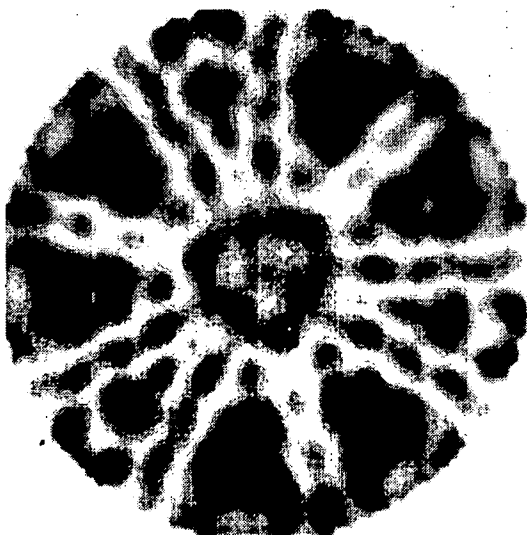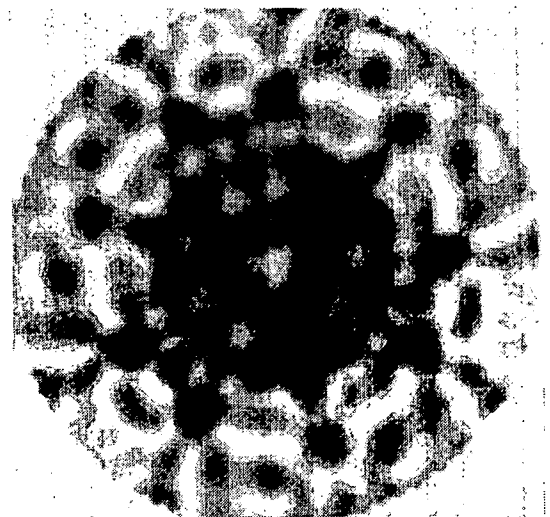
(a)   (b)

figure 5.2.9

Computed (000) disc of a gold single crystal specimen (thickness 600 Å). a) Absorption is included with an absorption factor of 0.1. b) Absorption is excluded.

into account with an absorption factor of 0.1. The effect of altering the absorption factor from a value of 0.05 to 0.1 is illustrated in figure 5.2.10a and 5.2.10b. The thickness was in both cases 460 Å (figure 5.2.10b is identical to figure 5.2.7e). The images of figures 5.2.10a and b show a remarkable similarity. The difference in absorption factor does not seem to change the pattern drastically in the range from 0.05 to 0.1.

An explanation for the described behaviour is difficult to establish, because of its complexity. In analogy to Beer's law,

$$I_g = I_g^{el} \exp(-4\pi q.z) \qquad\qquad 5.2.1$$

keeping the product of absorption factor and thickness constant (i.e. q.z=C), it should result in the same intensity. Comparing figures 5.2.7a and 5.2.10a, it is obvious that it is not the case. An explanation is found by the fact that the intensity, as a result of elastic scattering only, is thickness dependent (c.f. eqs. 4.2.32 and 4.2.33), i.e. Beer's law is not applicable. In addition, it must be realized, that the intensities are scaled to a certain greyvalue, using

$$greyvalue = (\log(I) - \log(I_{min}))/(\log(I_{max}) - \log(I_{min})) \times n$$

$$\cdots 5.2.2$$

in which n is the number of greyvalues within the grey-scale. Introducing the mean absorption, q^0, identical for each Bloch wave and diffraction direction, it is easily seen that the mean

(a)   (b)
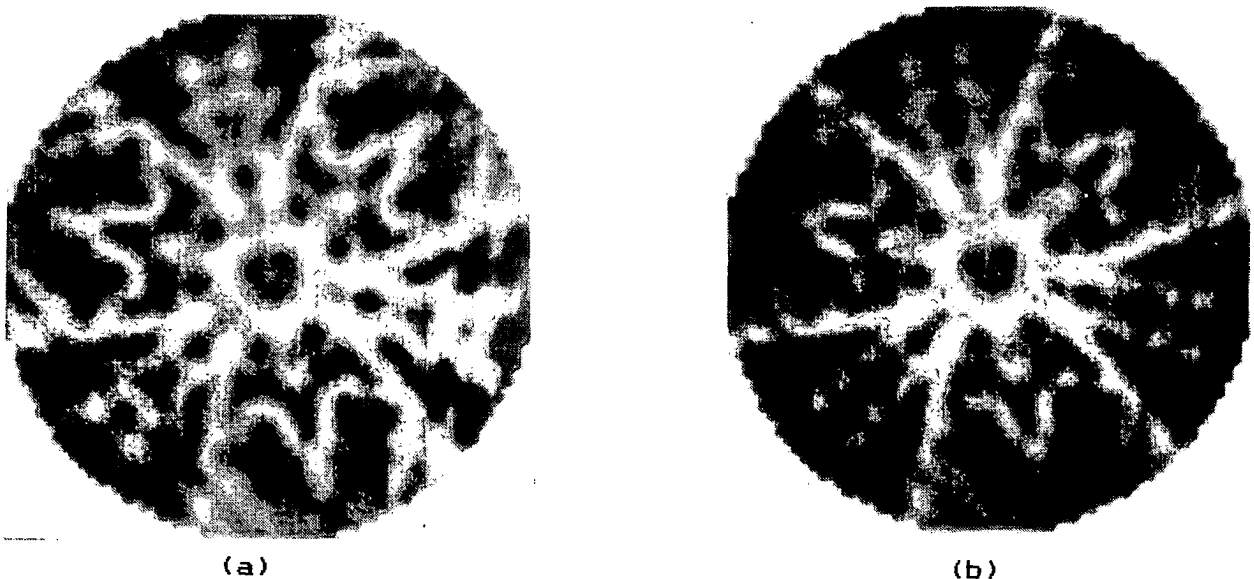
figure 5.2.10

Computed image of the (000) disc of a gold single crystal specimen (thickness 460 Å). Absorption is treated with an absorption factor of 0.05 (a) and 0.1 (b) respectively.

absorption disappears using eq. 5.2.2, i.e. the same image is obtained. Experimentally, this is equivalent to an increment of the exposure time.

On the other hand, the absorption factor, q, is in fact different for each Bloch wave and diffraction direction (c.f. eq. 4.2.42), making it impossible to obtain a simple relation, comparible to Beer's law. The observation that figures 5.2.10a and b show such a similarity, suggests that, in this particular case of thickness and range of absorption, absorption may be treated using a mean absorption.

A different aspect of the effect of absorption is the observation that it may destroy the pattern symmetry which is observed by virtue of the reciprocity relation. This will be illustrated with two examples, the first involving a single crystal of GaAs and the second involving a bicrystal of Au.

The crystal structure of gallium-arsenide (GaAs) is described with space group $F\bar{4}3m$. When viewed along the $<1 \bar{1} 0>$ zone axis there are two mirror planes: one parallel and the other perpendicular to the zone axis. The expected diffraction group is therefore $m1_R$, giving a 2mm symmetry in the (000) disc of the CBED pattern (c.f. table 2.2). In figure 5.2.11 the symmetry of this disc is shown using the radial-scan method for a thickness of 400 $\overset{o}{A}$. Clearly the 2mm symmetry is present in the case of figure 5.2.11a in which absorption has been excluded from the calculations. In figure 5.2.11b absorption has been included with an absorption factor of 0.05. The 2mm symmetry is reduced to m. On the other hand, the deviation from 2mm symmetry is not pronounced. Although the 2-fold symmetry is destroyed, the values near the original mirror lines (indicated by the dotted line) almost show a mirror symmetry. At a higher thickness of 800 $\overset{o}{A}$ (figure 5.2.11c), the same behaviour is observed, i.e. the deviation from 2mm symmetry is not pronounced. Therefore, it is expected that, experimentally, not a m-symmetry, but rather a 2mm symmetry is observed, i.e. the effect of absorption on the symmetry of the pattern is difficult to observe, the more so if we consider that GaAs is a low absorbing material. Figure 5.2.11d shows an experimental image of the (000) disc of a $<1 \bar{1} 0>$ ZAP of GaAs at 100 kV. It is seen that in this case the symmetry is 2mm. For the second example a bicrystal specimen of gold is used. The interface is of the type $\Sigma=7^+$, which means that crystal I and crystal II are related by $\{38.22^o|0\}I=II$, if I and II denote the respective crystal parts. The bicrystal space group is R32'. In a $<1 1 1>$ zone axis orientation three 2' axes are perpendicular to the zone axis. In order to fulfil the condition that the 2' axes can be detected by virtue of the reciprocity relation, the interface is positioned at 0.5 of the total specimen thickness of 850 $\overset{o}{A}$, i.e. the specimen exhibits the 2' symmetry operation; it is not a crystallographic symmetry operation like the mirror in the case of GaAs. With the interface positioned at 0.5, the

---

[+] The characteristics of a $\Sigma=7$ type CSL are explained in more detail in section 5.2.6.

INTENSITIES OF DISK   0   0   0
ORIENTATION :   0.00 DEGREES

0.9556E-01	0.4406E+00	0.2033E+00
0.2053E+00	0.4712E+00	0.2642E+00
0.2485E+00	0.4834E+00	0.2954E+00 ——— m
0.2053E+00	0.4712E+00	0.2642E+00
0.9556E-01	0.4406E+00	0.2033E+00
-.3393E-01	0.4061E+00	0.1660E+00
-.2343E+00	0.3813E+00	0.2003E+00
-.3517E+00	0.3773E+00	0.2661E+00
-.3708E+00	0.3604E+00	0.2822E+00 ——— m
-.3518E+00	0.3773E+00	0.2661E+00
-.2343E+00	0.3813E+00	0.2003E+00
-.3393E-01	0.4061E+00	0.1660E+00
0.9555E-01	0.4406E+00	0.2033E+00
0.2053E+00	0.4712E+00	0.2642E+00
0.2485E+00	0.4834E+00	0.2954E+00 ——— m
0.2053E+00	0.4712E+00	0.2642E+00
0.9557E-01	0.4406E+00	0.2033E+00
-.3392E-01	0.4061E+00	0.1660E+00
-.2343E+00	0.3813E+00	0.2003E+00
-.3517E+00	0.3773E+00	0.2661E+00
-.3708E+00	0.3804E+00	0.2822E+00 ——— m
-.3517E+00	0.3773E+00	0.2661E+00
-.2343E+00	0.3813E+00	0.2003E+00
-.3393E-01	0.4061E+00	0.1660E+00

(a)

INTENSITIES OF DISK   0   0   0
ORIENTATION :   0.00 DEGREES

0.1920E+00	0.2744E+00	0.1122E+00
0.2756E+00	0.3043E+00	0.1686E+00
0.3249E+00	0.2808E+00	0.1844E+00 ——— m
0.2756E+00	0.3043E+00	0.1666E+00
0.1920E+00	0.2744E+00	0.1122E+00
0.4835E-01	0.2704E+00	0.7544E-01
-.7164E-01	0.2380E+00	0.6179E-01
-.1574E+00	0.2347E+00	0.7985E-01
-.2062E+00	0.2347E+00	0.9762E-01 - - - -
-.1582E+00	0.2347E+00	0.8014E-01
-.1721E-01	0.2402E+00	0.6278E-01
0.4237E-01	0.2652E+00	0.7213E-01
0.1964E+00	0.2743E+00	0.1138E+00
0.2788E+00	0.3017E+00	0.1683E+00
0.3156E+00	0.2772E+00	0.1764E+00 ——— m
0.2788E+00	0.3017E+00	0.1683E+00
0.1964E+00	0.2743E+00	0.1138E+00
0.4234E-01	0.2653E+00	0.7216E-01
-.712CE-01	0.2402E+00	0.6278E-01
-.1582E+00	0.2347E+00	0.8014E-01
-.2054E+00	0.2258E+00	0.9315E-01 - - - -
-.1574E+00	0.2347E+00	0.7984E-01
-.7164E-01	0.2380E+00	0.6179E-01
0.4640E-01	0.2703E+00	0.7542E-01

(b)

INTENSITIES OF DISK   0   0   0
ORIENTATION :   0.00 DEGREES

0.5166E-01	-.1142E-01	0.2799E-02
0.1775E+00	0.1626E+00	0.5794E-01
0.2666E+00	0.1937E+00	0.1086E+00 ——— m
0.1775E+00	0.1626E+00	0.5793E-01
0.5165E-01	-.1143E-01	0.2799E-02
-.1555E+00	-.1493E+00	0.4647E-01
-.3153E+00	-.1691E+00	0.1280E+00
-.3702E+00	-.1478E+00	0.1589E+00
-.3570E+00	-.1564E+00	0.1519E+00 - - - -
-.3660E+00	-.1472E+00	0.1556E+00
-.3169E+00	-.1647E+00	0.1275E+00
-.1388E+00	-.1641E+00	0.4621E-01
0.5371E-01	-.1021E-01	0.2989E-02
0.1845E+00	0.1622E+00	0.6034E-01
0.2509E+00	0.1843E+00	0.9689E-01 ——— m
0.1845E+00	0.1622E+00	0.6035E-01
0.5373E-01	-.1020E-01	0.2991E-02
-.1388E+00	-.1642E+00	0.4624E-01
-.3169E+00	-.1647E+00	0.1275E+00
-.3660E+00	-.1472E+00	0.1556E+00
-.3696E+00	-.1515E+00	0.1595E+00 - - - -
-.3702E+00	-.1478E+00	0.1589E+00
-.3153E+00	-.1691E+00	0.1280E+00
-.1555E+00	-.1493E+00	0.4645E-01

(c)
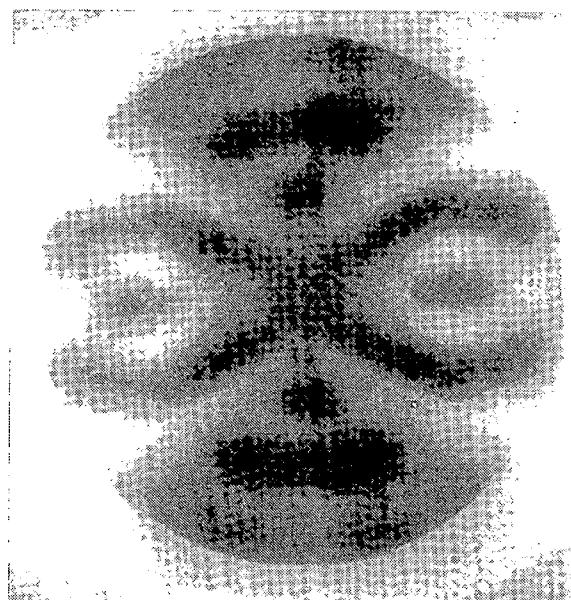
(d)

figure 5.2.11

a) Radial scan of the (000) disc of a GaAs <1 Ī 0> ZAP, for a thickness of 400 Å, absorption excluded; the symmetry is 2mm. b) As in figure 5.2.11a, absorption included with a factor of 0.05; the symmetry is m. The mirror lines are indicated. c) As in figure 5.2.11b for a thickness of 800 Å d) Experimental image of the (000) disc of a GaAs <1 Ī 0> ZAP at 100 kV. The pattern shows symmetry 2mm.

diffraction group is expected to be $3m_R$, giving a $3m$ symmetry in the (000) disc (c.f. table 2.2).

Figure 5.2.12 shows the computed images of the (000) disc of <1 1 1> ZAP CBED patterns for the case where absorption is treated with an absorption factor of 0.1 (figure 5.2.12a) and for the case where absorption is excluded (figure 5.2.12b). It is seen that the pattern in figure 5.2.12a has a 3-fold symmetry whereas the pattern in figure 5.2.12b has a $3m$ symmetry.

In the above two cases it has been shown that, caused by the effect of absorption, the symmetry relations which are expected to be seen in the CBED pattern, by the reciprocity relation, may not be observed. In the case of gold, the effect is such, that the reciprocity relation can no longer be applied. In the case of gallium-arsenide, the effect is less pronounced: the application of the reciprocity relation is still valid.
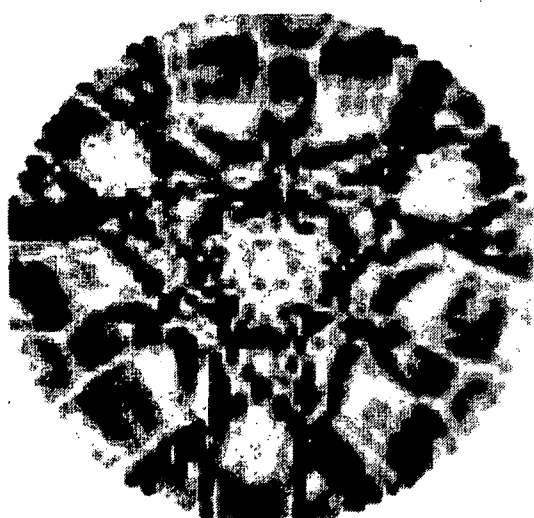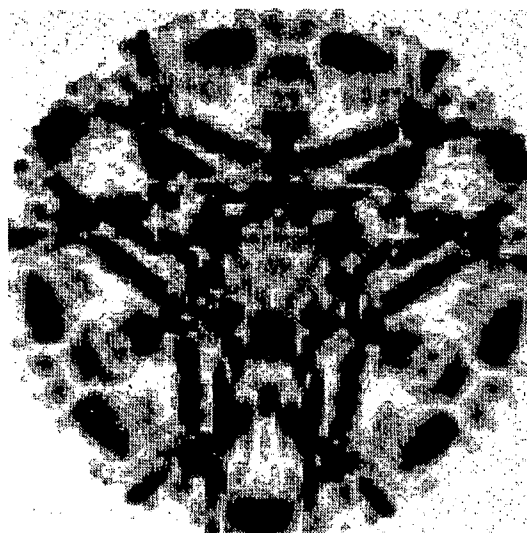
(a)   (b)

figure 5.2.12

Computed image of the (000) disc for a gold bicrystal specimen (<1 1 1> ZAP) with a $\Sigma=7$ type boundary. a) Absorption is included (V'/V=0.1), giving a 3-fold symmetry . b) Without absorption, it results in a $3m$ symmetry.

5.2.4 The position of a twin boundary in a bicrystal specimen.

As has been pointed out by Schapink et al. [1983] and Buxton et al. [1984], horizontal bicrystal colour symmetry elements are observed in the CBED pattern if the boundary coincides with the midplane of the specimen (see also chapter 3). If the boundary lies asymmetrically, the bicrystal specimen no longer exhibits the coloured (horizontal) symmetry operations. We have investigated the influence of the position of the boundary on the existence of symmetry relations in the CBED pattern originating from horizontal coloured symmetry elements, using the example of a silicon bicrystal having a <1 1 1> twin boundary.

A <1 1 1> twin boundary is constructed by rotating the second crystal 60° along <1 1 1> (a righthanded or lefthanded rotation is unimportant in this case) relative to the first crystal. In terms of the Seitz operator we therefore have the relation {60°|0}I=II, if I and II denote the respective crystal parts. The unit cell of the lattice which is continous over the interface (CSL) is three times as large as the unit cell of either constituent crystal, i.e. $\Sigma=3$. The space group G_{dcp} of the dichromatic pattern, as shown in figure 5.2.13, is P6'/m'm'm.

The symmetry elements which are observed in a CBED pattern with the incident beam directed along <1 1 1>, will be a vertical 3-fold axis, three vertical mirror planes and a horizontal coloured mirror plane. The latter will be observed as a 2-fold symmetry in the (000) disc of the pattern, provided that the horizontal m' operation is in the midplane of the specimen. Defining the position of the boundary in terms of the total specimen thickness, diffraction group expected is $3m1_R$ in case the boundary is positioned at 0.5; for all other values than 0.5, i.e. when the interface is not coincident with the midplane, the diffraction group will, in theory, be 3m. Referring to table 2.2, diffraction group $3m1_R$ shows a whole pattern symmetry of 3m and a 6mm symmetry for the central disc; diffraction group 3m shows a 3m symmetry for the whole pattern, the central disc having simply 3m symmetry.

Experimentally, the following specimen was investigated (figure 5.2.14a). The specimen has faces which were determined to be {112}; the interface is a <1 1 1> twin boundary (i.e. $\Sigma=3$). Taking a <1 1 1> ZAP, therefore, results in an actual asymmetrical Laue case. Although an inclination of 19.5° is present, the entrance and exit faces of the specimen are assumed to be parallel to the boundary plane within the spot of the focussed electron beam (see also figure 3.1.2). The asymmetrical Laue case is hereby treated as symmetrical. From this known geometry, the thickness of the specimen could be determined to be 2000 Å±10%.

The micrographs shown in figures 5.2.14b and 5.2.14c show the (000) disc of the specimen in question, at 100 kV. They have been taken at different positions along the interface as illustrated in figure 5.2.14a. In figure 5.2.14b the symmetry of the pattern is not distinguishable from 6mm symmetry. A slight shift of the incident beam along the plane of the interface gives the pattern of the (000) disc shown in figure 5.2.14c. Here, the symmetry of

figure 5.2.13

Dichromatic pattern of a Σ=3 type CSL for silicon. The space group is P6'/m'm'm. The open and closed symbols indicate the 'colour' difference. The symbols indicate pairs of Si-atoms (c.f. figure 5.2.4)
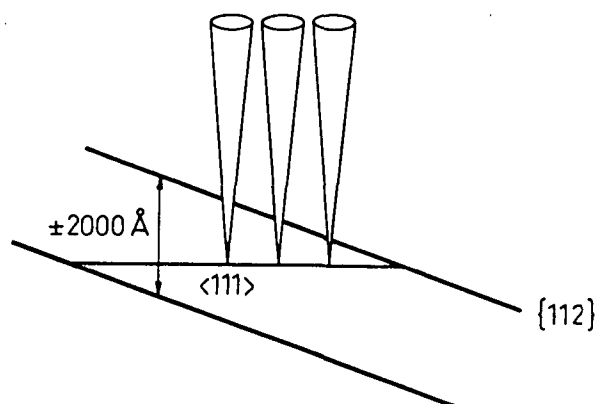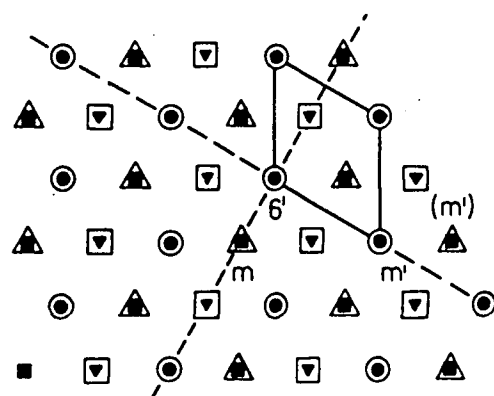
(a)
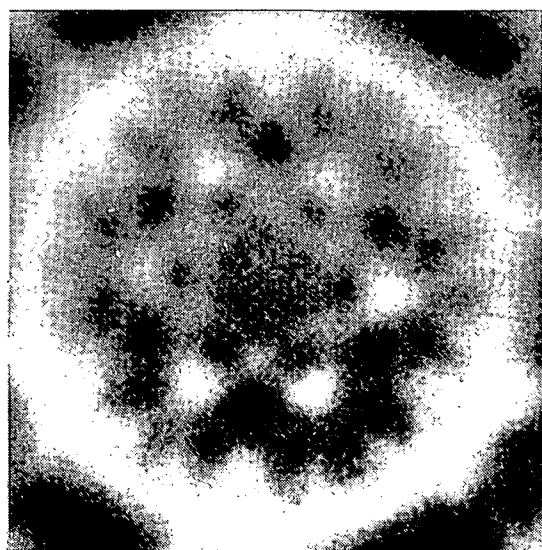
(b)
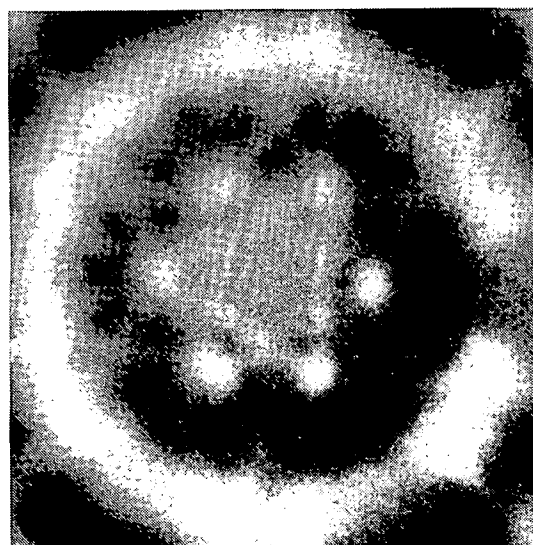
(c)

figure 5.2.14

a) Specimen configuration illustrating how the CBED patterns at different depths of the boundary have been obtained. b) Experimental image of the (000) disc of silicon (bicrystal, Σ=3). The position of the boundary is near 0.5. The symmetry is indistinguishable from 6mm. c) As in b) with the position of the boundary away from 0.5. The symmetry observed is 3m.

the pattern is clearly 3m. Considering figures 5.2.14b and
5.2.14c, it is apparent that these observations are according to
what has been expected. However, because the exact locations of
the beam, with respect to the boundary, are not known, the
observations do not give information on the relation between
symmetry and the position of the boundary.
In order to establish the minimum deviation of the boundary
position from the midplane of the specimen, needed to cause a
detectable change in symmetry, calculations have been performed
for the boundary position at 0.5, 0.48 and 0.46. The total
specimen thickness has been set at 2000 Å, the accelerating
voltage at 100 kV. The calculations are based on 31 reflections,
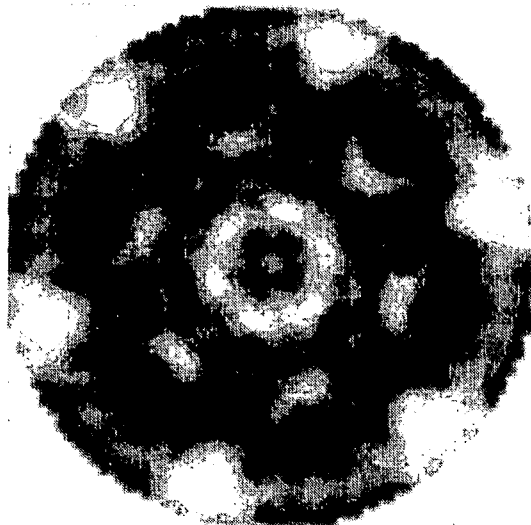
(a)
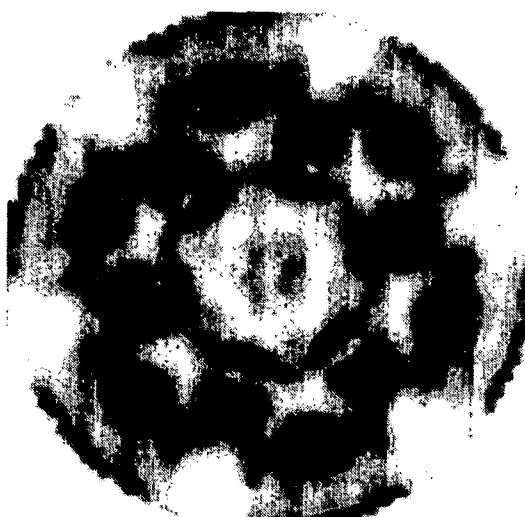
(b)

(c)

figure 5.2.15

Computed (000) disc of silicon (bicrystal, Σ=3). A change in
symmetry results form a difference in positions of the
boundary. Figures a to c show the result for boundary
positions of 0.5, 0.48 and 0.46 respectively. The observed
symmetry is reduced from 6mm to 3m.

of which 18 belong to the FOLZ. The results are shown in figures 5.2.15a, 5.2.15b and 5.2.15c respectively. Figure 5.2.15a clearly shows the 6mm symmetry as expected.

On changing the position of the boundary from 0.5 to 0.46 it is seen that the symmetry changes from 6mm to 3m. At 0.48 the deviation from 6mm symmetry is hardly detectable. At 0.46 a 3m symmetry is observed rather than a 6mm symmetry. Therefore, there is only a small range of 4% of the total thickness at either side of the midplane position where the effect of horizontal colour symmetry elements is observed, at least when using an imaging system based on 16 greylevels; a better greylevel resolution can give even a smaller range in which the effect of horizontal symmetry elements might be observed. Referring to figure 5.2.14b, we can, therefore, conclude that this micrograph is obtained from an area where the position of the boundary is approximately 0.5.

Another example involves a bicrystal of gold with a $\Sigma=3$ $\langle 1\ 1\ 1 \rangle$ twin boundary. It is the same type of bicrystal as described above, except that silicon has the diamond structure (space group $Fd\overline{3}m$) whereas gold has a cubic face centered structure (space group $Fm\overline{3}m$). The space group of the dichromatic pattern G_{dcp} is $P6'/m'm'm$. A CBED pattern taken along the $\langle 1\ 1\ 1 \rangle$ zone axis should, therefore, give either diffraction group $3m1_R$ or diffraction group $3m$, depending on the position of the boundary.

Figure 5.2.16a shows the experimental CBED image of the central disc of the specimen described. In the image, a symmetry indistinguishable from 6mm, is observed. The position of the boundary should therefore be near to 0.5.

Figure 5.2.16b shows the simulated image based on a total thickness of 800 $\overset{\circ}{A}$. The boundary position has been taken at 0.5, and absorption has been included into the calculation with an absorption factor of 0.1. The calculation is based on 55 reflections of which 42 belong to the FOLZ. Again a good agreement between the experimental image and calculated image is obtained.

It has only been the intention to compare the symmetry in the experimental and computed image. The fact that the images show, in addition, such a good agreement in intensity profile, is due to the choice of thickness of 800 $\overset{\circ}{A}$. Since no experimental information on specimen thickness could be retrieved in this case, this choice must be considered to be merely fortuitous, the more so if we consider the fact that the pattern is very sensitive to thickness variations (see also section 5.2.2).

Referring to section 5.2.3, where the effect of absorption on the symmetry of the pattern has been treated, figure 5.2.16b also illustrates the reduction in symmetry due to the effect of absorption. Theoretically, diffraction group $3m1_R$ is expected if the interface is positioned at 0.5, giving a 6mm symmetry in the (000) disc. Figure 5.2.16b lacks this symmetry if certain image details are considered; in fact only a 3m symmetry is observed. For instance, the arrow indicates a certain detail in the image which is not repeated by 6-fold symmetry. The deviation from 6mm symmetry in the experimental image of figure 5.2.16a is not apparent, which may be caused by the poor quality of the micrograph.
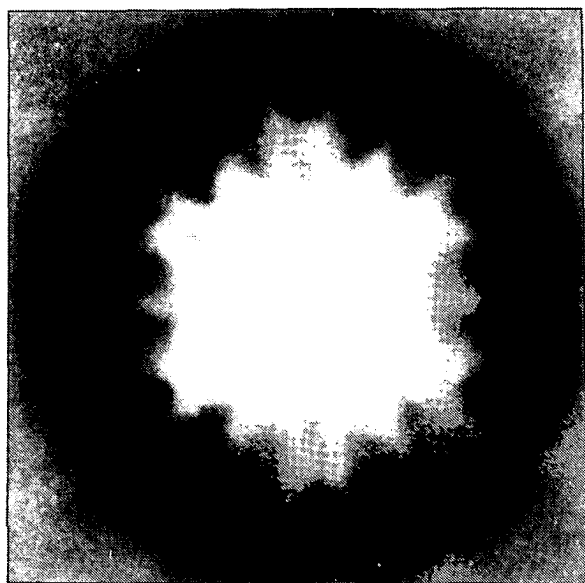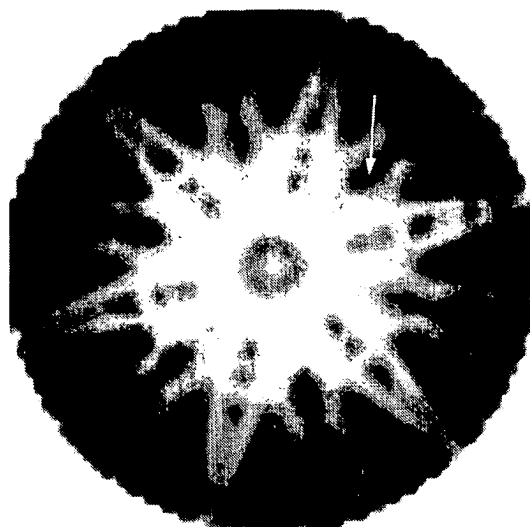
(a)   (b)

figure 5.2.16

a) Experimental image of the (000) disc of gold (bicrystal,
Σ=3, <1 1 1> ZAP). The symmetry observed is indistinguish-
able from 6mm. b) Computed image equivalent to a. The angle
of convergence is 0.37±0.02° and 0.4° respectively.

5.2.5 The effect on the symmetry of CBED patterns of a translation at the boundary of bicrystal specimens.

Up to this point only bicrystals have been considered which had a
simple rotational relationship between the constituent crystals I
and II. In this section bicrystals are considered which are, in
addition, translated with respect to each other (c.f. eq. 3.1.1).
As has been explained in section 3.2 and 3.3, each state of
translation is related to a certain space group of the
dichromatic pattern G_{dcp}. In addition, each space group is
related to a diffraction group of the CBED pattern. The relation
between the DG and the translation is, in general, not unique for
each DG, since different translations can lead to the same DG. On
the other hand, in specific cases, DG's can uniquely be related
to the translation. In such cases, the translation can be
determined from the symmetry of the CBED pattern.
The complete set of G_{dcp}'s and, therefore, the complete set of
DG's, relating all the possible translations, can be constructed
by considering only those translations which lie within the
Wigner-Seitz cell of the DSC lattice. Schapink and Mertens [1981]

have illustrated, using the case of a Σ=3 type boundary, that
certain states of translation give specific diffraction groups of
a <1 1 1> ZAP CBED pattern, which are different from the state of
zero translation. Figure 5.2.17 shows the DCP of the state of
zero translation and the Wigner-Seitz cell of the DSC. The unit
cell of the DSC is bounded by 1/6[Ī Ī 2] and 1/6[Ī 2 Ī],
expressed in terms of the crystallographic coordinate system of
crystal I.

The work of Schapink and Mertens is illustrated here with two
calculated examples of bicrystal specimens with a Σ=3 type
boundary. Although the examples refer to translations which are
not likely to be met experimentally, they illustrate the change
in symmetry resulting from such a translation. A comparison with
reality can, therfore, not be made. For convenience, the position
of the boundary is taken at 0.5 in which case horizontal coloured
symmetry elements, if present, apply to the bicrystal specimen
and can therefore be observed.

The first example (figure 5.2.18a) involves a silicon bicrystal
specimen having a Σ=3 type boundary. The relation existing
between crystal I and crystal II is {60°|1/12<Ī2Ī>} along
<1 1 1>. As a result the space group of the DCP is determined to
be Cmc'a' (see figure 5.2.18b); for comparison the space group of
the zero translation state is P6'/m'm'm (see also section 5.2.2
and Table I of Schapink & Mertens [1981]).

The diffraction group of the CBED pattern taken along <1 1 1> is
expected to be $m1_R$, the 1_R operation resulting from the a' glide
plane. According to table 2.2 the central disc must show a 2mm
symmetry.
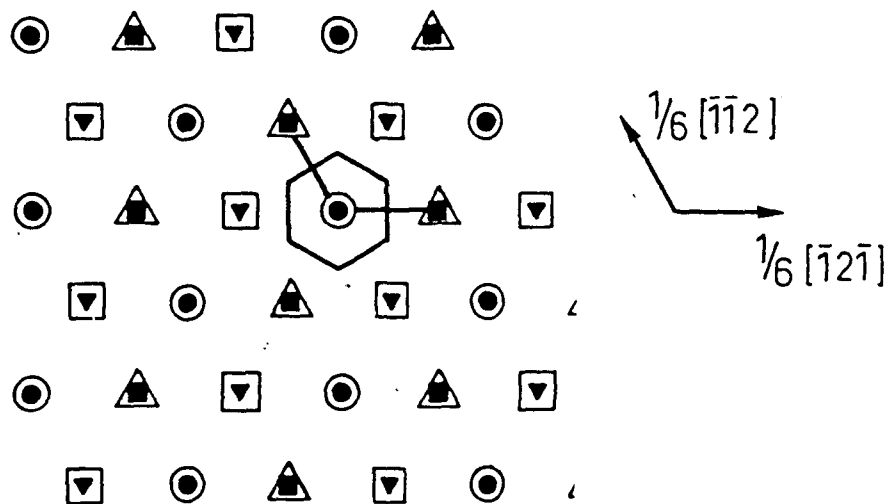
figure 5.2.17

The dichromatic pattern (DCP) seen along <1 1 1> for the
state of zero translation in case of a Σ=3 type boundary.
The symbols indicate atom positions in the case of Au and
pairs of atoms in the case of Si. The Wigner-Seitz cell of
the DSC-lattice is included.

The calculation has been performed using a specimen thickness of 2000 Å, the accelerating voltage was set at 100 kV. The number of reflections taken into account is 31, of which 18 belong to the FOLZ. In figure 5.2.18a the 2mm symmetry is clearly observed, confirming Schapink & Mertens' result.

The second example (figure 5.2.19a) involves the same type of specimen as presented in the first example, apart from the fact that the translation at the boundary has been adjusted to $1/6 \langle 0\ 1\ \bar{1} \rangle$, i.e. the relation that exists between the constituent crystal parts is $\{60° | 1/6 \langle 0\ 1\ \bar{1} \rangle \}$ along $\langle 1\ 1\ 1 \rangle$. The space group of the DCP is determined to be $P3_1 12'$[+] (see figure 5.2.19b) and therefore the diffraction group of the $\langle 1\ 1\ 1 \rangle$ zone axis CBED pattern is expected to be $3m_R$, since in the $\langle 1\ 1\ 1 \rangle$ zone axis orientation the 2' axis is perpendicular to the zone axis giving a m_R operation in the diffraction group. According to table 2.2 the central disc should therefore show a 3m symmetry. The calculation parameters have been set equivalent to the previous example. In figure 5.2.19a the 3m symmetry is clearly observed.

In the present example a 3-fold screw axis is directed along the zone axis. The effect of this translational-coupled symmetry element is not observed in figure 5.2.19a and is, therefore, considered to be too small to contribute to the pattern formation. This is in agreement with the work of Goodman [1975], Buxton et al. [1976] and Ishizuka [1984].

Comparing figures 5.2.18a and 5.2.19a, it is seen that, apart from the difference in symmetry, the images show a close correspondence. Compared with the image involving the zero state of translation, (figure 5.2.15a) the correspondence is also apparent. In practice this will mean that the determination of the state of translation at the boundary, based on a simple comparison of the experimental and calculated patterns only, is questionable, and can lead to erroneous results. The determination of the state of translation at the boundary is valid only when the images are of good quality and clearly show the symmetry of the pattern.

[+] This particular translation at the boundary is not included in Table I of Schapink & Mertens [1981]. For completeness it should, therefore, be added.

(a)

(b)
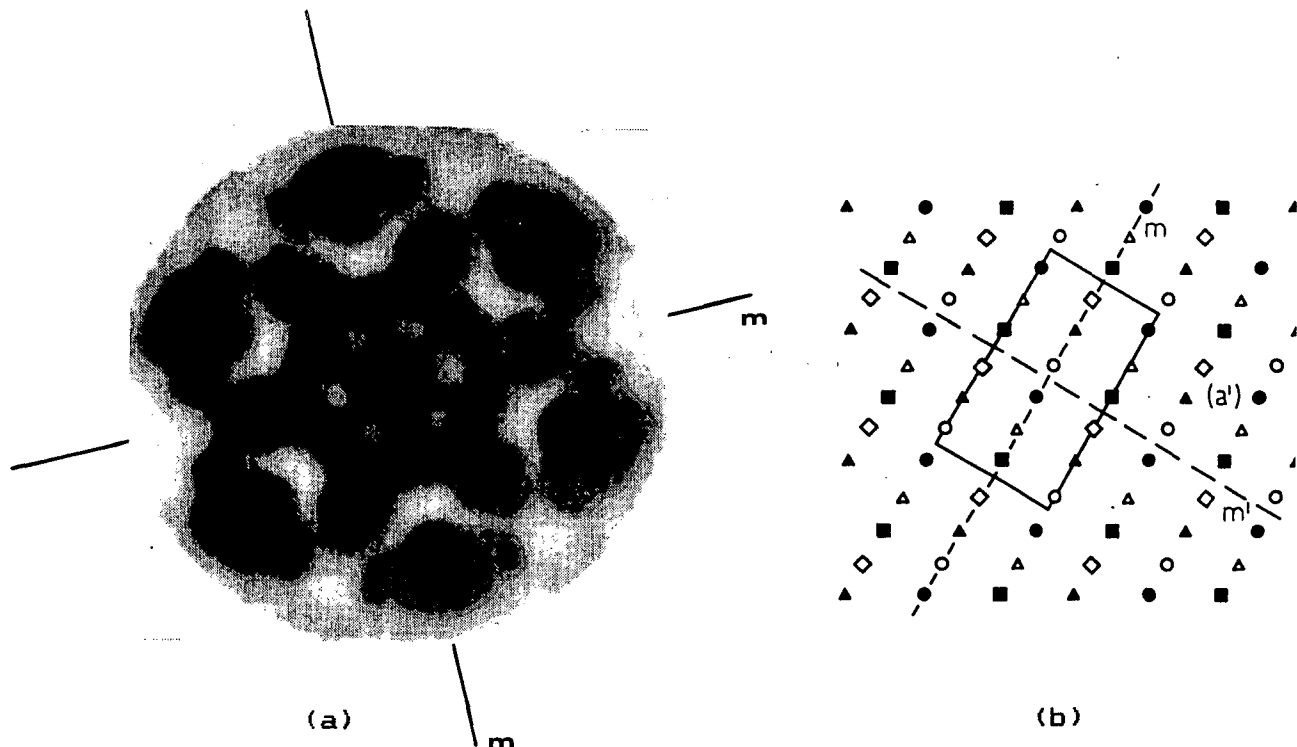
figure 5.2.18

a) Computed image of the (000) disc of a silicon bicrystal
(Σ=3). The boundary is positioned at 0.5. A translation of
1/12[Ī 2 Ī] is included. The symmetry is 2mm. b) The
dichromatic pattern belonging to a; the symbols indicating
pairs of Si-atoms (c.f. figure 5.2.4).

(a)

(b)
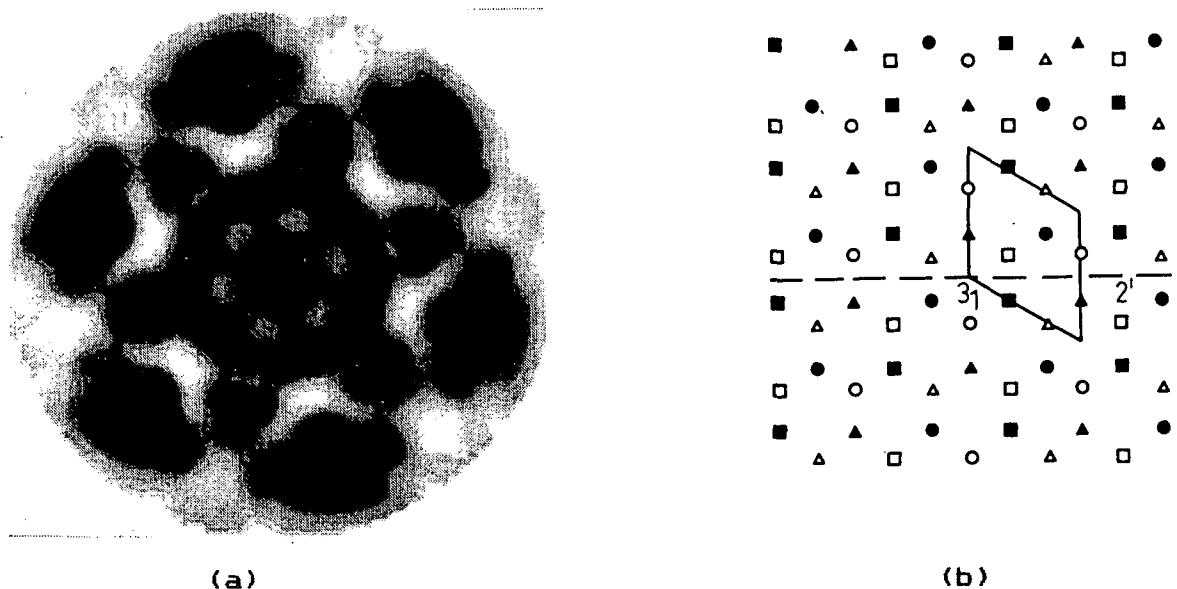
figure 5.2.19

a) Computed image of the (000) disc of a silicon bicrystal
(Σ=3). The boundary is positioned at 0.5. A translation of
1/6[0 1 Ī] is included. The symmetry is 3m. b) The
dichromatic pattern belonging to a; the symbols indicate
pairs of Si-atoms (c.f. figure 5.2.4).

5.2.6 A Σ=7 twist type boundary in a bicrystal of gold; a case of multiple diffraction.

Figure 5.2.20a shows a CBED pattern of a gold bicrystal specimen having a Σ=7 type boundary. The micrograph is taken at an accelerating voltage of 100 kV. The angle of convergence is 0.47±0.02º.

A Σ=7 twist type boundary can be constructed using the relation {38.22º|0}I=II, giving the disc pattern shown in figure 5.2.20c. Only a part of the ZOLZ reflections, and that part of the FOLZ reflections near the intersection of the Ewald sphere, are shown; the large circle indicates where the Ewald sphere belonging to 100 kV intersects the FOLZ plane. It is seen that most of the CBED discs partially overlap. Complete overlap is, besides the (000) disc, found for 6 FOLZ reflections, i.e. they are common to both crystal I and II. The orientation of figure 5.2.20c is such that it is compatible to figure 5.2.20a.

The dichromatic pattern has space group R$\bar{3}$m' resulting in diffraction group $3m_R$ for the <1 1 1> ZAP, provided that the interface is coincident with the midplane of the specimen so that the horizontal 2' symmetry axis is detected. Diffraction group $3m_R$ gives a 3-fold symmetry for the whole pattern and a 3m symmetry for the (000) disc. On the other hand, it is known that when absorption is included, as is the case with the gold specimen, the reciprocity relation may not be applicable, i.e. the 3m symmetry within the (000) disc is reduced to 3-fold symmetry, despite the fact that the position of the interface, which is unknown in the present case, is at 0.5. Both figures 5.2.20a and 5.2.20b show a 3-fold symmetry.

A peculiar observation in the CBED pattern of figure 5.2.20a is the reflection which is indicated by the arrow (by symmetry it is repeated every 120º). It is shown at greater magnification in figure 5.2.20d. From the Ewald sphere construction we expect the line profile of a FOLZ disc to be concentric with the origin in the pattern. Clearly it is observed that the reflection in question is concentric with a different origin. Another feature is that this reflection cannot be indexed in terms of the FOLZ reflection set obtained from the superposition of both the single crystal FOLZ reflection sets, i.e. those reflections indicated in figure 5.2.20c.

This behaviour could be explained if a diffracted beam leaving crystal I is subsequently diffracted by crystal II. It must be possible to confirm this behaviour, if valid, using the simulation program.

In order to use the simulation program in this case, a number of quantities has to be determined. Firstly, the reflection in question has to be indexed. The most probable construction for the subsequent diffraction observed is that the (0 $\bar{2}$ 2) reflection of either crystal I or II (the (2 $\bar{6}$ 4) reflection in CSL terms) and the (7 3 $\bar{9}$) reflection of either crystal II or I (the (23 $\bar{1}$ $\bar{21}$) reflection in CSL terms) gives the intensity profile in the (25 7 $\bar{17}$) reflection expressed in terms of the CSL. The symmetry related reflections of (25 7 $\bar{17}$) can be found by taking the symmetry related reflections of the contributing

91

(a)

(c)

(b)   figure 5.2.20

(d)
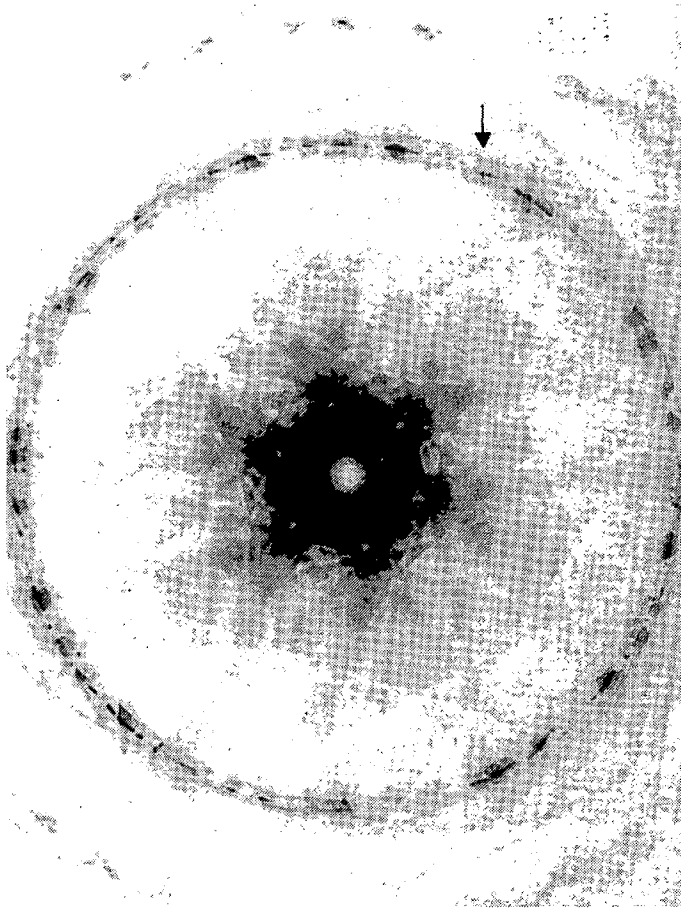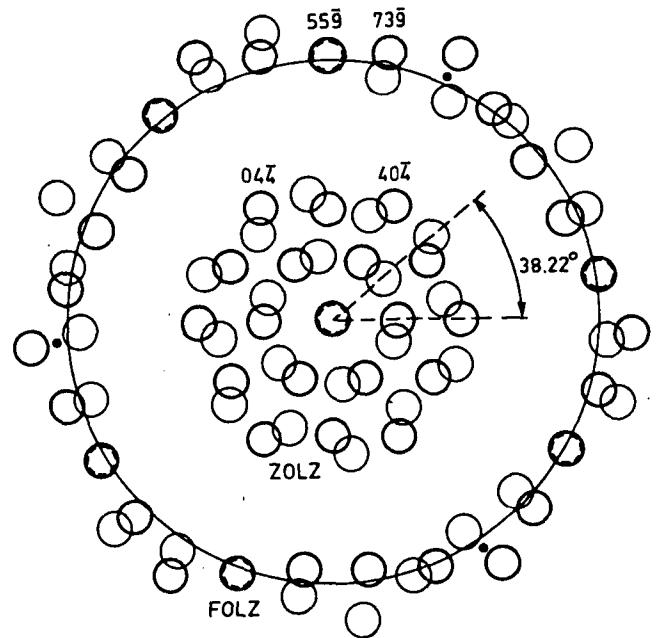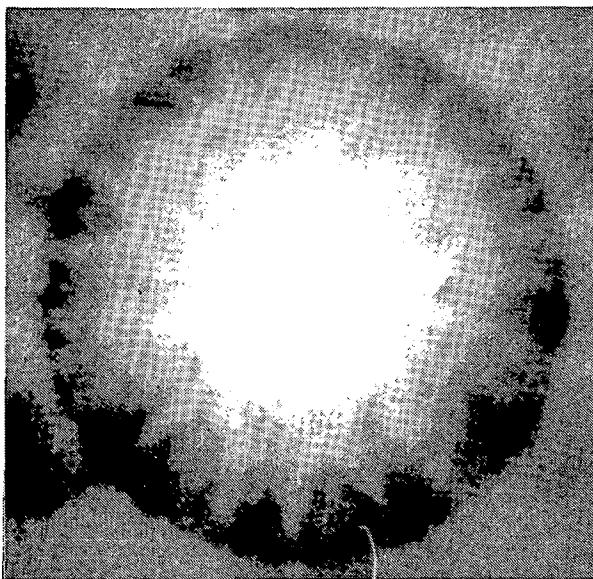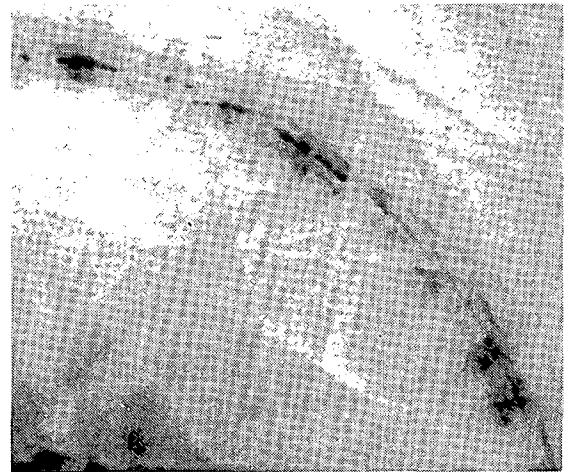
a) CBED pattern of a gold bicrystal (Σ=7) at 100 kV. The arrow indicates a CSL reflection originating from multiple diffraction in crystal I and crystal II. b) (000) disc magnification of a. c) Disc pattern for a, the circle indicates the intersection of Ewald sphere and FOLZ. d) Magnified micrograph of the region arrowed in a.

reflections. The positions of the three reflections in the CBED pattern is indicated by the dots in figure 5.2.20c.

Secondly, the thickness of the specimen has to be determined in order that a good comparison of the experimental and computed images can be made. From the assumed specimen configuration, as illustrated in figure 5.2.21, the total (bicrystal) specimen thickness has been determined to be 850 Å±10%, based on the individual thickness of the constituent single crystals.

Thirdly, the position of the interface has to be known for performing the calculation. From figure 5.2.21 it follows that the position of the boundary is at 0.46. For the calculations a value of 0.5 has been used. This value is allowed, since it is within the inaccuracy of the thickness measurement using the extinction contour method. In addition, it is assumed that the process of subsequent diffraction is not disturbed by the position of the interface, unless in extreme cases (crystal I very thin compared to crystal II, or vice versa).

The calculation has been based on 34 reflections including the $\langle 2\ \bar{6}\ 4 \rangle$, $\langle 7\ 3\ \bar{9} \rangle$ and $\langle 25\ 7\ \bar{17} \rangle$ reflections and a total of 21 FOLZ reflections. The accelerating voltage is identical to the experimental case, taken to be 100 kV. Absorption has been taken into account with an absorption factor of 0.1.

The result is shown in figure 5.2.22. The discs are presented correctly in their relative orientation, but incorrectly in their mutual distances (scaling). For reference, the $(19\ 5\ \bar{23})$ reflection disc is also included. The (000) disc shows the 3-fold symmetry as expected (the fact that its pattern is different from the image shown in figure 5.2.12a is explained by the fact that in both calculations different sets of reflections have been used; see also Appendix C). The intensity profile of the $(19\ 5\ \bar{23})$ reflection disc is concentric with the origin of the pattern. The intensity profile of the $(25\ 7\ \bar{17})$ reflection disc is clearly deviating from this concentric situation. The calculations therefore confirm the suggestion that the reflection in question is the $\langle 25\ 7\ \bar{17} \rangle$ CSL reflection which is generated by the subsequent diffraction in crystal II of a diffracted beam leaving crystal I.
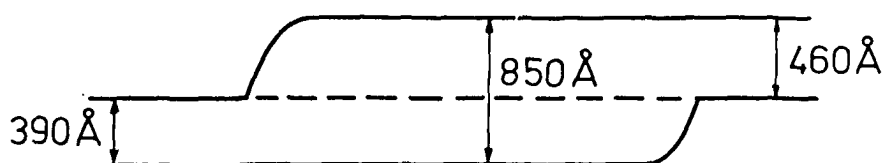
figure 5.2.21

Specimen configuration for the thickness determination of the specimen belonging to figure 5.2.20.

19 5 $\overline{23}$

(5 5 $\overline{9}$)

25 $\overline{7}$ $\overline{17}$

27.8°

000
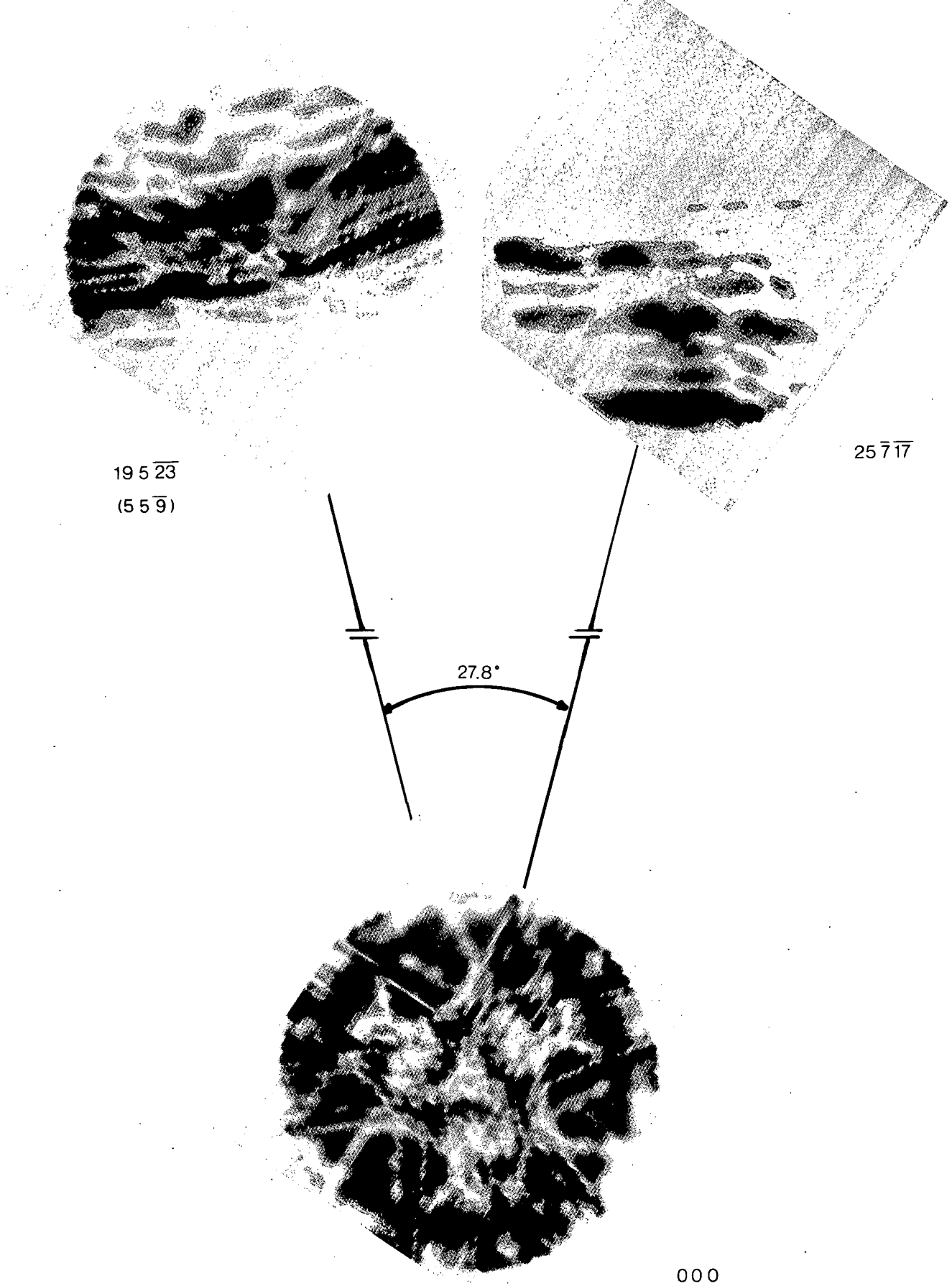
figure 5.2.22

Calculated CBED pattern showing the relative orientation of the (25 7 $\overline{17}$) and (19 5 $\overline{23}$) disc (expressed in terms of the CSL) for a Au bicrystal (Σ=7). The intensity profile of the (25 7 $\overline{17}$) is not concentric with the origin of the pattern.

94

5.2.7 Miscellaneous : the Tanaka method.

In CBED the separation of diffraction discs is limited by the Bragg angle of the nearest reflection. In cases in which the specimen involved has a large lattice spacing, overlap of reflection discs is more likely. To overcome this problem, the Tanaka method or Large Angle CBED (LACBED) method [Tanaka et al. 1980] can be of help to detect the symmetry present in the discs without interference from overlap.

In the Tanaka method, a large angle of convergence 3 to 5 times as large as in normal CBED, is used. In order to separate the transmitted and the diffracted beams, the specimen is raised slightly from its focussed position to a defocussed position. The central bright field beam can then be selected using the diffraction aperture.

An experimental example of the Tanaka method is illustrated in figure 5.2.23a which shows the pattern of the transmitted beam in a <1 1 1> ZAP of a single crystal specimen of gold. The thickness of the specimen was determined to be 460 $\overset{o}{A}\pm10\%$. The accelerating voltage was set at 100 kV. The angle of convergence is determined to be 1.90 ± 0.02^o. The calculated image is presented in figure 5.2.20b. The angle of convergence has been set to a wide angle of 1.5^o. Absorption is treated with an absorption factor of 0.1. The images show good agreement, both in detail and

(a)   (b)
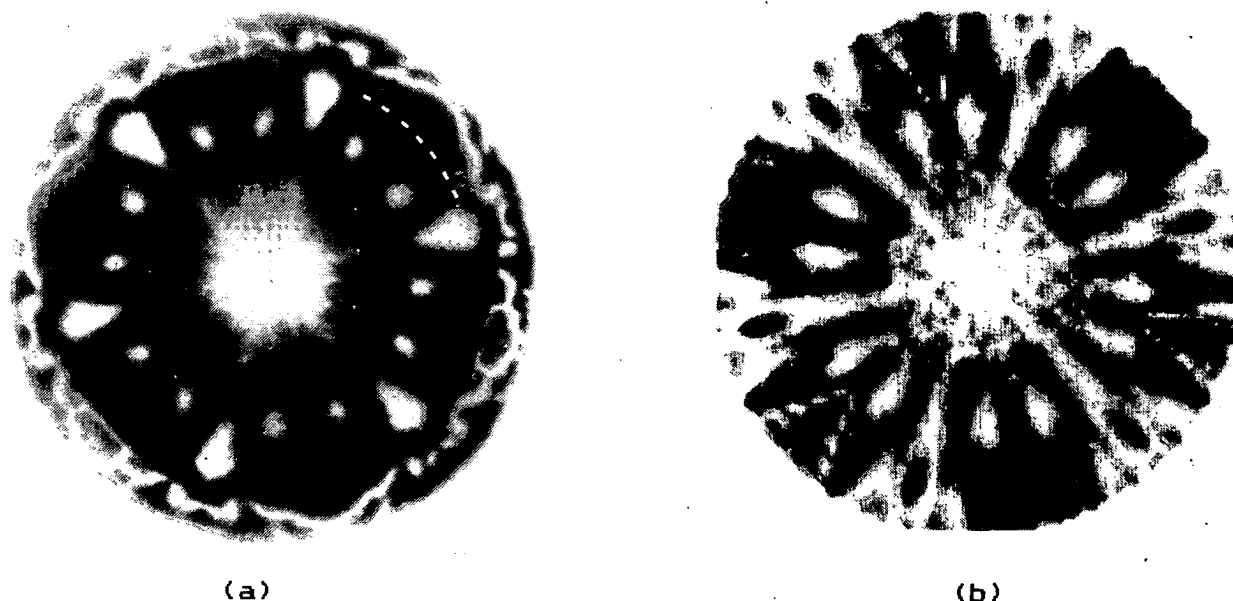
figure 5.2.23

a) Experimental example of the Tanaka or Large angle method on a gold single crystal specimen. b) Computed equivalent of a. The angle of convergence is 1.90 ± 0.02^o and 1.5^o respectively. Comparison can be performed within the dotted line of 5.2.23a.

in symmetry (3m). The angle of convergence is not exactly equal in both cases, which explains why the details seen near the edge of the disc in the experimental image are not observed in the computed image. The images are therefore only comparible within the dotted line indicated in the experimental image.

5.3   Conclusions.

In the previous sections results have been presented of CBED patterns obtained using a theoretical model. With this model it has been established that it is possible to calculate the CBED pattern resulting from specific types of specimen as defined in sections 2.1.2 and 3.1, i.e. involving a parallel-sided single crystal or a parallel-sided combination of two homogeneous crystals separated by the interface.
Based on the simulations presented, often in connection with the experimental data, the following conclusions can be drawn.

A   Single crystal specimens.
1) The position of the HOLZ lines within the calculated (OOO) disc of the CBED pattern is in agreement, including dynamical effects, with that which is experimentally observed, provided that the accelerating voltage is identical in both cases.
2) In order to obtain good agreement with experimental work, only those HOLZ reflections which are excited within the angle of convergence of the incident beam need to be included in the calculations. Of course, if more reflections are included, there will be more Bloch waves and a better approximation is obtained, although the image does not change noticeably.
3) In order to obtain a good agreement between the calculated and experimental image the thickness of the specimen must be known. In the case of silicon it has been reasoned that since absorption can be neglected, thickness differences appear only in the position and number of the thickness contours in the (OOO) disc. In the case of gold, on the other hand, the calculated images change noticeably with thickness. In these cases the thickness of the specimen should be known to within at least 10% accuracy.
4) The treatment of absorption using first-order perturbation methods leads to satisfying results. A simple relation between thickness and absorption is difficult to establish, since purely elastically diffracted intensities are thickness dependent. In addition, the absorption factor is different for each Bloch wave and diffraction direction.
5) The effect of absorption may destroy those symmetry elements in the CBED pattern which are induced by horizontal crystallographic symmetry operations. In the case of GaAs the effect is not noticeable. In tha case of gold the effect is such, that the reciprocity relation must be treated with care.

B   Bicrystal specimens.
1) From the example of a silicon bicrystal having a $\Sigma=3$ type boundary perpendicular to <1 1 1>, it has been shown that good agreement can be obtained when the set of single crystal

reflections is extended to include the set of reflections that are generated by the rotation relation between crystal I and crystal II. In this relatively simple example it means that the ZOLZ reflection set is identical to that of the single crystal, i.e. the set of ZOLZ reflections is common to both crystals. The set of FOLZ reflections is doubled in number, i.e. extended with the set that is generated as a result of the 60° rotation.

2) Simulations based on the example of a silicon bicrystal specimen with a $\langle 1 \; 1 \; 1 \rangle$ $\Sigma=3$ type boundary, have shown that, even a slight deviation from the symmetrical boundary position destroys the symmetry in the CBED pattern arising from horizontal symmetry elements.

3) Calculations have shown that the state of translation at the boundary can, in specific cases, be determined from the symmetry of the CBED pattern, in agreement with Schapink and Mertens' work [1981]. It has been illustrated that, although different states of translation are applied, the image profiles are, apart from the symmetry, remarkably similar. Therefore, this determination should be treated with care and only in cases in which the symmetry of the pattern can be clearly observed.

4) In the experimental image of a $\langle 1 \; 1 \; 1 \rangle$ ZAP at 100 kV, of a gold bicrystal specimen having a $\Sigma=7$ type boundary, a reflection in the FOLZ ring is observed which cannot be indexed according to the set of reflections obtained from the superposition of the FOLZ reflections of the individual crystals. The simulations have proved that the reflection in question is constructed from the $\langle 0 \; \bar{2} \; 2 \rangle$ reflection in crystal I or II and the $\langle 7 \; 3 \; \bar{9} \rangle$ reflection in crystal II or I respectively.

5) In analogy with the case of a single crystal of gold, in both the cases involving gold bicrystals having a $\Sigma=3$ and $\Sigma=7$ type boundary in the symmetrical position, the effect of absorption destroys the symmetry in the CBED pattern that is expected from horizontal coloured symmetry elements in the bicrystal. Therefore in cases of a gold bicrystal undergoing absorption, the reciprocity relation can no longer be applied.

A1   Orthonormalization.

Consider in the most general case a triclinic lattice defined by the three basic translation vectors $\underline{a}$, $\underline{b}$ and $\underline{c}$ with enclosing angles α, β and γ. The reciprocal lattice is then defined in the usual way [Int. Tables of Xray Cryst. vol I] by $\underline{a}^* = (\underline{b} \times \underline{c})/V$, $\underline{b}^* = (\underline{c} \times \underline{a})/V$ and $\underline{c}^* = (\underline{a} \times \underline{b})/V$ with the enclosing angles α^*, β^* and γ^*, where V denotes the volume of the unit cell enclosed by the vectors $\underline{a}$, $\underline{b}$ and $\underline{c}$.
An orthonormal coordinate system can be superimposed on the triclinic coordinate system (fig. A.1.1). The choice is made for the coincidence of the a-axis of the triclinic system with the X-axis of the orthonormal system, and the b-axis of the triclinic system being orientated in the XY plane of the orthonormal coordinate system.
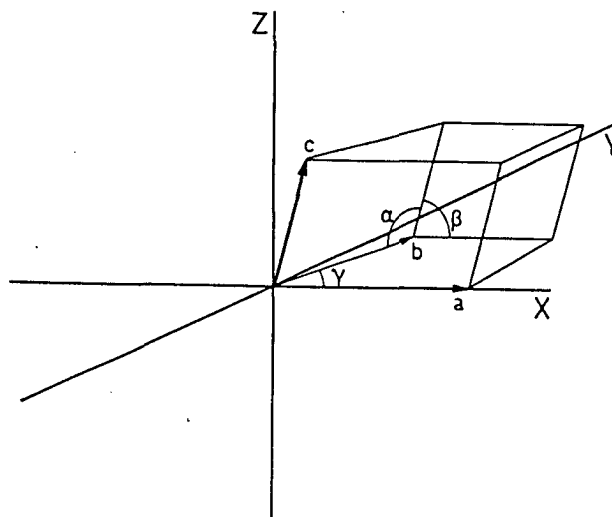
figure A.1.1

The superposition of an orthonormal coordinate system onto a triclinic coordinate system.

The orthonormalization matrix is defined as the transformation redefining a vector from triclinic coordinates $\underline{v}_t$ into orthonormal coordinates $\underline{v}_o$:

$$\underline{v}_o = O_d \underline{v}_t \qquad\qquad A.1.1$$

where O_d stands for the orthonormalization matrix in direct space. The matrix-vector product is calculated in the standard way, i.e. rows versus column (see for instance Bollmann 1982). It is easily seen that if

$$O_d = \begin{matrix} a_x & b_x & c_x \\ a_y & b_y & c_y \\ a_z & b_z & c_z \end{matrix} \qquad\qquad A.1.2$$

where a_x is the x-component of $\underline{a}$ in orthonormal units etc., every linear combination of $\underline{a}$, $\underline{b}$ and $\underline{c}$ can be transformed in this way [Int. Tables of Xray Cryst. vol I]. Evaluation of O_d, using $\det(O_d)=V$ and $|\underline{c}|^2 = c_x^2 + c_y^2 + c_z^2$ results in the orthogonalisation matrix :

$$O_d = \begin{matrix} a & b\cos\gamma & c\cos\beta \\ 0 & b\sin\gamma & c(\cos\alpha - \cos\beta\cos\gamma)/\sin\gamma \\ 0 & 0 & cq/\sin\gamma \end{matrix} \qquad A.1.3$$

with $q = \sqrt{(1 - \cos^2\alpha - \cos^2\beta - \cos^2\gamma + 2\cos\alpha\cos\beta\cos\gamma)}$.

In the same way it is possible to set up an orthonormalization matrix O_r, which redefines a vector $\underline{h}_t$ from reciprocal space into orthonormal units $\underline{h}_o$:

$$\underline{h}_o = O_r\underline{h}_t \qquad\qquad A.1.4$$

Because of the relation between $\underline{a}$ and $\underline{a}^*$, $\underline{b}$ and $\underline{b}^*$ and $\underline{c}$ and $\underline{c}^*$, O_r is given by :

$$O_r = 1/V \begin{matrix} (\underline{b} \times \underline{c})_x & (\underline{c} \times \underline{a})_x & (\underline{a} \times \underline{b})_x \\ (\underline{b} \times \underline{c})_y & (\underline{c} \times \underline{a})_y & (\underline{a} \times \underline{b})_y \\ (\underline{b} \times \underline{c})_z & (\underline{c} \times \underline{a})_z & (\underline{a} \times \underline{b})_z \end{matrix} \qquad A.1.5$$

in which $(\underline{b} \times \underline{c})_x = a_x^* = b_yc_z - c_yb_z$ etc..

Consider the transpose of the adjoint matrix of O_d, i.e. the matrix composed of the sub-determinants of O_d :

$$(adj(O_d))^T = \begin{matrix} b_yc_z-c_yb_z & c_ya_z-a_yc_z & a_yb_z-b_xa_z \\ c_xb_z-b_xc_z & a_xc_z-c_xa_z & b_xa_z-a_xb_z \\ b_xc_y-c_xb_y & c_xa_y-a_xc_y & a_xb_y-b_xa_y \end{matrix} \qquad A.1.6$$

99

therefore

$$O_r = (adj(O_d))^T/V \qquad\qquad A.1.7$$

From the definition of the inverse of O_d,

$$O_d^{-1} = adj(O_d)/V \qquad\qquad A.1.8$$

we have

$$O_r = (O_d^{-1})^T \qquad\qquad A.1.9$$

The transformation of a vector from direct to reciprocal space $T_{d->r}$ and vice versa the transformation from reciprocal to direct space $T_{r->d}$ are defined as

$$T_{d->r} = O_r^{-1}.O_d \qquad\qquad A.1.10$$

$$T_{r->d} = O_d^{-1}.O_r \qquad\qquad A.1.11$$

respectively, with the relation

$$T_{r->d}^{-1} = (O_d^{-1}.O_r)^{-1} = O_r^{-1}.O_d = T_{d->r} \qquad\qquad A.1.12$$

A2   Rotations

In orthonormal 3-dimensional space a rotation is represented by an orthogonal transformation ($R^{-1} = R^T$), i.e. it preserves the norm of a vector (det(R)= 1). If a rotation matrix is defined as

$$R_o = \begin{array}{ccc} r_{11} & r_{12} & r_{13} \\ r_{21} & r_{22} & r_{23} \\ r_{31} & r_{32} & r_{33} \end{array} \qquad\qquad A.2.1$$

the angle of rotation θ can be calculated from the trace t of R_o:

$$t = r_{11} + r_{22} + r_{33} = 2cos\theta + 1 \qquad\qquad A.2.2$$

The axis of rotation $\underline{l}$, one of the eigen vectors of the rotation matrix, can be calculated from $\underline{l} = (r_{23}-r_{32}, r_{31}-r_{13}, r_{12}-r_{21})$.

With the axis of rotation pointing towards the viewer[+], the angle of rotation forms a right handed screw with respect to $\underline{l}$ (figure A.2.1).
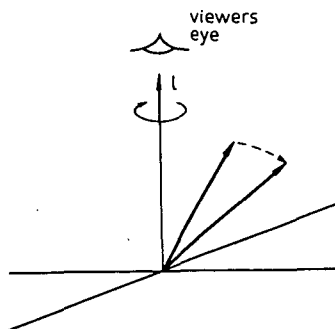
figure A.2.1

The definition of rotation. The choice is departing from the conventional definition.

In the more general triclinic case, a rotation matrix in direct space is defined as :

$$R_d = O_d^{-1} R_o O_d \qquad\qquad A.2.3$$

and its equivalent rotation in reciprocal space as :

$$R_r = O_r^{-1} R_o O_r \qquad\qquad A.2.4$$

in which O_d and O_r are the orthonormalization matrices for direct space and reciprocal space respectively (see A1). The above similarity transformation preserve the determinant of the matrices R, but not their orthogonality. Using the standard matrix relations $(AB)^T = B^T A^T$ and $(AB)^{-1} = B^{-1} A^{-1}$ together with eqs. A.2.4 and A.1.9, it follows

$$(R_r^T)^{-1} = ((O_r^{-1} R_o O_r)^T)^{-1} = O_r^T R_o^T (O_r^{-1})^T$$

$$= (O_d^{-1} R_o^T O_d)^{-1} = O_d^{-1} (R_o^T)^{-1} O_d \qquad\qquad A.2.5$$

Comparing this result with eq. A.2.3, together with the orthogonality principle $R_o = (R_o^{-1})^T$, we have

$$R_d = (R_r^{-1})^T \qquad\qquad A.2.6$$

_____

[+] It must be noted that the definition of the rotation direction is contrary to the usual convention.

APPENDIX B

B1 **The relation between the 58 dichromatic point groups and the 31 diffraction groups.**

Tables I and II give the relation between 58 of the dichromatic point groups (since the 32 classical and the 32 grey point groups are not of interest they have been left out) and the 31 diffraction groups suggested by Buxton et al. [1976]. Table I has been reproduced from Schapink et al. [1983], table II has been reproduced from Buxton et al. [1984].

In both tables the **X** indicate the possible diffraction group for each dichromatic point group depending on the direction of view; the **O** indicate that the projection approximation has been applied.

Table I

The relation between the diffraction groups and dichromatic point groups for bicrystals with Σ > 1.

102

	1	1R	2	2R	21R	mR	3	m1R	2mRmR	2mm	2RmmR	2mm1R	4	4R	41R	4mRmR	4mm	4RmmR	4mm1R	3	6R	3mR	3m	6RmmR	6	31R	61R	6mRmR	6mm	3m1R	6mm1R
$\bar{1}'$				X	O																										
2'/m				X	O						X	O																			
2/m'				X	⊗							O																			
m'mm				X	O						X	⊗																			
m'm'm'				X	⊗							O																			
4/m'				X	O							O						⊗													
4'/m'				X	⊗							O						O													
4/m'mm				X	O						X	O					⊗														
4'/m'm'm				X	⊗						X	⊗					O														
4/m'm'm'				X	⊗							O		X			O														
$\bar{3}'$				X	O																X				O						
$\bar{3}'m$				X	O						X	O											X								O
$\bar{3}'m'$				X	⊗							O									X										O
6'/m				X	O						X	O									X				O						
6/m'				X	O							O															⊗				
6/m'mm				X	O						X	O																			⊗
6'/mm'm				X	O						X	⊗											X								O
6/m'm'm'				X	⊗							O															X				O
m'3				X	⊗							O									X				O						
4'32'	X	O				X		O	X			O					O						X						O		
$\bar{4}'3m'$	X	⊗							O						X		O	X											O		
m3m				X	O						X	⊗					O						X								O
m3m'	X			O		X	X	X				O				X	O					X									O
m'3m'				X	⊗							O		X			O				X										O

Table II

The relation between the diffraction groups and dichromatic point groups for bicrystals with $\Sigma = 1$, i.e. either belonging to a group with $\bar{1}'$, or to a cubic group.

APPENDIX C

C1   List of calculation parameters.

In section 5.2 the calculated results are presented giving the values of only the parameters of interest. In the list below a detailed description of the used calculation parameters is given for each of the simulations. The numbers given refer to the figure numbers used in section 5.2.

Crystallographic properties :

    Silicon (Si)
    space group Fd$\bar{3}$m, a=5.4305 Å
    atomic positions: 0   0   0
                        1/8 1/8 1/8
                        1/8 5/8 5/8
                        5/8 1/8 5/8
                        5/8 5/8 1/8
                        7/8 7/8 7/8
                        3/8 3/8 7/8
                        3/8 7/8 3/8
                        7/8 3/8 3/8
    Cromer-Waber coeff. :   5.6627 2.6652 3.0716 38.6634 2.6245
                            0.9195 1.3932 93.5458 1.2471
    electron scatt. (s=0) :   6.00 Å

    Gold (Au)
    space group Fm$\bar{3}$m, a=4.0702 Å
    atomic positions: 0   0   0
                        1/2 1/2 0
                        1/2 0   1/2
                        0   1/2 1/2
    Cromer-Waber coeff. : 16.8819 0.4611 18.5913 8.6216 25.5582
                            1.4826 5.8600 36.3956 12.0658
    electron scatt. (s=0) :   10.57 Å

    Gallium-Arsenide (GaAs)
    space group F$\bar{4}$3m, a=5.6543 Å
    atomic positions: Ga   As
                        0   0   0   1/4 1/4 1/4
                        1/2 1/2 0   3/4 3/4 1/4
                        1/2 0   1/2   3/4 1/4 3/4
                        0   1/2 1/2   1/4 3/4 3/4
    Cromer-Waber coeff. : Ga 15.2354 3.0669 6.7006 0.2412 4.3591
                            10.7805 2.9623 61.4135 1.7189
                          As 16.6723 2.6345 6.0701 0.2647 3.4313
                            12.9479 4.2779 47.7972 2.5310
    electron scatt. (s=0) :   Ga 7.11 Å
                              As 7.32 Å

5.2.3a

    Crystal type : silicon, single crystal
    Thickness : 2000 Å
    Accelerating voltage : 102.7 kV
    No. of reflections : 22
    Reflections : (0 0 0), 6×<2 $\bar{2}$ 0>, 6×<4 $\bar{2}$ $\bar{2}$>, 6×<9 1 $\bar{9}$>,
              3×<$\bar{5}$ $\bar{5}$ 11>
    Angle of convergence : 0.2⁰

5.2.5

    Crystal type : silicon, single crystal
    Thickness : 2000 Å
    Accelerating voltage : 102.7 kV
    No. of reflections : 22
    Reflections : (0 0 0), 6×<2 $\bar{2}$ 0>, 6×<4 $\bar{2}$ $\bar{2}$>, 6×<9 1 $\bar{9}$>,
              3×<$\bar{5}$ $\bar{5}$ 11>
    Angle of convergence : 0.2⁰

5.2.6a

    Crystal type : silicon, single crystal
    Thickness : 2000 Å
    Accelerating voltage : 100 kV
    No. of reflections : 88 (see footnote on page 73)
    Reflections : (0 0 0), 6×<2 $\bar{2}$ 0>, 6×<4 $\bar{2}$ $\bar{2}$>, 6×<4 $\bar{4}$ 0>,
             6×<6 $\bar{6}$ 0>, 6×<2 $\bar{6}$ 4>, 6×<4 $\bar{6}$ 2>, 6×<11 $\bar{1}$ $\bar{9}$>,
             5×<9 3 $\overline{11}$>, 6×<9 1 $\bar{9}$>, 6×<7 3 $\bar{9}$>, 6×<7 5 $\overline{11}$>,
             3×<5 5 $\bar{9}$>, 5×<$\bar{3}$ 11 7>, 6×<$\bar{3}$ 9 5>, 3×<$\bar{5}$ 11 $\bar{5}$>,
             5×<$\bar{1}$ 9 7>
    Angle of convergence : 0.2⁰

5.2.7a

    Crystal type : gold, single crystal
    Thickness : 230 Å
    Accelerating voltage : 100 kV
    No. of reflections : 34
    Reflections : (0 0 0), 6×<2 $\bar{2}$ 0>, 6×<4 $\bar{2}$ $\bar{2}$>, 6×<7 $\bar{9}$ 3>,
             3×<5 $\bar{9}$ 5>, 6×<$\bar{1}$ 7 9>, 6×<3 $\bar{5}$ 9>
    Angle of convergence : 0.4⁰
    Absorption factor : 0.1

5.2.7b

    Crystal type : gold, single crystal
    Thickness : 300 Å
    Accelerating voltage : 100 kV
    No. of reflections : 34
    Reflections : (0 0 0), 6×<2 $\bar{2}$ 0>, 6×<4 $\bar{2}$ $\bar{2}$>, 6×<7 $\bar{9}$ 3>,
             3×<5 $\bar{9}$ 5>, 6×<$\bar{1}$ 7 9>, 6×<3 $\bar{5}$ 9>
    Angle of convergence : 0.4⁰
    Absorption factor : 0.1

5.2.7c

    Crystal type : gold, single crystal
    Thickness : 350 Å
    Accelerating voltage : 100 kV
    No. of reflections : 34

Reflections : (0 0 0), 6×<2 2̄ 0>, 6×<4 2̄ 2̄>, 6×<7 9̄ 3>,
            3×<5 9̄ 5>, 6×<1̄ 7 9>, 6×<3̄ 5̄ 9>
Angle of convergence : 0.4°
Absorption factor : 0.1

5.2.7d
Crystal type : gold, single crystal
Thickness : 400 Å
Accelerating voltage : 100 kV
No. of reflections : 34
Reflections : (0 0 0), 6×<2 2̄ 0>, 6×<4 2̄ 2̄>, 6×<7 9̄ 3>,
            3×<5 9̄ 5>, 6×<1̄ 7 9>, 6×<3̄ 5̄ 9>
Angle of convergence : 0.4°
Absorption factor : 0.1

5.2.7e
Crystal type : gold, single crystal
Thickness : 460 Å
Accelerating voltage : 100 kV
No. of reflections : 34
Reflections : (0 0 0), 6×<2 2̄ 0>, 6×<4 2̄ 2̄>, 6×<7 9̄ 3>,
            3×<5 9̄ 5>, 6×<1̄ 7 9>, 6×<3̄ 5̄ 9>
Angle of convergence : 0.4°
Absorption factor : 0.1

5.2.9a
Crystal type : gold, single crystal
Thickness : 600 Å
Accelerating voltage : 100 kV
No. of reflections : 34
Reflections : (0 0 0), 6×<2 2̄ 0>, 6×<4 2̄ 2̄>, 6×<7 9̄ 3>,
            3×<5 9̄ 5>, 6×<1̄ 7 9>, 6×<3̄ 5̄ 9>
Angle of convergence : 0.2°
Absorption factor : 0.1

5.2.9b
Crystal type : gold, single crystal
Thickness : 600 Å
Accelerating voltage : 100 kV
No. of reflections : 34
Reflections : (0 0 0), 6×<2 2̄ 0>, 6×<4 2̄ 2̄>, 6×<7 9̄ 3>,
            3×<5 9̄ 5>, 6×<1̄ 7 9>, 6×<3̄ 5̄ 9>
Angle of convergence : 0.2°
Absorption factor : no absorption

5.2.10a
Crystal type : gold, single crystal
Thickness : 460 Å
Accelerating voltage : 100 kV
No. of reflections : 34
Reflections : (0 0 0), 6×<2 2̄ 0>, 6×<4 2̄ 2̄>, 6×<7 9̄ 3>,
            3×<5 9̄ 5>, 6×<1̄ 7 9>, 6×<3̄ 5̄ 9>
Angle of convergence : 0.2°
Absorption factor : 0.05

5.2.10b

Crystal type : gold, single crystal
Thickness : 460 Å
Accelerating voltage : 100 kV
No. of reflections : 34
Reflections : (0 0 0), 6×<2 $\bar{2}$ 0>, 6×<4 $\bar{2}$ $\bar{2}$>, 6×<7 $\bar{9}$ 3>,
  3×<5 $\bar{9}$ 5>, 6×<$\bar{1}$ 7 9>, 6×<$\bar{3}$ 5 9>
Angle of convergence : 0.4⁰
Absorption factor : 0.1

5.2.11a

Crystal type : gallium-arsenide, single crystal; radial-scan
Thickness : 400 Å
Accelerating voltage : 100 kV
No. of reflections :25
Zone axis : 1 $\bar{1}$ 0
Reflections : (0 0 0), 2×<2 2 0>, 2×<0 0 2>, 4×<1 1 1>,
  4×<1 1 3>, 4×<3 3 1>, 4×<7 5 19>, 4×<1 9 15>
Angle of convergence : 0.4⁰
Absorption factor : no absorption

5.2.11b

Crystal type : gallium-arsenide, single crystal; radial-scan
Thickness : 400 Å
Accelerating voltage : 100 kV
No. of reflections :25
Zone axis : 1 $\bar{1}$ 0
Reflections : (0 0 0), 2×<2 2 0>, 2×<0 0 2>, 4×<1 1 1>,
  4×<1 1 3>, 4×<3 3 1>, 4×<7 5 19>, 4×<1 9 15>
Angle of convergence : 0.4⁰
Absorption factor : 0.1

5.2.11c

Crystal type : gallium-arsenide, single crystal; radial-scan
Thickness : 800 Å
Accelerating voltage : 100 kV
No. of reflections :25
Zone axis : 1 $\bar{1}$ 0
Reflections : (0 0 0), 2×<2 2 0>, 2×<0 0 2>, 4×<1 1 1>,
  4×<1 1 3>, 4×<3 3 1>, 4×<7 5 19>, 4×<1 9 15>
Angle of convergence : 0.4⁰
Absorption factor : 0.1

5.2.12a

Crystal type : gold, bicrystal
Thickness : 850 Å
Accelerating voltage : 100 kV
No. of reflections : 49
Reflections : (0 0 0), 6×<2 $\bar{2}$ 0>, 6×<7 $\bar{9}$ 3>, 3×<5 $\bar{9}$ 5>,
  6×<$\bar{1}$ 7 9>, 6×<$\bar{3}$ 5 9> + the equivalent
  non-commons of crystal II
Angle of convergence : 0.4⁰
Absorption factor : 0.1
Rotation relation : 38.22⁰
Translation relation : no translation

```
Position of boundary : 0.5
CSL transformation matrix :      2  -1   0
                                 0   2  -1
                                -1   0   2
```

5.2.12b
```
Crystal type : gold, bicrystal
Thickness : 850 Å
Accelerating voltage : 100 kV
No. of reflections : 49
Reflections : (0 0 0), 6×<2 2̄ 0>, 6×<7 9̄ 3>, 3×<5 9̄ 5>,
              6×<1̄ 7 9>, 6×<3̄ 5 9> + the  equivalent
              non-commons of crystal II
Angle of convergence : 0.4⁰
Absorption factor  : no absorption
Rotation relation : 38.22⁰
Translation relation : no translation
Position of boundary : 0.5
CSL transformation matrix :      2  -1   0
                                 0   2  -1
                                -1   0   2
```

5.2.15a
```
Crystal type : silicon, bicrystal
Thickness : 2000 Å
Accelerating voltage : 100 kV
No. of reflections : 31
Reflections : (0 0 0), 6×<2 2̄ 0>, 6×<4 2̄ 2̄>, 6×<9 1 9̄>,
              3×<5̄ 5̄ 11> + the equivalent non-commons of
              crystal II
Angle of convergence : 0.2⁰
Rotation relation : 60⁰
Translation relation : no translation
Position of boundary : 0.5
CSL transformation matrix :      1   0  -1
                                -1   1   0
                                 1   1   1
```

5.2.15b
```
Crystal type : silicon, bicrystal
Thickness : 2000 Å
Accelerating voltage : 100 kV
No. of reflections : 31
Reflections : (0 0 0), 6×<2 2̄ 0>, 6×<4 2̄ 2̄>, 6×<9 1 9̄>,
              3×<5̄ 5̄ 11> + the equivalent non-commons of
              crystal II
Angle of convergence : 0.2⁰
Rotation relation : 60⁰
Translation relation : no translation
Position of boundary : 0.48
CSL transformation matrix :      1   0  -1
                                -1   1   0
                                 1   1   1
```

5.2.15c

    Crystal type : silicon, bicrystal
    Thickness : 2000 Å
    Accelerating voltage : 100 kV
    No. of reflections : 31
    Reflections : (0 0 0), 6×⟨2 $\bar{2}$ 0⟩, 6×⟨4 $\bar{2}$ $\bar{2}$⟩, 6×⟨9 1 $\bar{9}$⟩,
              3×⟨$\bar{5}$ $\bar{5}$ 11⟩ + the equivalent non-commons of
              crystal II
    Angle of convergence : 0.2⁰
    Rotation relation : 60⁰
    Translation relation : no translation
    Position of boundary : 0.46
    CSL transformation matrix :   1   0 −1
                                      −1   1   0
                                        1   1   1

5.2.16b

    Crystal type : gold, bicrystal
    Thickness : 800 Å
    Accelerating voltage : 100 kV
    No. of reflections : 55
    Reflections : (0 0 0), 6×⟨2 $\bar{2}$ 0⟩, 6×⟨4 $\bar{2}$ $\bar{2}$⟩, 6×⟨7 $\bar{9}$ 3⟩,
              3×⟨5 $\bar{9}$ 5⟩, 6×⟨$\bar{1}$ 7 9⟩, 6×⟨$\bar{3}$ 5 9⟩
                  + the equivalent non-commons of crystal II
    Angle of convergence : 0.4⁰
    Absorption factor   : 0.1
    Rotation relation : 60⁰
    Translation relation : no translation
    Position of boundary : 0.5
    CSL transformation matrix :   1   0 −1
                                        −1   1   0
                                        1   1   1

5.2.18a

    Crystal type : silicon, bicrystal
    Thickness : 2000 Å
    Accelerating voltage : 100 kV
    No. of reflections : 31
    Reflections : (0 0 0), 6×⟨2 $\bar{2}$ 0⟩, 6×⟨4 $\bar{2}$ $\bar{2}$⟩, 6×⟨9 1 $\bar{9}$⟩,
              3×⟨$\bar{5}$ $\bar{5}$ 11⟩ + the equivalent non-commons of
              crystal II
    Angle of convergence : 0.2⁰
    Rotation relation : 60⁰
    Translation relation : 1/12⟨$\bar{1}$ 2 $\bar{1}$⟩
    Position of boundary : 0.5
    CSL transformation matrix :   1   0 −1
                                        −1   1   0
                                        1   1   1

5.2.19a

    Crystal type : silicon, bicrystal
    Thickness : 2000 Å
    Accelerating voltage : 100 kV
    No. of reflections : 31
    Reflections : (0 0 0), 6×⟨2 $\bar{2}$ 0⟩, 6×⟨4 $\bar{2}$ $\bar{2}$⟩, 6×⟨9 1 $\bar{9}$⟩,

$$3\times\langle 5\ \bar{5}\ 11\rangle\ +\ \text{the equivalent non-commons of crystal II}$$

Angle of convergence : 0.2⁰
Rotation relation : 60⁰
Translation relation : 1/6⟨0 1 Ī⟩
Position of boundary : 0.5
CSL transformation matrix :

$$\begin{array}{rrr} 1 & 0 & -1 \\ -1 & 1 & 0 \\ 1 & 1 & 1 \end{array}$$

5.2.22

Crystal type : gold, bicrystal
Thickness : 850 Å
Accelerating voltage : 100 kV
No. of reflections : 34
Reflections in terms of CSL : (0 0 0), 6×⟨2 $\bar{6}$ 2⟩, 6×⟨2 4 $\bar{6}$⟩, 6×⟨23 $\bar{21}$ $\bar{1}$⟩, 6×⟨15 $\bar{25}$ 11⟩, 3×⟨19 $\bar{23}$ 5⟩, 3×⟨$\bar{11}$ 25 $\bar{13}$⟩, 3×⟨7 25 $\bar{17}$⟩

Angle of convergence : 0.4⁰
Absorption factor : 0.1
Rotation relation : 38.22⁰
Translation relation : no translation
Position of boundary : 0.5
CSL transformation matrix :

$$\begin{array}{rrr} 2 & -1 & 0 \\ 0 & 2 & -1 \\ -1 & 0 & 2 \end{array}$$

5.2.23b

Crystal type : gold, single crystal
Thickness : 460 Å
Accelerating voltage : 100 kV
No. of reflections : 34
Reflections : (0 0 0), 6×⟨2 $\bar{2}$ 0⟩, 6×⟨4 $\bar{2}$ $\bar{2}$⟩, 6×⟨7 $\bar{9}$ 3⟩, 3×⟨5 $\bar{9}$ 5⟩, 6×⟨$\bar{1}$ $\bar{7}$ 9⟩, 6×⟨3 $\bar{5}$ 9⟩
Angle of convergence : 1.5⁰
Absorption factor : 0.1

References.

Acton F.S., (1970), Numerical Methods That Work (New York: Harper & Row).

Anstis G.R., (1977), Acta Cryst., A33, 844.

Baker J.R., (1982), Doctorate Thesis, Univ. Bristol.

Bethe H.A., (1928), Ann. Phys., Leipzig, 87, 55.

Blom N.S. & Schapink F.W., (1985), J. Appl. Cryst., 18, 126.

Bollmann W., (1970), Crystal Defects and Crystalline Interfaces (Berlin: Springer Verlag).

Bollmann W., (1982), Crystal Lattices, Interfaces, Matrices (Geneva: Bollmann).

Bragg W.L., (1913), Proc. Cambridge Phil. Soc., 17, 43.

Buxton B.F., (1976), Proc. R. Soc. London, A350, 335.

Buxton B.F., Eades J.A., Steeds J.W. & Rackham G.M., (1976) Phil. Trans. R. Soc., 281, 171.

Buxton B.F., Forghany S.K.E. & Schapink F.W., (1984), Inst. Phys. Conf. Ser. No. 68: Chapter 2, 59.

Cowley J.M., (1975), Diffraction Physics (Amsterdam: North-Holland).

Cowley J.M. & Moodie A.F., (1957), Acta Cryst., 10, 609.

Cowley J.M. & Moodie A.F., (1958), Proc. R. Soc, 71, 533.

Cowley J.M. & Moodie A.F., (1959a), Acta Cryst., 12, 353.

Cowley J.M. & Moodie A.F., (1959b), Acta Cryst., 12, 360.

Cromer D.T. & Waber J.T., (1965), Acta Cryst., 19, 104.

Dawson B., Goodman P., Johnson A.W.S., Lynch D. & Moodie A.F., (1974), Acta Cryst., A30, 297.

Doyle P.A. & Cowley J.M., (1974), Int. Tables Xray Cryst. vol IV, table 2.4.6C.

DSTT, (1974), Dict. Sc. Techn. Terms (New York: Mcgraw-Hill) 1353.

Friedel M.G., (1913), C. R. Acad. Sci., Paris, 157, 1533.

Friedel M.G., (1926), Leçons de Cristallographie (Paris: Berger-Levrault).

Fujiwara K., (1962), J. Phys. Soc. Japan, 17 suppl. BII, 118.

Gjonnes J.K. & Moodie A.F., (1965), Acta Cryst., 19, 65.

Goodman P., (1975), Acta Cryst., A31, 804.

Goodman P., (1984), Acta Cryst., A40, 635.

Goodman P. & Moodie A.F., (1974), Acta Cryst. A30, 280.

Gratias D. & Portier R., (1982), J. Physique, 43, coll. 6, 15.

Heine V., (1963), Proc. Phys. Soc., 81, 300.

Hirsch P.B., Howie A., Nicholson R.B., Pashley D.W. & Whelan M.J., (1965), Electron Microscopy of Thin Crystals (London: Butterworth).

Humphreys C.J., (1979), Rep. Prog. Phys., 42, 1825.

Humphreys C.J. & Fisher R.M., (1971), Acta Cryst., A27, 42.

Humphreys C.J. & Hirsch P.B., (1968), Phil. Mag., 18, 115.

Hwang K. & Briggs F.A., (1984), Computer Architectures and Parallel Processing (London: McGraw-Hill).

Ibers J.A., (1958), Acta Cryst., 11, 178.

International Tables for X-ray Crystallography, vol. I (1962) and vol IV (1974), (Birmingham: Kynoch Press/IUCr).

Ishizuka K., (1984), Acta Cryst., A suppl., 383.

Ishizuka K. & Uyeda N., (1977), Acta Cryst., A33, 740.

Jones P.M., Rackham G.M. & Steeds J.W., (1977), Proc. R. Soc. London, A354, 197.

Kalonji G., (1985), J. Physique, 46, coll. 4, 249.

Kikuchi S., (1928),Proc. Jap. Acad. Sci. 4, 271.

Laue M. von, (1935), Ann. Phys., Leipzig, 23, 705.

Lipson H. & Cochran W., (1953), The Determination of Crystal Structures (London: Bell & sons Ltd.).

Lynch D.F., (1971), Acta Cryst., A27, 399.

Miyake S. & Uyeda R., (1955), Acta Cryst., 8, 335.

Moodie A.F., (1965), Int. Conf. Elec. Diffr. Cryst. Defects, Melbourne.

Morris R.H., Bottoms W.R. & Peacock R.G., (1968), J. Appl. Phys., 39, 3016.

Mott N.F., (1930), Proc. R. Soc., A127, 658.

NAG-library, (1984), Numerical Algorithm Group, Mark 11.

Pizer S.M., Zimmerman J.B. & Johnston R.E., (1982), IEEE Trans. Nucl. Sc., 29-4, 1322.

Pogany A.P. & Turner P.S., (1968), Acta Cryst., A24, 103.

Pond R.C. & Bollmann W., (1979), Phil. Trans. R. Soc. London, A292, 449.

Pond R.C. & Vlachavas D.S., (1983), Proc. R. Soc. London, A386, 95.

Reimer L., (1984), Transmission Electron Microscopy (Berlin: Springer Verlag).

Schapink F.W., Blom N.S. & Forghany S.K.E., (1985) J. Physique Coll. C4 46 85

Schapink F.W. & Mertens F.J.M., (1981), Scr Metall., 15, 611.

Schapink F.W., Forghany S.K.E. & Buxton B.F., (1983), Acta Cryst., A39, 805.

Seitz F., (1936), Ann. Math., 37, 17.

Self P.G., O'Keefe M.A., Buseck P.R. & Spargo A.E.C., (1983), Ultramicroscopy, 11, 35.

Shannon M.D., (1978), Inst. Phys. Conf. Ser. No. 41: Chapter 1, 41.

Shannon R.E., (1975), Systems Simulation: the art and science (New York: Eaglewood Cliffs).

Sheinin S.S. & Corbett J.M., (1976), Phys. Status Solidi, A38, 675.

Shubnikov A.V., (1964), Coloured Symmetry (New York: Pergamon Press Inc.).

Shubnikov A.V. & Koptsik V.A., (1964), Symmetry in Art and Science (London: Plenum Press).

Sprague J.A. & Wilkens M., (1970), Proc. Septième Cong. Micr. Elec., Grenoble vol 1 (Paris: Société Française de Microscopie Electronique), 95.

Steeds J.W., Rackham G.M. & Shannon M.D., (1978), Inst. Phys. Conf. Ser. No. 41: Chapter 3, 135.

Steeds J.W., Baker J.R. & Vincent R., (1982), Electron Microscopie 1982, 617.

Sutton A.P. & Pond R.C., (1978), Phys. Status Solidi, A45, 149.

Tanaka M., Saito R., Ueno K. & Harada Y., (1980), J. Electron Microsc., 20, 408

Tanaka M., Sekii H. & Nagasawa T., (1983), Acta Cryst. A39, 825.

Tinappel A. (1975) Doctorate Thesis, Techn. Univ. Berlin.
Thiessen P.A. & Molière K., (1939), Ann. Physik, 34, 449.

Vainshtein B.K., (1981), Modern Crystallography I (Berlin: Springer Verlag).
Whelan M.J., (1962), J. Phys. Soc. Japan, 17 suppl. BII, 122.
Wilkinson J.H., (1965), The Algebraic Eigenvalue Problem (London: Oxford).
Yoshioka H., (1957), J. Phys. Soc. Japan, 12, 618.

Summary.

A brief introduction to this thesis is given in chapter 1. The fundamentals of Convergent Beam Electron Diffraction (CBED) are treated in chapter 2, in which a general description is given of the symmetry and the interpretation of CBED patterns, including the classification into the 31 diffraction groups as proposed by Buxton et al. [1976].

Chapter 3 deals with the subject of CBED patterns resulting from bicrystal specimens. The concept of colour symmetry is introduced to describe the bicrystal symmetry , after which the general construction of bicrystal space groups is discussed; the classification as given by Schapink et al. [1983] and Buxton et al. [1984], based on bicrystals having a CSL type boundary, is treated.

Chapter 4 is divided into two parts.
The first part gives a detailed description of the dynamical theory of diffraction, originally developed by Bethe [1928], including the effect of higher order Laue zone reflections. The first-order perturbation method for the description of absorption is included. A brief comparison is made between the Bloch wave method and the multi-slice method, which is an equivalent method for describing dynamical diffraction.
In the second part, the implementation based on the dynamical theory is treated. In particular, specific attention is given to the implementation of the convergence of the incident beam and the program parameters. Since the main objective in the presentation of the results has been the ability to make a good comparison between the experimental and calculated results, the method in which the results are presented is discussed in detail. Finally, the use of the CDC Cyber 205 computer of the Stichting Academisch Rekencentrum Amsterdam (SARA) is treated, based on considerations of computation time.

The results of the calculations are presented in chapter 5. A comparison is made between calculated and experimental images where possible. All the experimental results have been obtained using a Philips EM400T electron microscope. The calculated images are presented in such a way to allow a direct comparison with the diffraction images obtained in electron microscopy. In addition, line-scans of certain CBED patterns have been determined from the point of view of the computation time needed for the calculation of images. These line-scan calculations reduce the calculation time considerably, whilst retaining virtually the same amount of information on the symmetry relations within the CBED pattern.
The following subjects are treated.
1) Images are presented which have been obtained during the testing phase of the computer program, using known observations in CBED patterns of silicon single crystal specimens. It is shown that, in order to obtain good agreement between the calculated and experimental results, only those reflections which lie on the

Ewald sphere within the angle of convergence need to be included in the calculations.

2) The effect of thickness variations is illustrated using the example of gold single crystal specimens. In order to obtain a good agreement in the case of gold between the calculated and experimental image, the specimen thickness needs be known to within an accuracy of at least 10% .

3) The effect of absorption is treated using the examples of single crystal specimens of gold and gallium-arsenide and a bicrystal of gold. Because of its complexity, it is difficult to generalize the relation between the intensity profile of the CBED pattern and the effect of absorption. It is illustrated that in the case of gold, those symmetry relations which are observed in the CBED pattern by virtue of the reciprocity relation are destroyed by the effect of absorption. In the case of gallium-arsenide this behaviour is not apparent.

4) The effect of position of a <1 1 1> twin boundary in bicrystal specimens of silicon and gold on the symmetry of the CBED pattern is discussed. It is shown, based on a resolution of 16 greylevels, that a deviation of the interface greater than 4% from the symmetrical (mid-plane) position destroys the symmetry, which is specific for the bicrystal construction.

5) The change in symmetry in CBED patterns is calculated for bicrystal specimens of silicon having an additional translation of 1/6[0 1 $\bar{1}$] and 1/12[$\bar{1}$ 2 $\bar{1}$] at the twin boundary respectively. The symmetry observed in the calculated images is in agreement with that expected for these translations. The resulting images, still however, show a remarkable similarity with the image belonging to the state of zero translation. The translation at the boundary can, therefore, only be established when the symmetry of the pattern is clearly observed.

6) A more complex type of boundary is discussed using the example of a bicrystal of gold, having a <1 1 1> Σ=7 type twist boundary. In the experimental image at 100 kV, a FOLZ reflection is observed, which shows an abnormal intensity distribution and cannot be indexed according to the superposition of the individual single crystal reflections. It is calculated that this particular reflection is the (25 7 $\bar{17}$) CSL reflection.

7) Finally, a calculation based on a single crystal specimen of gold illustrates the application of the Tanaka method.

Samenvatting.

Een korte inleiding tot het onderwerp beschreven in dit proefschrift wordt gegeven in hoodfstuk 1. Hierna worden de beginselen van Convergerende Bundel Elektronen Diffraktie (CBED) besproken in hoodfstuk 2. Een algemene beschouwing wordt gegeven betreffende de symmetrie en de interpretatie van CBED patronen. De classificatie van de mogelijke symmetrie relaties in CBED patronen volgens Buxton et al. [1976] wordt geïntroduceerd.

Hoodfstuk 3 is toegespitst op de beschouwing van de symmetrie in CBED patronen, afkomstig van bikristallen. Voor de beschrijving van bikristalsymmetrie wordt het concept van gekleurde symmetrie operatie geïntroduceerd, met daaraan verbonden een algemene mathematische beschrijving van de ruimtegroep synthese voor bikristallen. De classificatie volgens Schapink et al. [1983] en Buxton et al. [1983] wordt besproken.

Hoofdstuk 4 is gesplitst in twee delen.
In het eerste deel wordt uitgebreid ingegaan op de dynamische theorie, zoals ontwikkeld door Bethe [1928], inclusief het effect van hogere orde Laue zone reflecties. De beschrijving van absorptie vindt plaats met behulp van eerste orde storingsrekening. Een korte vergelijking tussen the Bloch-golf methode en de 'multi-slice' methode wordt gegeven.
Het tweede gedeelte is gereserveerd voor de behandeling van de implementatie op basis van de dynamische theorie. Specifiek wordt ingegaan op de beschrijving van de convergentie van de inkomende bundel en de parameters voor het beschrijven van het kristal preparaat. Ook wordt nader ingegaan op de manier van presentatie van de resultaten, omdat tot één van de voornaamste doelen heeft behoord, de mogelijkheid van een vergelijking van berekende en experimentele resultaten. Het gebruik van de CDC Cyber 205 van de Stchting Academisch Rekencentrum Amsterdam (SARA) wordt gemotiveerd aan de hand van overwegingen met betrekking tot de rekentijd.

In hoofdstuk 5 worden de resultaten van de berekenigen gepresenteerd en besproken. Waar mogelijk wordt een vergelijking gemaakt met experimentele resultaten, verkregen met behulp van een Philips EM400T elektronen microscoop. De meeste berekende resultaten zijn zodanig gepresenteerd, dat een direkte vergelijking met de experimentele resultaten mogelijk is. Ook zijn een aantal 'line-scan' berekeningen uitgevoerd, welke illustreren dat, met slechts een aantal berekende intensiteiten, en daarmee een sterk gereduceerde rekentijd, informatie kan worden verkregen over de symmetrie in een CBED patroon.
De volgende onderwerpen worden behandeld.
1) Aan de hand van berekeningen aan silicium éénkristallen wordt de testfase van het computerprogramma besproken. Zo wordt aangetoond dat, voor een goede overeenkomst tussen de berekende en experimentele beelden, slechts die reflecties voor de berekeningen hoeven te worden beschouwd welke op de Ewald bol liggen binnen de convergentie van de inkomende bundel.

2) Het effect van preparaatdikte op het resulterende intensiteitsprofiel van de beelden wordt geïllustreerd aan de hand van berekeningen aan goud éénkristallen. Voor een goede overeenkomst tussen berekende en experimentele beelden is bekendheid van de dikte binnen 10% nauwkeurigheid noodzakelijk.

3) Het meenemen van absorptie effecten bij de berekenigen wordt geïllustreerd met behulp van berekenigen aan modellen van goud en gallium-arsenide éénkristallen en goud bikristallen. Gezien de complexiteit van het effect dat absorptie heeft op de patronen is het niet mogelijk om dit effect te generaliseren. Wel wordt aangetoond dat absorptie invloed heeft op de symmetrie relaties in het CBED patroon van goud één- en bikristallen, welke kunnen worden geobserveerd als gevolg van het omkeerbaarheids principe. In het geval van gallium-arsenide wordt dit effect wel met berekeningen aangetoond, maar blijkt het te klein om geobserveerd te worden.

4) In geval van een silicium bikristal wordt de invloed van de positie op de symmetrie van het CBED patroon van een <1 1 1> tweeling grensvlak in het preparaat bekeken. Er wordt aangetoond, aan de hand van berekende beelden gebaseerd op 16 grijswaarden, dat een afwijking van het middenvlak van het preparaat van slechts 4% voldoende is om de symmetrie, specifiek voor het bikristal, te verstoren.

5) De symmetrie van CBED patronen behorende bij een silicium bikristal met een translatie van, respectievelijk, 1/6[0 1 $\bar{1}$] en 1/12[$\bar{1}$ 2 $\bar{1}$] aan de tweelinggrens wordt berekend. De symmetrie is overeenkomstig de verwachtingen. Aan de andere kant wordt aangetoond dat de patronen veel lijken op het beeld behorende bij het geval zonder translatie. Voor de bepaling van de translatie aan het grensvlak is een duidelijke aanwezigheid van de symmetrie daarom noodzakelijk.

6) Een meer complex geval betreft een silicium bikristal met een <1 1 1> torsie grensvlak van het type Σ=7. Het experimentele beeld bij 100 kV vertoont een reflectie, welke een abnormale intensiteits distributei vertoont en niet te indiceren is op basis van de superpositie van de FOLZ reflecties van de individuele éénkristallen. Aan de hand van berekenigen wordt aangetoond dat de reflectie in kwestie de (25 7 $\bar{17}$) CSL reflectie is.

7) Als laatste wordt aan de hand van een berekend beeld gebaseerd op een goud éénkristal de Tanaka methode geïllustreerd.

Curriculum Vitae.

Nico Selhorst Blom werd op 28 maart 1956 te 's-Gravenhage geboren. Na een vooropleiding Atheneum B aan de s.g. Hugo de Groot te 's-Gravenhage, startte hij in 1975 met een studie scheikunde aan de Rijksuniversiteit te Utrecht. Het kandidaatsdiploma werd in mei 1979 behaald. Onder begeleiding van dr. J.A. Kanters vervolgde hij zijn doktoraalstudie aan de Rijksuniversiteit te Utrecht met een hoofdvak struktuurchemie (prof.dr. J.C. Schoone; vakgroep Algemene Chemie) en een bijvak informatica (prof.dr. J. van Leeuwen; vakgroep Informatica). Het doktoraaldiploma werd in juni 1982 behaald. Gedurende die periode was hij tevens werkzaam als student-assistent.
Vanaf augustus 1982 tot augustus 1986 was hij werkzaam bij de Stichting voor Zuiver Wetenschappelijk Onderzoek (ZWO), in opdracht van de Stichting Scheikundig Onderzoek Nederland (SON), en als wetenschappelijk assistent verbonden aan het Laboratorium voor Metaalkunde van de TH Delft. Aldaar heeft hij het onderzoek verricht dat in dit proefschrift is beschreven.